DISSERTATION

# NUMERICAL AND EXPERIMENTAL EVALUATION OF THE ERODIBILITY OF PARTICLE PACKINGS WITH SURFACE TREATMENTS AND SPRING REINFORCEMENTS USING THE DISCRETE ELEMENT METHOD

Submitted by

Kirsten LaRhea Peterson

Department of Civil and Environmental Engineering

In partial fulfillment of the requirements

For the Degree of Doctor of Philosophy

Colorado State University

Fort Collins, Colorado

Spring 2019

Doctoral Committee:

Advisor: Paul Heyliger
Co-Advisor: Christopher Bareither

Rebecca Atadero
Stephanie Kampf

ABSTRACT

NUMERICAL AND EXPERIMENTAL EVALUATION OF THE ERODIBILITY OF PARTICLE PACKINGS WITH SURFACE TREATMENTS AND SPRING REINFORCEMENTS USING THE DISCRETE ELEMENT METHOD

Chapter 4: The erodibility of homogeneous two-dimensional spherical particle packings subjected to added mass surface treatments was explored using a combination of physical flume experiments and the discrete element method (DEM). Packings composed of spherical glass particles, with and without surface treatments and angled at two different slopes, were tested experimentally and simulated numerically under surficial flow conditions. The surface treatments acted to add mass to the surface of the particle packings. Particle erosion was quantified by tracking eroded particles as a function of fluid velocity. DEM simulations and flume experiments were first performed with a layer of steel particles that served as an extreme case of surface treatment. Similar trends were observed between the simulations and experiments, whereby the number of eroded particles decreased by an average of 90% when compared to untreated cases. The results from this surface treatment suggested that if the surface treatment mass is large enough, nearly all particle erosion under surficial flow conditions can be mitigated. Additional experiments were performed with surface treatments composed of increasing application rates of wetted agricultural straw. The particle erosion rates were dominated by piecewise linear behavior as a function of eroded mass versus fluid velocity. This behavior indicated a) an initial resistance to flow based on gravity, followed by b) a surface treatment movement that induced widespread failure or erosion at a much higher rate. Dislodgement and subsequent erosion of particles occurred at higher fluid velocities

(over 50% higher for the highest straw application rate) when the surface treated cases were compared to the untreated cases. Conclusions drawn from the simulation and experiment results indicated a direct correlation between added mass on the surface of a particle packing and decreased erosion under surficial flow conditions and showed that as slope increased, erosion levels increased and began at lower surficial flow fluid velocities.

Chapter 5: The erodibility of three-dimensional particle packings reinforced numerically with elastic springs and subjected to overland flow conditions was explored using the discrete element method (DEM). Particle packings at three slopes, subjected to overland flow at two fluid velocities, and four reinforcement configurations resulted in a total of 24 datasets of simulation results for comparisons to be made. The three slopes were composed of the same 2400 particles with coarse sand material properties and a uniform distribution of diameters between 1.8 and 8.0 millimeters. The elastic spring reinforcements represent a potential modeling technique for root development in a soil. The spring reinforcement technique presented here is a proof-of-concept attempt to model three-dimensional slopes at up-scaled particle sizes, root stiffness, and fluid velocities. Particle displacements were tracked and compared as functions of time, reinforcement level, and slope. The results suggest linear relationships between decreased particle movement with increased percent reinforced surface particles, increased particle movement with increased slope, and decreased sediment yields with increased percent reinforced surface particles. Also, at the lower fluid velocity, particle displacements were more dependent on incremental changes in slope; whereas at the higher fluid velocity, particle displacements were not dependent on small changes in slope. Overall, the results from the simulations and experiments showed the influence of elastic spring reinforcements on particle movements and the next step of the research would be to assess the scaling effects and apply the root model to smaller particles, more indicative of where

roots are expected to grow.

# ACKNOWLEDGEMENTS

I would like to first and foremost thank my advisor Dr. Paul Heyliger for his constant support and encouragement throughout my entire time spent at Colorado State University. I truly could not have completed this research, along with the research completed for my master's thesis, without his insight, advice, and guidance along the way. Thank you and I look forward to the possibility of collaborating on new projects together in the future.

I would also like to thank my other committee members for their perspectives on all angles of the project. I've been known to get caught up in the small details instead of focusing on the bigger picture. Their insights have helped me tremendously with taking a step back and spending time on the bigger takeaways of the research instead of only thinking about the minute details in the code calculations. Also, a special thank you goes to Dr. Christopher Bareither for working to acquire the funding that supported me financially while completing this research and his valuable input on editing my writing.

Finally, I need to thank my family, friends, and especially my husband, Tyler, for their endless love, help, patience, and motivation. Having all of your support gives me the confidence to go for anything and everything I want to do in life.

TABLE OF CONTENTS

LIST OF TABLES

LIST OF FIGURES

# Chapter 1 : INTRODUCTION AND BACKGROUND

Slope erodibility simulations and experiments at the particle level are the bulk of this research. The behavior of several different slopes under hydraulic loading were investigated with different types and amounts of reinforcements and ground-treatments in place. The discrete element method (DEM) is a numerical tool used to solve problems over a range of technical fields and the simulations presented in this dissertation were performed with a program written specifically for this research, based around the DEM. Also, experiments were performed and compared with the DEM results.

This dissertation follows the format of presenting journal articles as chapters, but because of the nature of this content, chapters are also included with more details on the DEM model. The remainder of this chapter focuses on an introduction to current ground treatments applied to burned soil slopes, the original motivation for this work, and on an introduction to methods used to model particulate behavior, and finally more details on the DEM will be discussed. Chapter 2 presents the theoretical basis of DEM modeling and details on the approach taken for this DEM model. Chapter 3 provides details on benchmark tests that were used to verify the force calculations in the model at the particle impact level. Chapter 4 presents a manuscript titled “Numerical and Experimental Evaluation of the Erodibility of Surface Treated Particle Packings”, to be submitted to Journal of Engineering Mechanics, ASCE. Chapter 5 presents a manuscript titled “Numerical Evaluation of the Erodibility of Particle Packings with Spring Reinforcements using the Discrete Element Method”, submitted to Granular Matter, Springer. In Chapter 6, conclusions are discussed for this research. Also, implications of the completed work are suggested and ideas for future research are discussed.

## Post-fire Ground Treatments

Every year wildfires pose a threat to land in Colorado and the Western United States. Climate variability has caused the amount of destructive wildfires to increase over the past decade and is expected to continue to increase (Robichaud et al., 2010). Following a fire, the soil can be left bare and un-reinforced. Precipitation events after a fire can lead to increased runoff, flooding, erosion, and debris flows (Stewart et al., 2003). Post-fire recovery in the Colorado Front Range is longer than most other locations, because of highly erodible granitic soils, sparse vegetative cover, and steep topography. In addition, large sediment yields can be produced for several years after a fire by intense summer convection storms (Robichaud et al., 2010).

One prime example of this behavior that occurred in Colorado were the storms that caused massive flooding in September of 2013, just one year after the High Park wildfire in the mountains west of Fort Collins. Figure **1-1** (Rocky Mountain Research Station Collaborators, 2017) shows a before and after flood comparison at an area downstream from the High Park fire area. As can be seen from the two photographs, "the 2013 floods flushed large quantities of sediments downstream, widening the channel" (Rocky Mountain Research Station Collaborators, 2017).


Figure 1-1: "Postfire, the valleys in the High Park fire area accumulated sediment" (Rocky Mountain Research Station Collaborators, 2017).

Figure 1-2 (Shahverdian, 2015) shows a before and after comparison at a location directly in the High Park Fire burn area. This comparison shows sediment transport after a typical summer storm, and by comparing the two photographs, the differences in sediment in the channel before the storm (virtually no sediment in the left photograph) and after the storm (a noticeable depth of eroded soil material) can be seen. The circles indicate the same location.


Figure 1-2: Sediment transport after a summer storm at a High Park Fire burn location (Shahverdian, 2015).

Robichaud et al. (2010) and Napper (2006) report that current post-fire soil stabilization techniques include erosion barriers, mulching, or a combination of these options. The overall goals of current ground treatments are to promote water infiltration into the burned soil and to delay and/or prevent overland flow that will erode soil particles. Mulch treatments are applied to burned soils to modulate soil moisture and temperature and improve soil structure and nutrient content. Mulch materials include agricultural straw, wood shreds, paper, cotton, and flax. Figure 1-3 shows

a burn location with a boundary between an area that was mulched and an area that was not mulched. The effectiveness of using mulch can be seen by comparing the levels of regrowth in the background (much taller vegetative growth) with the foreground (hardly any vegetative growth).

Figure 1-3: After three growing seasons, the ground cover of the mulched and seeded area (background of the photograph) is much greater than the seeded only area (foreground) (Robichaud et al., 2010).

How mulch works to reduce erosion has been hypothesized, but not shown at a particle level. The published assumptions are that mulch ground cover reduces raindrop impact, promotes infiltration, and aids in seed retention on the slope to stimulate vegetative growth. A hypothesis discussed later in this dissertation proposes that another reason mulch ground treatments have been successful at decreasing erosion is because of the compressive stress from the added mass on the surface. The gravitational forces from the added mass on the soil surface may act similar to a pressure, holding surface particles in place. This added mass could especially have an impact during a rain event, considering not only the added mass from the mulch itself, but also from the

water that soaks in as the mulch is saturated. Also, the mulch provides a physical barrier that adds frictional forces that act to reduce surface particle rolling and sliding.

The majority of research on slope stabilization techniques has been conducted with field observations, field tests, and laboratory testing. A summary of mulch treatment effectiveness studies given by Robichaud et al. (2010), discusses studies that were carried out on land areas ranging from 20-30 $m^2$ to 1000-5000 $m^2$. The studies were carried out over at least 2-3 years to gather substantial data. Although these studies can yield invaluable data at field scale, the studies require large amounts of equipment and materials, are limited by burn locations, burn area sizes, and rain event unpredictability, and take years to gather data.

Seeding a burned area of land also can be used to help promote and quicken root growth and development. The natural recovery of native vegetation reduces erosion over time and soils with more vegetation and organic matter have been shown to have higher infiltration rates, more reinforced and strengthened soil structure, and are less erodible because the soil stability is increased (Robichaud et al., 2010). Seeding typically is completed in conjunction with post-fire ground treatment (e.g., straw mulch) to help retain seeds on the slopes to promote germination. Simulations were also performed for this research to model the relationship between reduced erosion with increased root development and one application of this would be as vegetation is established on a post-burned soil slope.

**Modeling Particulate Behavior**

The following are two primary methods used to model particulate behavior: continuum (or Eularian) based approaches and discrete (or Lagrangian) based approaches (Bossy & Safuryn,

2016). Continuum approaches assume that the material is continuous and all space is filled with matter while ignoring individual particle behavior. Discrete modeling represents granular matter as an idealized assembly of particles with overall macroscopic behavior resulting from the collection of all particle interactions. The choice between continuum and discrete modeling depends on the particular system being simulated, but discrete modeling is preferred when modeling granular, discontinuous flow (Bossy & Safuryn, 2016). An example comparing the geometries of a continuum model and a discrete model is shown in Figure 1-4.

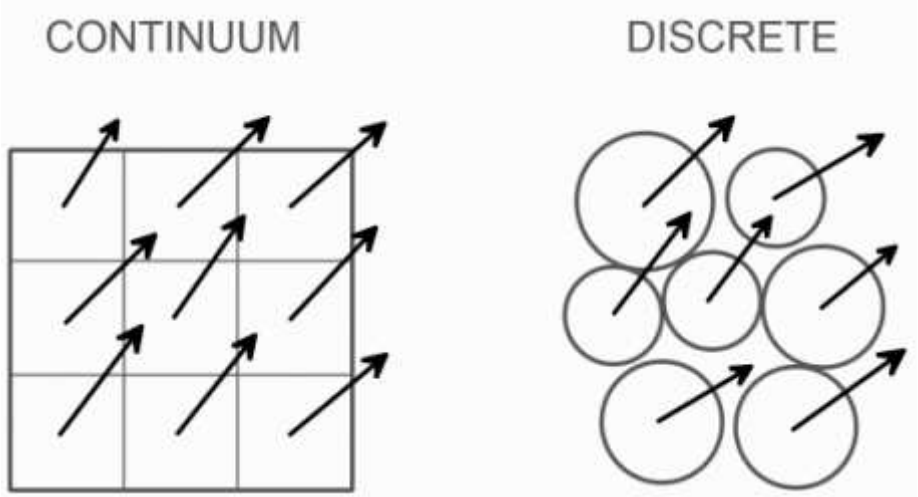


Figure 1-4: Example system geometry modeled with both a continuum approach and a discrete approach. Arrows show example resultant forces on a continuous material with specified areas in a grid (continuum) and on individual particles (discrete) (Bossy & Safuryn, 2016).

There are several advantages and disadvantages for both continuum and discrete modeling. The main advantage of continuum modeling is that as larger volumes are modeled, and therefore comparable DEM models will have more and more particles, continuum modelling quickly becomes much more computationally efficient than the DEM counterpart (Coetzee, 2014). Disadvantages include difficulty in deciding on a constitutive law that will accurately represent the mechanics of the system since the constitutive laws for continuum modeling can be very complex and contain many provisional parameters and equations (Cundall, 2001). Also, because

the matter is modeled as a continuum rather than as individual particles that are free to move, capturing localized behavior in a continuum model that uses a mesh can be difficult. The development of shear bands is an example of this behavior (Cundall, 2001).

Some advantages to discrete modeling are that the equations between particles are not coupled, the math is fairly straight forward, and discrete modelling can be used to study micromechanics of materials at the particle level. One disadvantage to discrete modeling is that analyses can quickly become computationally very expensive with the increase in total number of particles in the simulation. To accurately represent macroscopic behavior of a granular material, a large enough volume of the material must be modeled and, for example, a relatively small volume of soil will contain a relatively large amount of particles. Therefore, a balance must be found in discrete modeling where enough particles are modeled to accurately represent the macroscopic behavior while modeling a small enough number of particles to keep analyses to realistic computational times. The most persuasive explanations for using discrete element methods are that macroscopic behavior of a particulate system often depends on particle level behavior and this method accurately models the individual interactions between particles.

**The Discrete Element Method**

The discrete element method can be defined as "a numerical method that simulates the response of granular materials considering the individual particles to be rigid and uses relatively simple models to simulate their interactions" (O'Sullivan, 2011). Yet another advantage of DEM modeling is that particle-scale information can be tracked and recorded throughout the simulations, such as individual particle orientations and rotations, while this can be a relatively difficult task (if not impossible) to measure/track during laboratory tests. Specifically, for laboratory testing in the

geomechanics field, collecting undisturbed soil samples from the field can be difficult and no two samples will be the same. On the contrary, the same input file (initial configuration of particles) can be used for an unlimited number of DEM simulations. Laboratory testing of course has the advantage that physical material response is captured, while DEM simulation results are subject to validation and calibration of the model.

The most cited reference, by far, on the discrete element method is Cundall and Strack (1979). They laid the groundwork for using the discrete element method to describe the mechanical behavior of assemblies of discs and spheres and their work was the first granular dynamics simulation technique published in the open literature (Zhu et al., 2007). Since then, there have been several published articles on the DEM, advancing the pool of knowledge on the subject. Zhu et al. (2007) provide a very thorough compilation of literature on the major theoretical developments in DEM modeling. The authors present a figure on how the number of publications on the DEM has increased over the years. Their data was only available up until 2006. Therefore, the search method used was expanded on here to create Figure with more recent data. The figure presents the number of publications related to the DEM from 1987 to 2017, obtained from the Web of Science with the following keywords: discrete element method/model, distinct element method/model, discrete particle simulation/method/model, and granular dynamic simulation. As can be seen from Figure 1-5, using the DEM to simulate granular systems has become increasingly more popular over the last thirty years.

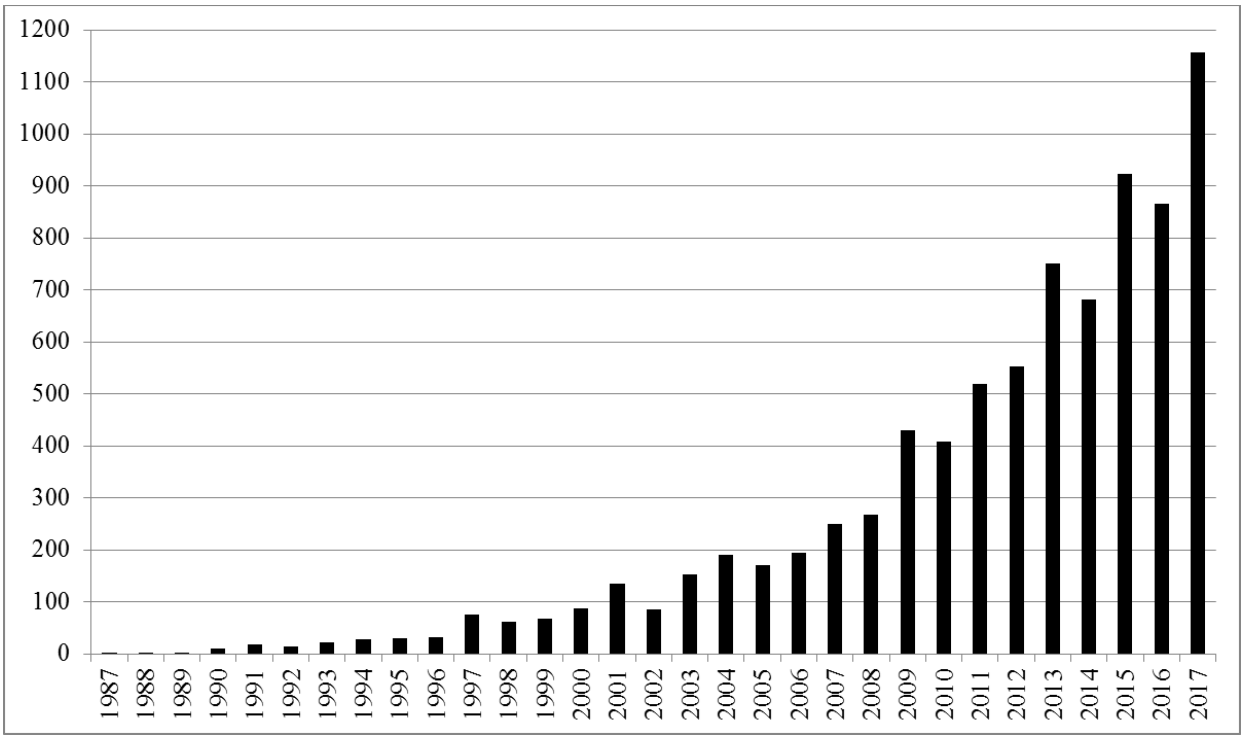

Figure 1-5: Number of publications related to the DEM from 1987 to 2017.

Zhu et al. (2007) group their information into the following three major categories: calculation of particle-particle and particle-fluid interaction forces, coupling DEM with CFD to describe particle-fluid flow, and linking DEM modeling to continuum modeling. Firstly, the governing equations for the translational and rotational motion of a particle are presented (Zhu et al., 2007). Several DEM modelling techniques and equations have been proposed to calculate the forces and torques required for the governing equations and those used for the research performed for this dissertation are cited accordingly in 0.

Much of the development of the DEM model used for the research presented here in this dissertation relies heavily on the book by O'Sullivan (2011). The equations and force models referenced from O'Sullivan are presented and explained later in this dissertation.

When developing numerical models in research, comparing results with a physical experiment is advantageous. The experiment can be used to validate and calibrate the numerical model. This method is being used in the research performed for this dissertation.

Chandramohan and Powell (2005) ran experiments on collisions between two spheres and monitored particle paths and rotations with digital photographic equipment. They were able to measure coefficients of tangential and normal restitution and friction angles. However, they found that when the measured parameters were used in a DEM analysis using the commercial code PFC, the viscous damping model, originally developed by Cundall and Strack, failed to correctly predict paths of particles colliding in the sliding impact (slip) region. Because Cundall and Strack originally developed the viscous damping model for the study of soil mechanics and slow creeping motion of particles, the simplifications made might not be appropriate for rapid granular flow. Future work for the authors consists of refining DEM contact models to more realistically model particle behavior under rapid collisions. Experimental results were able to guide the direction of the DEM simulations, which then led to a method of better numerically modelling complex physical behavior.

Another example of using experiments to validate a DEM model was presented by Cui et al. (2007). Triaxial tests were performed on specimens of steel spheres. The novel technique used here by the researchers is that they used circumferential periodic boundaries in their DEM model to accurately simulate the particle behavior, while greatly decreasing the run time of the simulations. A periodic boundary condition is a technique used to decrease the number of particles needed for the simulation and to eliminate non-realistic boundary effects that occur from using rigid boundaries. More details on this type of boundary condition are discussed in a later chapter.

Lu et al. (2014) present a descriptive figure showing the process of calibrating the particle level properties in a DEM model to obtain accurate macro-level behavior and this figure is shown here in Figure 1-6. This is done by varying the input particle-particle level parameters of the DEM and running numerical triaxial compression test and Brazilian tensile test simulations until the macro-level behavior parameters of the simulations match the properties obtained during physical experiments of the actual material. Although not performed on these same tests, a similar procedure of varying input particle-particle level parameters in the model and comparing simulations with physical experiments was performed for the research presented in this dissertation to calibrate the model.

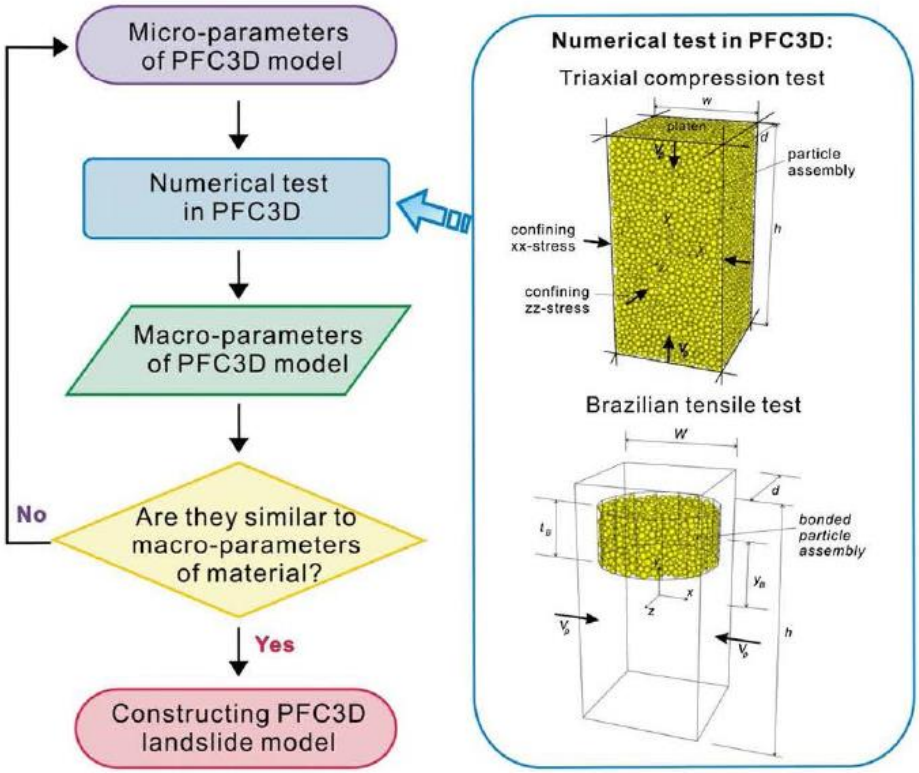


Figure 1-6: A flow chart showing the derivation of the micro-parameters used to construct a PFC3D model (Lu et al., 2014).

Although the DEM has been used to model field scale boundary value problems of soil and rock slopes (discussed later in this chapter), articles published on DEM analyses of laboratory

experiments greatly outnumber articles published on field scale DEM analyses (O'Sullivan, 2011). Also, in the geomechanics field when authors compare to experimental results, comparing with laboratory experiments, rather than field scale experiments, is much more common. Key references for numerous laboratory experiments modelled with the DEM have been summarized by O'Sullivan (2011) and are shown with more detail in Table 1-1 (triaxial tests by Cui et al. were previously discussed in this section).

Table 1-1: Key References for Laboratory Experiments Modelled with the DEM

| Laboratory Experiment | Article | Reference |
|---|---|---|
| Biaxial compression test (2D, unbonded) | Rolling Resistance at Contacts in Simulation of Shear Band Development | (Iwashita & Oda, 1998) |
| Biaxial compression test (2D, bonded) | A bonded-particle model for rock | (Potyondy & Cundall, 2004) |
| Triaxial test (with periodic boundaries) | Numerical simulations of deviatoric shear deformation of granular media | (Thornton, 2000) |
| Triaxial test | An analysis of the triaxial apparatus using a mixed boundary three-dimensional discrete element model | (Cui et al., 2007) |
| Plane strain test (with periodic boundaries) | Shear strength of assemblies of ellipsoidal particles | (Ng, 2004) |
| Plane strain test | Numerical modelling of plane strain tests on sands using a particulate approach | (Powrie et al., 2005) |
| True triaxial test (with periodic boundaries) | Shear strength of assemblies of ellipsoidal particles | (Ng, 2004) |
| | Numerical simulations of deviatoric shear deformation of granular media | (Thornton, 2000) |
| Direct shear test (2D) | Micromechanical analysis of the shear behavior of a granular material | (Masson & Martinez, 2001) |
| Direct shear test (3D) | Exploring the macro- and micro-scale response of an idealised granular material in the direct shear apparatus | (Cui & O'Sullivan, 2006) |
| Simple shear test | Grain rotation versus continuum rotation during shear deformation of granular assembly | (Matsushima et al., 2003) |
| Interface shear test | Numerical studies of shear banding in interface shear tests using a new strain calculation method | (Wang et al., 2007) |
| Penetration test (2D) | An analytical study of cone penetration tests in granular material | (Huang & Ma, 1994) |
| Penetration test (3D) | Homogeneity and symmetry in DEM models of cone penetration | (Butlanska et al., 2009) |

A large part of the analyses performed for the research presented in this dissertation deal with analyzing slope surficial particle interactions that lead to erosion; what forces cause particle flows leading to erosion and what types/amounts of reinforcements or surface treatments can help avoid or delay erosion. Therefore, a review of other slope stability analyses is included in this chapter.

Stead et al. (2006) present a very thorough investigation of numerical modelling techniques used to simulate rock slope failures. They present mostly on DEM analyses, using PFC, and hybrid finite/discrete element codes. Critical input parameters, advantages, and limitations of each are discussed and the importance of the behavior of deforming rock slopes due to a combination of yield and fracturing is emphasized.

Zhang et al. (2005) present results showing how DEM was used to accurately simulate movement of a landslide at the Panluo iron mine in China that started moving in 1990. Since then, monitoring equipment has been placed and shows that the slippage of the landslide is closely related to rainfall. The DEM simulations take into account water reducing the shear strength of the weak interlayer on the sliding surface and water seeping through the fractures at the back of the landslide causing artesian pressure that reduces the effective stress on the sliding surface. The simulations performed by Zhang et al. (2005) are closest in the literature to the analyses performed for the research presented in this dissertation. However, while they simulate a cross-section of the entire slope (over 500 meters in length) with only 1650 elements, soil particle aggregates are modeled, closer to an individual soil grain scale, in the simulations performed for this dissertation. Also, drag forces from water running down the slope are included.

Taboada and Estrada (2009) model a rain-triggered rock and soil avalanche using a 2D contact dynamics DEM. Unlike most DEM analyses that allow for overlap between particles,

which then form contact forces as a function of that overlap, a contact dynamics model considers particles to be perfectly rigid. Instead of contact forces developing because of overlap, they are calculated to enforce kinematic constraints. Although there are differences in the formulation of the equations of motion, results from these simulations are similarly interpreted to analyses like the ones presented in this paper, by looking at the dependence of overall macroscopic behavior on elemental interactions. Similar to analyses presented in this dissertation, the authors simulate a rain-triggered failure mode. However, while they induce failure purely from an increase in the water table, the analyses performed for this dissertation consider drag forces on the soil surface from overland flow.

Using PFC3D, Lu et al. (2014) study catastrophic slope failures based off input slip geometries. Depending on the given predicted slip geometry, the DEM is used to predict runout paths and particle velocities. The authors present a useful discussion on systematically varying micro-parameters for the DEM simulations, such as particle-particle friction coefficients, contact moduli, and bond stiffnesses, until the macro-scale material property results from the simulations match material properties from laboratory tests on soil samples. Overall, they show that PFC3D can be useful in modeling landslides, but that limitations exist in modeling all complex mechanisms, as is the case with all DEM simulations.

Most DEM simulations focused on geomechanics have been completed using commercial or open source codes. The first commercial code developed for three-dimensional DEM simulations is Trubal (Cundall & Strack, 1979) and the most common three-dimensional commercial codes currently used, which are altered adaptions of and closely linked to Trubal (O'Sullivan, 2011), include PFC3D and EDEM. Common open source DEM codes include LIGGGHTS, ESyS-Particle, YADE, and OVAL.

The research performed here differs from most published DEM analyses in that commercial or open source code was not used and an original discrete element model was written in Fortran coding language and analyses were performed using capabilities of a high-performance computing system. Details on the model will be discussed in a later chapter.

As with most numerical models, a discrete element model is an idealization of the actual physical system and therefore several assumptions are made to complete the analyses. Computational cost is a big concern for DEM analyses, and so there exists a trade-off between computational cost and physical practicality. Perhaps the largest assumption made in the DEM analyses of the research presented here is that the particles simulated are perfectly spherical. Particle irregularities are going to exist in a physical soil; however, spheres are the simplest to use computationally because calculating if they are in contact with other spheres or with boundaries is easy and spheres have the simplest (yet still accurate) contact models. Because of the contact model chosen, another assumption made for these analyses is that the particles deform elastically. This is not a bad assumption for sand particles but could cause problems for soils with more complicated constitutive laws. There are several other assumptions made for the completion of this research, but they are explicitly described herein and supported with explanations, published experimental evidence, and citations.

As has been demonstrated, DEM simulations can produce qualitatively realistic results (Thornton & Antony, 2000). Also, with DEM simulations, several analyses (for example with different loadings) can be performed on the same exact initial configuration. This is not possible in laboratory experiments, where there are unavoidable differences in each test specimen. For a natural system, these differences may be necessary to account for ranges of variables in the system the researcher is investigating. However, when testing something external to the natural system,

differences in specimen initial configurations could possibly lead to uncertainties when comparing the test results. In DEM simulations (or any numerical simulations for that matter), these uncertainties do not occur (Thornton & Antony, 2000).

# Chapter 2 : THE DISCRETE ELEMENT METHOD

A numerical model using the discrete element method (DEM) was developed to better understand reinforced or protected soil behavior at a particle level. The DEM model was used to represent the geometry and hydraulic loading of physical experiments. Verification of the accuracy of the DEM model will have potential future applications to allow for rapid assessment of the controlling input parameters. These include but are not limited to the material properties of the particles, particle size distribution, and surface slope, the ground treatment type and associated properties, hydraulic loading mechanisms, and other types of applied external loads without having to construct a physical model.

The overall modeling procedure incorporated within the DEM code is shown in Figure 2-1. The system geometry and boundary conditions are described first, as is the total range of time over which the analysis will be completed. The total time duration is divided into a finite number of time steps. For each time step, the contacting particles are identified using a contact detection algorithm and the contact forces are calculated between interacting particles. The resultant force acting on each particle is calculated, including body forces, non-contact particle forces, and all external forces that include but are not limited to those from gravity, rain, and changing boundary conditions. Using the resultant forces that act on each particle, the particle accelerations are calculated and then integrated in time to determine particle velocities. Finally, for each time step, the particle displacements are calculated and the current particle positions are updated. These steps are then repeated for the next time step where forces will most likely change based on particle location. These steps are repeated until the final time duration has been reached. The circular arrow path of Figure 2-1 represents the time stepping.

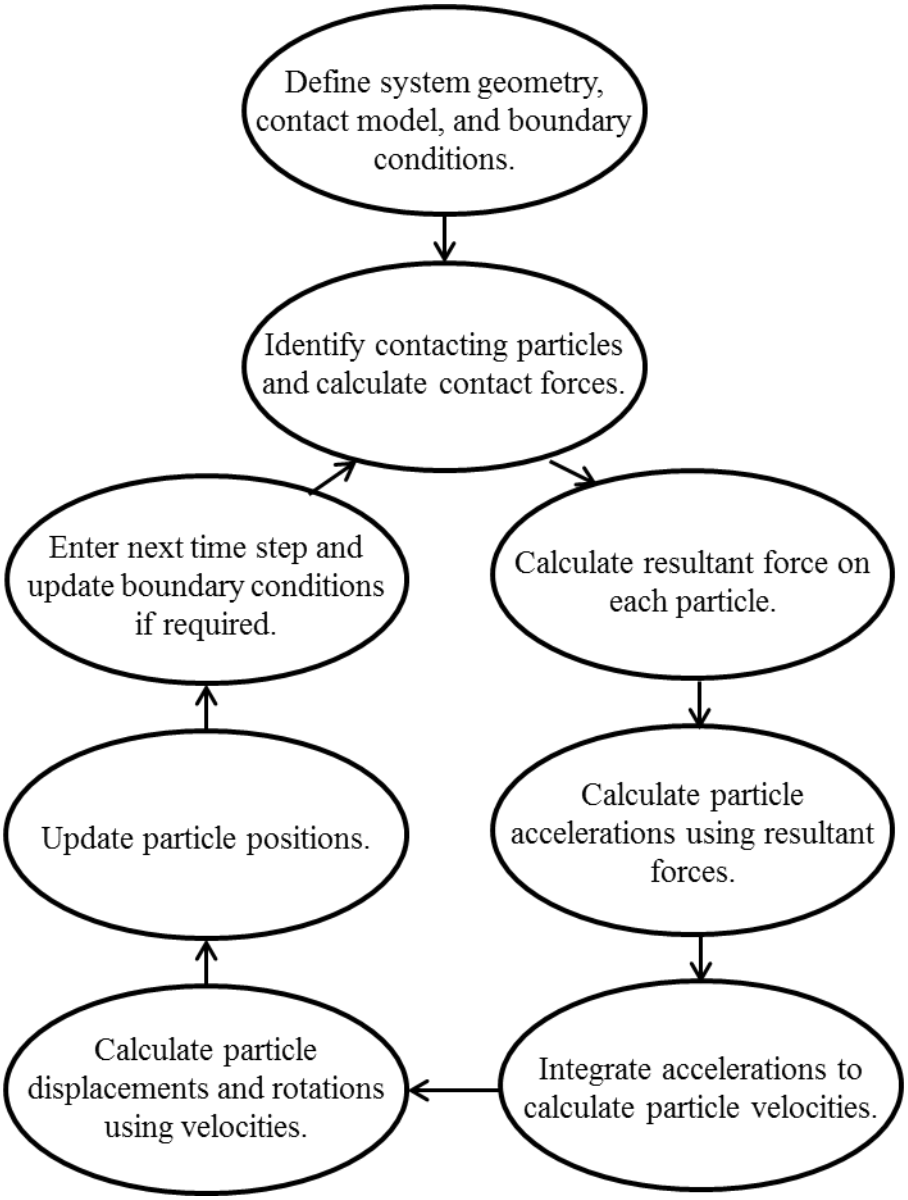


Figure 2-1: Illustrative representation of the calculation steps performed in a DEM simulation.

Using the DEM model, simulations were performed on three-dimensional sphere models. Throughout the rest of this chapter, equations and algorithms that make up the model are discussed along with discussions on why the specific equations, appropriately referenced, were chosen and the associated benefits and/or limitations.

**Particle Kinematics**

The discrete element model was formulated using Newton's vector equations of motion to govern the particle behavior. Each particle has six degrees of freedom; three translational and three rotational. The expression of the equations of motion governing the translational and rotational dynamic equilibrium of each individual particle *i* with mass mi and moment of inertia Ii (Zhu et al., 2007) are expressed as

$$\boldsymbol{m_i \frac{dv_i}{dt}} = \sum_j \boldsymbol{F_{ij}^c} + \sum_k \boldsymbol{F_{ik}^{nc}} + \boldsymbol{F_i^f} + \boldsymbol{F_i^g} \qquad \text{[Equation 2-1]}$$

$$\boldsymbol{I_i \frac{d\omega_i}{dt}} = \sum_j \boldsymbol{M_{ij}^c} \qquad \text{[Equation 2-2]}$$

where $v_i$ is the translational velocity, $\omega_i$ is the rotational velocity of particle *i*, $F_{ij}^c$ is the contact force and $M_{ij}^c$ is the contact moment acting on particle *i* by particle *j* or boundary conditions, $F_{ik}^{nc}$ is the non-contact force acting on particle *i* by particle *k* (for example, capillary forces) or other sources, $F_i^f$ is the particle-fluid interaction force on particle *i*, $F_i^g$ is the gravitational force, and $t$ is time. The derivatives of translational and rotational velocities with respect to time are the translational and rotational accelerations of the particle.

The computational algorithm used in this study calculates the right-hand side of Equation 2-1 as the resultant force on each particle for each time step. This force has three values (for each particle), one in each the *x*, *y*, and *z* directions, which will be called $F_i^{tx}$, $F_i^{ty}$, and $F_i^{tz}$, respectively, for time step *t*. After these resultant forces are calculated, they are divided by the mass of the particle to obtain the accelerations of the particle in the *x*, *y*, and *z* directions for time step *t*. Similarly, the right-hand side of Equation 2-2 is calculated as the resultant moment on each particle for each time step about the *x*, *y*, and *z* axes, $M_i^{tx}$, $M_i^{ty}$, and $M_i^{tz}$ respectively, and then these are divided by the moment of inertia of the particle to obtain the rotational accelerations. The

accelerations are given by $a_i^{tx}$, $a_i^{ty}$, and $a_i^{tz}$, translational, and $\dot{\omega}_i^{tx}$, $\dot{\omega}_i^{ty}$, and $\dot{\omega}_i^{tz}$, rotational, and are defined as

$$\mathbf{a_i^{tj}} = \frac{\mathbf{F_i^{tj}}}{\mathbf{m_i}} \qquad \text{[Equation 2-3]}$$

$$\dot{\boldsymbol{\omega}}_\mathbf{i}^{\mathbf{tj}} = \frac{\mathbf{M_i^{tj}}}{\mathbf{I_i}} \qquad \text{[Equation 2-4]}$$

where *j* goes from 1 to 3, with 1=*x*, 2=*y*, and 3=*z*. This nomenclature is used throughout the rest of this dissertation.

In terms of structural dynamics nomenclature for discrete systems, the terms associated with mass density are contained in the mass matrix, which is a diagonal matrix containing only non-zero entries on the diagonal (essentially the same as lumped mass matrices used in the finite element method). Computational space is reduced if the mass of each particle is saved in a Nx1 array, where N is the number of particles, instead of a NxN array with non-zero values only existing on the diagonals. Therefore, the acceleration of each particle can be solved separately instead of having to solve a system of equations simultaneously. This is a significant difference between modeling a collection of particles and, for example, a continuous structural system where the mass matrix is not diagonal.

The velocities of particle *i* for time step *t* in the *x*, *y*, and *z* directions, $v_i^{tx}$, $v_i^{ty}$, and $v_i^{tz}$, translational, and $\omega_i^{tx}$, $\omega_i^{ty}$, and $\omega_i^{tz}$, rotational, respectively, can then be calculated using

$$\mathbf{v_i^{tj}} = \mathbf{v_i^{(t-1)j}} + \mathbf{a_i^{tj}dt} \qquad \text{[Equation 2-5]}$$

$$\boldsymbol{\omega}_\mathbf{i}^{\mathbf{tj}} = \boldsymbol{\omega}_\mathbf{i}^{\mathbf{(t-1)j}} + \dot{\boldsymbol{\omega}}_\mathbf{i}^{\mathbf{tj}}\mathbf{dt} \qquad \text{[Equation 2-6]}$$

where $v_i^{(t-1)j}$ and $\omega_i^{(t-1)j}$ are the initial translational and rotational velocities of particle *i* at the beginning of the time step (also the final velocities from the previous time step) and *dt* is the value

of the time increment for the time step, in seconds. The initial velocities are equal to zero during the first time step, unless a non-zero initial velocity for a particle is specified. At the end of each time step, $v_i^{tx}$, $v_i^{ty}$, $v_i^{tz}$, $\omega_i^{tx}$, $\omega_i^{ty}$, and $\omega_i^{tz}$ are saved as the initial velocities for the next time step.

Next, the translational distances that the center of each particle travels in the time step, $d_i^{tx}$, $d_i^{ty}$, and $d_i^{tz}$, in the *x*, *y*, and *z* directions, respectively, are calculated using

$$\mathbf{d_i^{tj}} = \mathbf{v_i^{tj}dt} \quad \text{[Equation 2-7]}$$

The angles of rotation of the edges of each particle, $\theta_i^{tx}$, $\theta_i^{ty}$, and $\theta_i^{tz}$, in the *x*, *y*, and *z* directions, respectively, with radius $R_i$ are calculated using

$$\boldsymbol{\theta_i^{tj}} = \frac{\boldsymbol{\omega_i^{tj}dt}}{\mathbf{R_i}} \quad \text{[Equation 2-8]}$$

Finally, the positions and edge locations of the particles are updated by adding the distances moved to the final locations of the previous time step, $x_i^t$, $y_i^t$, and $z_i^t$, using

$$\mathbf{x_i^t} = \mathbf{x_i^{t-1}} + \mathbf{d_i^{tx}} \quad \text{[Equation 2-9]}$$

$$\mathbf{y_i^t} = \mathbf{y_i^{t-1}} + \mathbf{d_i^{ty}} \quad \text{[Equation 2-10]}$$

$$\mathbf{z_i^t} = \mathbf{z_i^{t-1}} + \mathbf{d_i^{tz}} \quad \text{[Equation 2-11]}$$

Assigning the *x*, *y*, and *z* locations of each particle to a time step is essential, because issues will arise when the location of a particle is updated mid time step (i.e. after particle-particle contact is calculated for another particle), before the particle is analyzed in the force summation loop. Because the forces, and subsequently the accelerations, velocities, and distances, are direction defined, negative values automatically follow through the calculations and the positions are correctly updated. These calculations are repeated for every time step.

One issue that needs to be resolved in any computational scheme is determining the appropriate value for *dt*. In general, this can be of any arbitrary magnitude. However, this value

must not exceed the critical time increment that has been determined (O'Sullivan, 2011) and (Sheng et al., 2004), and used by commercial software TRUBAL and EDEM, beyond which solutions can potentially be unstable. The main reason for the instability that arises is that discrete element modelling does not consider disturbances, say from one particle colliding with another, propagating further than the immediate neighbors of the particle. Therefore, if the time increment is sufficiently small, an assumption can be made that the force propagation is negligible compared to the other forces in the system (Zhu et al., 2007). This assumption is used by Cundall and Strack (1979) and greatly reduces the memory requirements for DEM simulations. The limiting time increment is defined as dtcrit, which is defined for DEM simulations with spheres and a Hertzian contact model by (Sheng et al., 2004)

$$\mathbf{dt_{crit}} = \frac{\pi \mathbf{R_{min}}}{\alpha}\sqrt{\frac{\rho}{G}} \qquad \text{[Equation 2-12]}$$

where $R_{min}$ is the minimum radius of all particles in the simulation and $\rho$ and $G$ are the density and the shear modulus of that smallest particle. If there are multiple particles with the minimum radius and are composed of different materials, all values for density and shear modulus should be checked so that the smallest time step will be calculated. Finally, $\alpha$ is defined by (Sheng et al., 2004)

$$\boldsymbol{\alpha = 0.1631\nu + 0.876605} \quad \text{[Equation 2-13]}$$

where ν is the value of the Poisson's ratio for the most critical material of the smallest particles. Equation 2-12 is derived from the Rayleigh wave surface velocity equation, with α being the root of an eighth order equation and approximated with Equation 2-13 (Sheng et al., 2004), therefore the critical time step calculated with Equation 2-12 is also referred to as the Raleigh time step (Bossy & Safuryn, 2016). The critical time step increases with increased minimum radius and density of the material. If very small particles are being used in the simulation, density scaling may

be appropriate to increase the minimum time increment and make the run times more reasonable (O'Sullivan, 2011).

The Raleigh time step does not take into account the relative movement of particles and the value may turn out to still be too large to ensure numerical stability. Therefore, if relative velocities between particles are very high and numerical instability occurs, the time step should be reduced further. The Raleigh time step is only an approximation and therefore a fraction of the value is typically used in simulations (Bossy & Safuryn, 2016). Using a small fraction of the Raleigh time step for the simulations will greatly increase the simulation time, therefore a balance must be found and for high relative velocities between particles. This balance is typically a time step that is 20% of the Raleigh time step (Bossy & Safuryn, 2016).

**Particle Shape**

Spheres are by far the most common type of particle shape used in three-dimensional DEM analyses (O'Sullivan, 2011). Spheres possess the simplest and most efficient method of contact detection, which significantly decreases the simulation time (Bossy & Safuryn, 2016). There are simple calculations to determine if a sphere is in contact with other spheres or with boundaries. Even ellipsoids, having relatively simple geometry, involve solving a non-linear equation to solve contact resolution (O'Sullivan, 2011). Determining what to use for the shape of the particles causes the analyst to trade between computational cost and physical practicality. For these reasons, spheres were chosen for the simulations performed with this DEM model.

## User Inputs

The execution of any DEM simulation requires that the following variables must generally be known:

- Number of particles
- Number of time steps
- Time increment for each time step
- Boundary conditions
- Gravity magnitude and direction
- Friction coefficients between particles and between particles and rigid walls
- Global damping coefficient
- Individual particle properties, including particle density, Young's modulus, shear modulus, and Poisson's ratio
- Damping coefficient for particle-particle contact forces

## Contact Forces between Particles

### *Contact Detection Algorithm*

To save computational time, the discrete element model uses a contact detection algorithm to determine which particles are near enough to be checked for physical contact. This allows for only the particles that are near each other to go through the contact force loop instead of every particle being checked with every other particle in the packing. One way of looking at the amount of time that can be saved is to imagine a person only having to say hello to all of their immediate neighbors, instead of every other person on the planet. The requirements for a contact detection

algorithm are reliability, ease of implementation, and time and memory efficiency (Munjiza, 2004).

This discrete element model uses a grid based algorithm, similar to the method proposed by Munjiza (2004). The algorithm developed here assigns cell numbers to every particle and then only checks particles in the same or adjacent cells for contact. The grid is automatically split into equally sized cells with size calculated as a function of the maximum particle radius present in the simulation. For example, depending on the initial geometry of the simulation, the grid could be composed of 1,000 cells with a 10x10x10 cell structure. Basing the cell sizes off of the actual radii of the particles being simulated, as opposed to making the size of the cells a user input or just a constant value, makes the algorithm more efficient. This is an advantage, because the algorithm is written to optimize the size of the cells to ensure all particle contacts will be detected while also minimizing the number of particle-particle contact checks performed in the program, thereby saving computational time.

One aspect that could be seen as a "limitation" of this contact detection algorithm is that all of the cells are the same lengths in the *x*, *y*, and *z* directions. This would only be a limitation if a very specific problem is being run, for example, a problem with geometry of very large sized particles on one side of a boundary and very small sized particles on the other side. Even in this case, the contact detection algorithm will still work; however, technically the algorithm could be more time efficient if the cells could be different sizes (e.g. smaller sized cells containing the smaller particles will allow for less contact checks). This is a very specific problem and for the analyses presented in this dissertation (along with the vast majority of DEM research problems), the fact that the cells are all the same size is not a limitation. The primary physical limitation is that cells should not be smaller than the size of the largest particle (O'Sullivan, 2011).

*Normal Contact Forces*

Once two particles are found to be in the same or adjacent cells by the contact detection algorithm, the distance between the particles is calculated. The overlap behavior of two particles coming into contact can be seen in Figure 2-2. If the particles are in contact with one another, particle contact forces exist as the particles deform. In the DEM simulations modeled for this research, particles do not actually deform the way they would in real life, but the amount of overlap is accurately controlled to mimic the real world elastic deformations (Padros & Kokocinska, 2016). This is considered a soft-sphere method of discrete element modeling, as opposed to hard-sphere which does not allow for any overlap. The soft-sphere approach allows for both normal and tangential forces to be more accurately evaluated and is the most common approach used in current practice (Bossy & Safuryn, 2016).

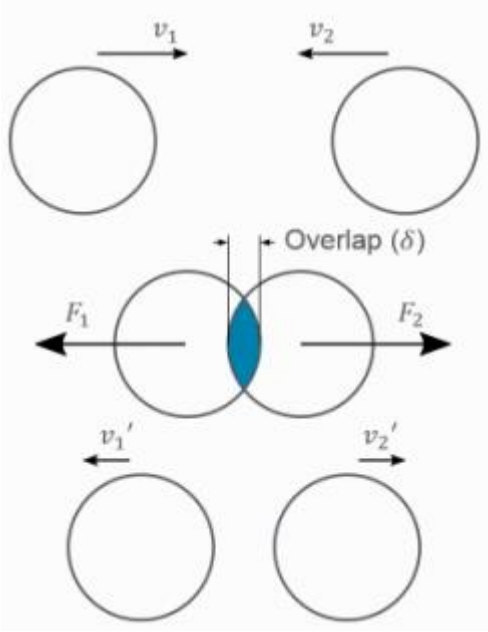


Figure 2-2: Soft-sphere approach allowing overlap between two contacting particles (Bossy & Safuryn, 2016).

In Figure 2-2, two particles with known velocities come into contact with each other. Forces develop, acting in opposite directions, on the particles as a function of the amount of overlap

between the particles, calculated based off the locations of the centers and the known radii values. The force calculations are dependent on the chosen contact model being used in the DEM simulation.

A number of different contact models exist that can accurately model realistic material behavior. The simplest types of contact models assume that the contact between two particles, which is in fact a very complex nonlinear problem of solid mechanics, can be represented by a linear spring with stiffness $K_n$ that exists between two particles as they come in contact with one another. Because the linear spring stiffness does not have an easily intuitive relationship with respect to the known properties of the particle, models have been developed to link the stiffness to the physical particle material properties. This DEM model uses a simplified Hertzian contact model, with stiffness for time step *t*, $K_n^t$, calculated by (O'Sullivan, 2011)

$$\mathbf{K_n^t} = \left(\frac{\mathbf{2\langle G\rangle\sqrt{2\langle R\rangle}}}{\mathbf{3(1-\langle \nu\rangle)}}\right)\sqrt{\boldsymbol{\delta}_\mathbf{n}^\mathbf{t}} \qquad \text{[Equation 2-14]}$$

where, for sphere-sphere contact, the coefficients are calculated as (O'Sullivan, 2011)

$$\langle \mathbf{R}\rangle = \frac{\mathbf{2R_AR_B}}{\mathbf{R_A+R_B}} \qquad \text{[Equation 2-15]}$$

$$\langle \mathbf{G}\rangle = \frac{\mathbf{1}}{\mathbf{2}}(\mathbf{G_A} + \mathbf{G_B}) \qquad \text{[Equation 2-16]}$$

$$\langle \boldsymbol{\nu}\rangle = \frac{\mathbf{1}}{\mathbf{2}}(\boldsymbol{\nu}_\mathbf{A} + \boldsymbol{\nu}_\mathbf{B}) \qquad \text{[Equation 2-17]}$$

$$\boldsymbol{\delta}_\mathbf{n}^\mathbf{t} = \mathbf{R_A} + \mathbf{R_B} - \mathbf{d_{AB}^t} \qquad \text{[Equation 2-18]}$$

Here $R$ is the sphere radius, $G$ is the elastic shear modulus, $\nu$ is the Poisson's ratio, and the subscripts *A* and *B* refer to two spheres, *A* and *B*, in contact. Lastly, $\delta_n^t$ is the sphere overlap for time step *t*, with $d_{AB}^t$ being the distance between the centers of the two particles at time step *t*, and calculated by

$$\mathbf{d_{AB}^t} = \sqrt{\mathbf{d_{xAB}^t}^2 + \mathbf{d_{yAB}^t}^2 + \mathbf{d_{zAB}^t}^2} \qquad \text{[Equation 2-19]}$$

where $d_{xAB}^t$, $d_{yAB}^t$, and $d_{zAB}^t$ are the *x*, *y*, and *z* distances between the centers of the particles, respectively, during time step *t*, and calculated by

$$\mathbf{d_{xAB}^t} = \mathbf{x_A^t} - \mathbf{x_B^t} \qquad \text{[Equation 2-20]}$$

$$\mathbf{d_{yAB}^t} = \mathbf{y_A^t} - \mathbf{y_B^t} \qquad \text{[Equation 2-21]}$$

$$\mathbf{d_{zAB}^t} = \mathbf{z_A^t} - \mathbf{z_B^t} \qquad \text{[Equation 2-22]}$$

The equations represented above amount to an effort to replicate the actual deformation between two elastic spheres with a relative simple one-dimensional relationship rather than using the full equations of three-dimensional elasticity.

The normal contact forces between the particles in the *x*, *y*, and *z* directions, $F_{nx}^t$, $F_{ny}^t$, and $F_{nz}^t$, respectively, for time step *t* are calculated as (O'Sullivan, 2011)

$$\mathbf{F_{nj}^t} = \mathbf{K_n^t \delta_n^t} \frac{\mathbf{d_{jAB}^t}}{\mathbf{d_{AB}^t}} \qquad \text{[Equation 2-23]}$$

The magnitude of the distance between the particles, $d_{AB}^t$, is always positive, but $d_{xAB}^t$, $d_{yAB}^t$, and $d_{zAB}^t$ can be positive or negative depending on the location of the particles relative to each other. Therefore, the directions of the forces are constantly updated.

The simplified Hertzian contact model is effective for use in DEM simulations because the model provides a logical basis for the link between spring stiffness and actual material properties. Also, in general, the model can provide very efficient and accurate calculations for non-cohesive granular materials (Bossy & Safuryn, 2016).

*Tangential Contact Forces*

This DEM model uses a simplified Mindlin-Deresiewicz tangential contact model, where the tangential stiffness for time step *t*, $K_t^t$ (Mindlin & Deresiewicz, 1953) and (Vu-Quoc et al., 2000) is calculated as

$$\mathbf{K_t^t} = \mathbf{K_n^t}\left(\frac{\mathbf{2(1-\langle \nu \rangle)}}{\mathbf{2-\langle \nu \rangle}}\right) \quad \text{[Equation 2-24]}$$

Because the Poisson's ratios of the particles are a constant, the ratio between normal and tangential stiffnesses is a constant throughout the simulation. The tangential forces are calculated as (O'Sullivan, 2011)

$$\mathbf{F_{tj}^t}\left(\boldsymbol{\delta_t}, \dot{\boldsymbol{\delta}}_\mathbf{t}\right) = \mathbf{K_t^t}\int_{\mathbf{t_c^0}}^{\mathbf{t}} \dot{\boldsymbol{\delta}}_\mathbf{t}\mathbf{dt} \quad \text{[Equation 2-25]}$$

where $\dot{\delta}_t$ is the relative velocity between the particles at time *t*. The integral in Equation 2-25 is approximated by the summation

$$\int_{\mathbf{t_c^0}}^{\mathbf{t}} \dot{\boldsymbol{\delta}}_\mathbf{t}\mathbf{dt} \approx \sum_{\mathbf{t_c^0}}^{\mathbf{t}} \dot{\boldsymbol{\delta}}_\mathbf{t}\triangle\mathbf{t} \quad \text{[Equation 2-26]}$$

and the relative velocity between the particles at time *t* is given by (O'Sullivan, 2011)

$$\dot{\boldsymbol{\delta}}_\mathbf{i} = \left[\mathbf{v_i^b} + \mathbf{e_{ijk}}\boldsymbol{\omega}_\mathbf{j}^\mathbf{b}\left(\mathbf{x_k^C} - \mathbf{x_k^b}\right)\right] - \left[\mathbf{v_i^a} + \mathbf{e_{ijk}}\boldsymbol{\omega}_\mathbf{j}^\mathbf{a}\left(\mathbf{x_k^C} - \mathbf{x_k^a}\right)\right] \quad \text{[Equation 2-27]}$$

where $e_{ijk}$ is the permutation tensor, $v$ and $\omega$ are the translational and rotational velocities, respectively, of particles *a* and *b*, $x^a$ and $x^b$ are the components of the particle centroids, and $x^C$ are the contact coordinates. The tangential component is then calculated by subtracting the normal component of the relative velocity vector as (O'Sullivan, 2011)

$$\dot{\boldsymbol{\delta}}_\mathbf{i}^\mathbf{t} = \dot{\boldsymbol{\delta}}_\mathbf{i} - \dot{\boldsymbol{\delta}}_\mathbf{j}\mathbf{n_j}\mathbf{n_i} \quad \text{[Equation 2-28]}$$

The tangential forces are limited by a Coulomb friction criteria and are given by (O'Sullivan, 2011)

$$\mathbf{F_{tj}^t = -min\left(\left|\mu F_{nj}^t\right|, F_{tj}^t\left(\delta_t, \dot{\delta}_t\right)\right)\frac{\dot{\delta}_t}{|\dot{\delta}_t|}} \qquad \text{[Equation 2-29]}$$

where μ is the friction coefficient between the particles. The tangential forces are then added to the normal forces and also cause moments about the centers of the particles.

The computational difficulty with the tangential forces is that the tangential displacements must be incrementally summed during the simulation for Equation 2-26. Therefore, the tangential displacements between particles at every contact must be saved, creating three NxN matrices, for *x*, *y*, and *z* directions, with N number of particles. This increases computational time. For the larger three-dimensional slope simulations described later, this computational time increase was significant. Therefore, a new way to store the incremental tangential displacements was written for the model. A maximum number of particle contacts for each particle is assumed as "Ncontact" (i.e. a particle can only be in contact with Nconcact other particles). The information contained in what were the three NxN matrices can now be stored in three NxNcontact matrices. This storage strategy essentially gets rid of all the zero entries between non-contacting particles and has greatly reduced the computational run times required for simulations with a large number of particles.

For mostly static simulations, the tangential force contributions can be negligible because the summed tangential displacements are almost zero. However, because the research performed here is investigating behavior after particles begin to roll, the tangential model is used during all simulations.

Once a particle is found to be in contact with another particle, the forces between them in the *x*, *y*, and *z* directions are calculated only once for that time step and then stored with the same magnitude but in the opposite directions for the other particle.

**Non-contact Forces between Particles**

When the particles in a DEM simulation are small in size (fine) and/or moisture exists, non-contact forces between particles can significantly affect the packing and flow behavior of the particles (Zhu et al., 2007) and should also be included in the simulation calculations. Non-contact forces are forces that exist between particles even though they are not physically in contact. Quantitatively simulating these forces can be particularly difficult outside of the DEM. However, the DEM overcomes these difficulties by directly considering the sum of individual forces on each particle. Examples of non-contact forces include van der Waals, capillary, and electrostatic forces. These can occur concurrently or independently depending on the circumstances and will be explained in the following text. A comparison of the magnitudes of common non-contact forces between particles is shown in Figure 2-3 (Rumpf, 1962).

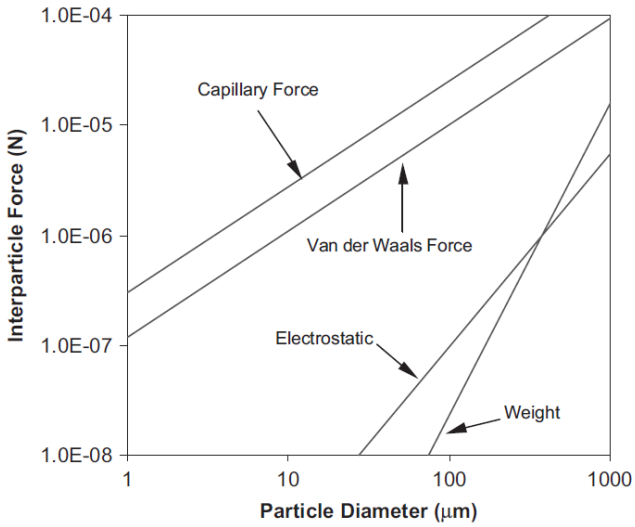


Figure 2-3: Comparison of magnitudes of common non-contact forces between particles (Rumpf, 1962) Calculations based on van der Waals with Hamaker constant, A, equal to 6.5 x 10-20 J and the surface gap between two spheres, h, equal to 1.65 Å, capillary force with liquid surface tension, γ, of water equal to 72.8 x 10-2 Nm-1, electrostatic forces with εr equal to 1, and weight with density, ρg, equal to 3 x 103 kg/$m^3$.

Electrostatic forces exist between charged particles. As can be seen from Figure 2-3, electrostatic forces are generally at least one order of magnitude below van der Waals and capillary

forces for particles with diameters below 1000 microns. Hence for this DEM model, they are ignored.

*Van der Waals Forces*

The Hamaker theory (Hamaker, 1937) is usually used to calculate van der Waals forces in DEM simulations (Zhu et al., 2007). This theory quantifies molecular dipole interactions between individual atoms and calculates the van der Waal forces, $F_{vanx}^{t}$, $F_{vany}^{t}$, and $F_{vanz}^{t}$, in the *x*, *y*, and *z* directions, respectively, for time step *t* with (Zhu et al., 2007)

$$\mathbf{F_{vanj}^{t}} = -\left(\frac{\mathbf{A d_{ave}}}{\mathbf{24 h^{t2}}}\right)\frac{\mathbf{d_{jAB}^{t}}}{\mathbf{d_{AB}^{t}}} \qquad \text{[Equation 2-30]}$$

where *A* is the Hamaker constant (Joules = N·m), $h^t$ is the surface gap between two spheres during time step *t*, $d_{AB}^{t}$, $d_{xAB}^{t}$, $d_{yAB}^{t}$, and $d_{zAB}^{t}$ have been previously defined, and $d_{ave}$ is the average particle diameter between particles *A* and *B* calculated by

$$\mathbf{d_{ave}} = \frac{\mathbf{1}}{\mathbf{2}}(\mathbf{d_A} + \mathbf{d_B}) \qquad \text{[Equation 2-31]}$$

The Hamaker constant is the only variable in Equation 2-30 that is not explicitly known. This constant depends on several variables related to the number of atoms per unit volume in the two bodies and the coefficient in the atom-atom pair potential (Israelachvili, 1991). Evaluating the effects of each of these properties is difficult (Zhu et al., 2007), but this DEM model uses a lumped parameter determined empirically for the value of the Hamaker constant as 6.5 x $10^{-20}$ J (Rumpf, 1962), (Yang et al., 2000), and (Dong et al., 2006).

As can be seen from Equation 2-30, the van der Waals force goes to infinity as the particles come closer and closer together (as $h^t$ goes to zero). This is avoided in this DEM model (and also most other DEM codes (Zhu et al., 2007)) by specifying a cut-off distance where the force is no

longer calculated. In this DEM model, the cut-off distance is specified at 1 nm, but according to published research this value can range from 0.165 nm to 1 nm (Krupp, 1967), (Israelachvili, 1991), (Yen & Chaki, 1992), and (Yang et al., 2000). There would be a high computational cost in calculating the van der Waals force between each particle and every other particle. As can be seen from Equation 2-30, two particles farther apart than 10 nm have a van der Waals force lower by two orders of magnitude than the van der Waals forces at the 1 nm cut-off distance. For this reason, another cut-off distance of 10 nm is specified where the van der Waals force between particles this distance apart or greater are no longer calculated. In summary, this DEM model can calculate van der Waals forces between particles that are 1-10 nm apart.

*Capillary Forces*

Capillary forces are associated with surface tensions at solid, liquid, and/or gas interfaces. One example of when capillary forces could be considered in a simulation are those between soil particles in contact with water in the soil. The capillary forces on a particle for time step *t* can be rather difficult to calculate and the fundamental equation is given as (Zhu et al., 2007), (Lian et al., 1993), (Gladkyy & Schwarze, 2014), and (Weigert & Ripperger, 1999)

$$\mathbf{F_{cap}^{t} = -(2\pi\gamma R \sin(\beta^{t}) \sin(\vartheta + \beta^{t}) + \pi R^{2} \Delta p^{t} \sin^{2}(\beta^{t}))} \qquad \text{[Equation 2-32]}$$

where $\gamma$ is the liquid surface tension (N/m), $\beta^t$ is the half-filling angle at time step *t*, $\vartheta$ is the contact angle between two particles, $\Delta p^t$ is the difference between the pressure outside and inside the liquid bridge at time step *t*, and *R* is the effective radius between the two particles, calculated by (Gladkyy & Schwarze, 2014)

$$\mathbf{R = \frac{2R_i R_j}{R_i + R_j}} \qquad \text{[Equation 2-33]}$$

where $R_i$ and $R_j$ are the radii of particles $i$ and $j$, respectively, shown in Figure 2-4.

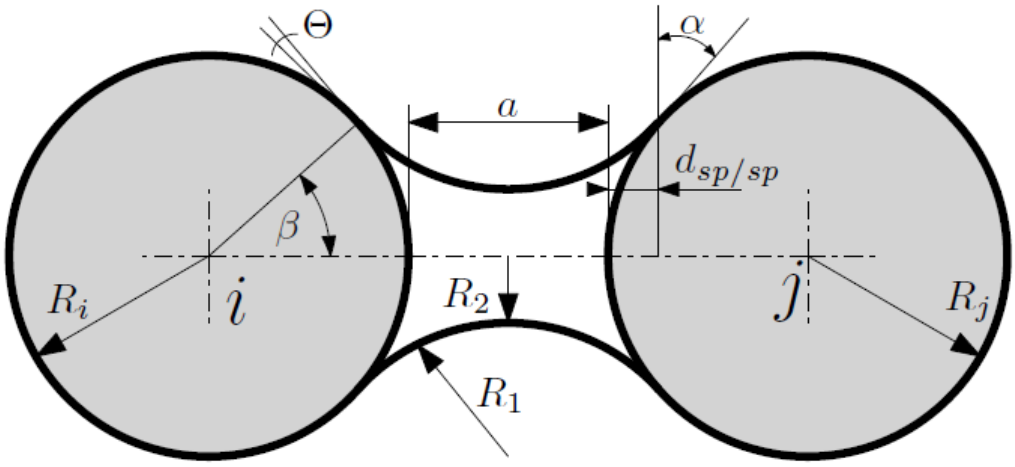


Figure 2-4: Diagram of two spheres in contact showing the liquid bridge resulting in a capillary force (Gladkyy & Schwarze, 2014)

The first portion of Equation 2-32 is contribution from the liquid surface tension and the second portion is the hydrostatic pressure component (Lian et al., 1993). The term $\Delta p^t$ is what makes Equation 2-32 so difficult to calculate and is given by the Laplace-Young equation (Lian et al., 1993)

$$\Delta \mathbf{p^t} = \frac{\gamma}{\mathbf{R_{ave}}}\left(\frac{\ddot{Y}}{(1+\dot{Y}^2)^{\frac{3}{2}}} - \frac{1}{Y(1+\dot{Y}^2)^{\frac{1}{2}}}\right) \qquad \text{[Equation 2-34]}$$

where $Y$ is a dimensionless coordinate with respect to the sphere radius and the dot notation refers to differentiations with respect to $X$ (Lian et al., 1993).

Approximations are almost always used to solve Equation 2-34 and they depend on the size of the particles and liquid surface tension. For the size of particles appropriate for future simulations using this model, the Weigert model, commonly used in DEM simulations (Gladkyy & Schwarze, 2014), was chosen for the capillary force calculations. Hence $\Delta p^t$ is approximated by (Weigert & Ripperger, 1999)

$$\Delta \mathbf{p^t} \approx \boldsymbol{\gamma}\left(\frac{\mathbf{1}}{\mathbf{R_1^t}} + \frac{\mathbf{1}}{\mathbf{R_2^t}}\right) \quad \text{[Equation 2-35]}$$

where $R_1^t$ and $R_2^t$ are the principal radii of the bridge curvature for time step *t*, are taken positive and negative, respectfully, and calculated by (Weigert & Ripperger, 1999)

$$\mathbf{R_1^t} = \left|\frac{\mathbf{R(1-\cos(\beta^t))+a^t}}{\mathbf{\cos(\beta^t+\vartheta)}}\right| \quad \text{[Equation 2-36]}$$

$$\mathbf{R_2^t} = -|\mathbf{R\sin(\beta^t)} + \mathbf{R_1^t[\sin(\beta^t+\vartheta)-1]}| \quad \text{[Equation 2-37]}$$

where $\mathbf{a^t}$ is the surface distance between the two particles for time step *t* and all parameters are shown in Figure 2-4. The absolute value signs in Equations 2-36 and 2-37 force the signs of $R_1^t$ and $R_2^t$ appropriately for Equation 2-35 (Weigert & Ripperger, 1999). The last of the variables needed for the above equations are the half-filling and contact angles. The contact angle varies based on the material properties of the particles and the liquid. For most published studies, a contact angle of 0° is used. Changing this value does not change the final capillary force significantly, especially compared to the magnitudes of other forces present in the analyses; therefore a contact angle of 0° is quantified in the model but can be specified to a different value if desired. The half-filling angle is calculated, using an assumed given liquid bridge volume between particle *i* and *j*, $V_{ij}$, with (Gladkyy & Schwarze, 2014)

$$\boldsymbol{\beta^t} = \mathbf{arcsin}\left(\frac{\mathbf{V_{ij}}}{\mathbf{0.12(2R)^3 C_a^t C_\vartheta}}\right)^{\mathbf{1/4}} \quad \text{[Equation 2-38]}$$

where $C_a^t$ and $C_\vartheta$ are correction functions for the surface distance between the particles at time step *t* and the contact angle, respectively, and they are calculated by (Gladkyy & Schwarze, 2014)

$$\mathbf{C_a^t} = \left(\mathbf{1} + \mathbf{6}\frac{\mathbf{a^t}}{\mathbf{2R}}\right) \quad \text{[Equation 2-39]}$$

$$\mathbf{C_\vartheta} = (\mathbf{1} + \mathbf{1.1\sin\vartheta}) \quad \text{[Equation 2-40]}$$

Several methods for calculating capillary forces solve for the liquid bridge volume as a function of the half-filling angle when the angle is known. However, for DEM simulations, the

liquid bridge volume is commonly treated as a known value because the volume of liquid in the simulation is known. As an example for future simulations performed with this DEM model that consider forces on a soil slope from a rainstorm event, the raindrop locations will be randomly assigned. The volume of liquid per rain drop can be divided evenly and distributed to the particles either in contact with the drop or neighboring the particles in contact with the drop, yielding a known liquid bridge volume for each pair of particles with a capillary force.

Similar to the van der Waals forces, there is a cut-off distance where capillary forces no longer exist. This distance is referred to as the critical surface distance and represents the physical distance where the liquid bridge would rupture. Because the liquid bridge volume between the two particles is a known value, the critical surface distance $a_{crit}$ is also calculated as a function of the volume, with (Weigert & Ripperger, 1999)

$$\mathbf{a_{crit} = (1 + 0.5\vartheta)V_{ij}^{\frac{1}{3}}} \qquad \text{[Equation 2-41]}$$

Equation 2-41 is only valid for $\vartheta$ values less than 40° (Weigert & Ripperger, 1999), which is appropriate for all analyses here. This critical distance is almost always larger than distances between particles for the analyses performed in this dissertation; however the formula is given here for completeness and is included in the DEM code.

Finally, multiplying Equation 2-32 by the direction components yields the capillary forces on a particle, $F_{capx}^{t}$, $F_{capy}^{t}$, and $F_{capz}^{t}$, in the *x*, *y*, and *z* directions, respectively, for time step *t* as

$$\mathbf{F_{capj}^{t} = -(2\pi\gamma R\sin(\beta^{t})\sin(\vartheta + \beta^{t}) + \pi R^{2}\Delta p^{t}\sin^{2}(\beta^{t}))\frac{d_{jAB}^{t}}{d_{AB}^{t}}} \qquad \text{[Equation 2-42]}$$

**Boundary Conditions**

Three different types of boundary conditions are considered: periodic boundary conditions,

rigid wall boundary conditions, and one boundary condition novel to this DEM model, called a save-mass boundary condition. For calculations performed using this DEM model, the plane equation of the boundary condition must be input in the following form:

$$\mathbf{ax + by + cz + d = 0} \qquad \text{[Equation 2-43]}$$

During each time step, the distances between each particle and each boundary condition are calculated. If a particle is in contact with a boundary, the forces or displacement relationship between the particle and the boundary are calculated. These forces and displacement relationships are described in the following text for each boundary condition type.

*Periodic Boundary Conditions*

Periodic boundaries allow the simulation of a very large number of particles while considering a much smaller subdomain. This subdomain is assumed to be surrounded by identical sub-packings. Using periodic boundary conditions for DEM simulations can be very advantageous for decreasing the number of particles in the simulation, thereby decreasing the computational time. Periodic boundaries are especially useful when modeling soils where repeated sections of material with nearly identical properties and geometries can be expected. Essentially, knowing how one section of the soil is going to behave during the analysis allows one to predict how the surrounding soil will behave as well. An example of a two-dimensional case where periodic boundaries can be used is shown in Figure 2-5. In this figure only side by side periodic boundaries are shown by the dashed vertical lines; however, top to bottom periodic boundaries can be modeled as well.

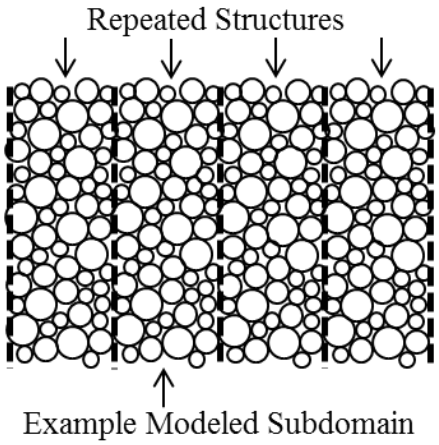


Figure 2-5: Example of side to side periodic boundary structure

If a particle exits through one side of a periodic boundary, then because the subdomain is surrounded by identical subdomains, an assumption is made that an identical particle will enter through the opposite side. This relationship is shown in Figure 2-6. As particle 1 exits periodic boundary A-A, an identical particle 1' enters periodic boundary B-B. This behavior continues for all example particles shown in Figure 2-6.

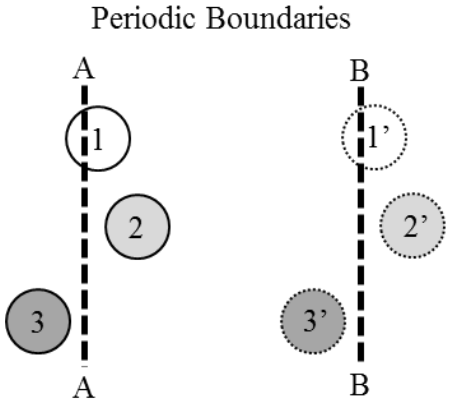


Figure 2-6: Example particle behavior with side to side periodic boundaries

In this study, if a boundary condition is labeled as periodic and a particle is determined to be outside the boundary, then the maximum *x*, *y*, or *z* dimensions are added or subtracted to the current location of the particle. This essentially "moves" the particle to the opposite side of the analysis domain for the next time step.

*Rigid Wall Boundary Conditions*

To determine if a particle, *i*, is in contact with a rigid wall, the distance between the center of the particle and the rigid wall boundary condition at time step *t*, $d_{iBC}^{t}$, is calculated using (O'Sullivan, 2011)

$$\mathbf{d_{iBC}^{t}} = \frac{\mathbf{ax_i^t + by_i^t + cz_i^t + d}}{\sqrt{\mathbf{a^2 + b^2 + c^2}}} \qquad \text{[Equation 2-44]}$$

where *a*, *b*, *c*, and *d* are the components of the equation of the plane, from Equation 2-43, of the rigid wall boundary condition and $x_i^t$, $y_i^t$, and $z_i^t$, are the *x*, *y*, and *z* coordinates of the center of particle *i* in contact with the wall at time step *t*. This calculation method is widely accepted for a sphere-boundary contact (O'Sullivan, 2011). Rigid wall boundary conditions also apply if the walls are moving. If this is the case, *a*, *b*, *c*, and *d* are adjusted throughout the simulation. Care must be taken to ensure the time step increment is appropriate for how fast the wall is moving (i.e. a wall must not move too much in one time step to cause particle instability).

For rigid wall boundary conditions, the equation of the plane must give the unit normal vector in the direction pointing towards the particles being analyzed. This is because there is an "active" and "inactive" side of the wall and only one of them is physically correct. If the unit normal vector is pointing away, the calculations may be incorrect.

For a special case when a rigid wall barrier is located through the middle of a mass of particles, two rigid wall boundary conditions must be identified. They will have the same location in space but must have unit normal vectors in opposite directions. This will essentially cause both sides of the boundary to be "active."

If the distance between the center of the particle and the rigid wall is less than the radius of the particle, the particle is in contact with the wall. The normal and tangential forces on the

particles are calculated exactly the same as the particle-particle contact forces, but with the direction defined by the unit normal vector of the boundary condition. The contact stiffness is a function only of the particle material properties.

*Save-Mass Boundary Conditions*

The third boundary condition type is one created for this DEM model. The boundary condition has been named "save-mass" and is defined by a boundary where once a particle passes the boundary, the mass of the particle is saved, no further force calculations are performed for the particle, and the particle is essentially absent from the rest of the analysis. This boundary condition type was created, because during the analyses an important output parameter is how much soil mass is eroded. For the analyses completed for this research, a save-mass boundary is located at the bottom of the initial slope geometry. During the hydraulic flow event, the particles begin to slide down the slope. As more particles exit the save-mass boundary, the masses are summed to give a final totaled erosion mass at the end of the analysis.

Figure 2-7 shows a time stepping example of how this boundary condition works. In this example, the shaded particles, each with mass equal to 1 (ignoring units), are rolling down the top of the slope. In time step i, no particles have passed the save mass boundary shown by the dashed line to the right of the particle mass. In the next time step, one of the particles has passed the boundary and the mass of the particle has been saved. Finally, in the last time step shown, both particles have passed the boundary and the total erosion mass has been saved (1+1=2).

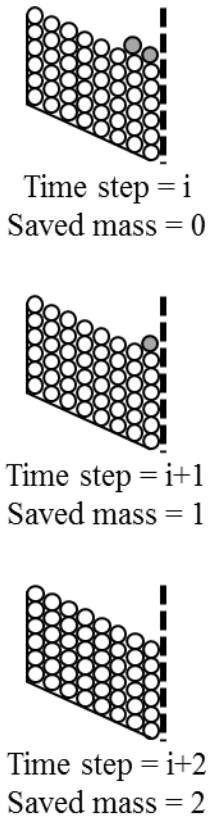


Figure 2-7: Save-Mass Boundary Condition Example

**Damping**

In the physical world, both energy losses from frictional heat and energy dissipation due to frictional sliding exist that are not taken into account in DEM simulations. Non-physical particle vibrations can also develop as a result of the elastic contact models used for the contact forces. Damping is used in the DEM to represent these issues.

Damping coefficients are required for the damping methods presented here and one problem with damping coefficients is that the values are hard to relate to any physical property, whether to a macro-property of the entire assembly or to any individual particle property. Ng (2006) discusses the sensitivity of DEM results to the damping coefficient used. Both the macro-

and micro-scale properties are affected. Therefore, clearly documenting what damping coefficient was used is important when presenting results and these details are given later for this research.

*Mass Damping*

Mass damping (also called global damping), originally proposed by Cundall and Strack (1979), is used for some of the simulations performed for this research. The damping is applied to the resultant velocities of each particle, changing Equations 2-5 and 2-6 to (O'Sullivan, 2011)

$$\mathbf{v_i^{tj}} = \left(\frac{\mathbf{v_i^{(t-1)j}(1-\alpha\triangle t/2)+a_i^{tj}dt}}{\mathbf{1+\alpha\triangle t/2}}\right) \qquad \text{[Equation 2-45]}$$

$$\boldsymbol{\omega_i^{tj}} = \left(\frac{\boldsymbol{\omega_i^{(t-1)j}(1-\alpha\triangle t/2)+\dot{\omega}_i^{tj}dt}}{\mathbf{1+\alpha\triangle t/2}}\right) \qquad \text{[Equation 2-46]}$$

where $\alpha$ is the mass damping coefficient.

*Local Non-viscous Damping*

Mass damping can introduce body forces, which can be inaccurate in flowing regions (O'Sullivan, 2011). Since hydraulically induced flow is one of the main topics studied here, an alternative damping system later proposed by Cundall (1987), local non-viscous damping, was chosen for simulations performed for this research.

The local non-viscous damping force for particle $p$, $F_d^p$, is calculated as (O'Sullivan, 2011)

$$\mathbf{F_d^p} = -\boldsymbol{\alpha}|\mathbf{F^p}|\mathbf{sgn}(\mathbf{v^p}) \qquad \text{[Equation 2-47]}$$

where α is the damping coefficient, $F^p$ is the resultant force acting on particle $p$, $v^p$ is the velocity vector for particle $p$, and $sgn(v^p)$ indicates to multiply by the sign of the velocity vector. This damping force is applied separately to each degree of freedom to yield three translational forces

and three rotational moments for each particle. This type of damping ensures that only accelerating motion is damped and that no erroneous damping forces are introduced during steady-state motion (Itasca, 2004). An advantage of this approach is that this is analogous to hysteretic damping and the energy loss per cycle is independent of the rate at which the cycle is executed (Itasca, 2004).

*Particle-particle contact damping*

As stated before, one problem with the simplified Hertzian contact model and all contact models that are elastic prior to yielding is that the energy dissipation that occurs physically is not captured in the model (O'Sullivan, 2011). The issue that arises is that if there is no yield by contact separation, the particles will continue to vibrate like a system of connected elastic springs. Particle-particle contact damping is used to relieve this issue. In this scenario, the damping forces, $F_{dampx}^{t}$, $F_{dampy}^{t}$, and $F_{dampz}^{t}$, in the *x*, *y*, and *z* directions, respectively, for time step *t* are simply a reduced contact force and calculated by

$$\mathbf{F_{dampj}^{t} = -\mu_c K_n^t \delta_n^t} \qquad \text{[Equation 2-48]}$$

where $\mu_c$ is the contact damping coefficient between the particles. Finally, Equation 2-23 is changed to include the damping force by

$$\mathbf{F_{nj}^{t} = \left(K_n^t \delta_n^t + F_{dampj}^{t}\right) \frac{d_{jAB}^{t}}{d_{AB}^{t}}} \qquad \text{[Equation 2-49]}$$

## Loads

*Gravitational Loads*

Gravity loading for the analyses considered in this study is significant and one of the primary forces on the individual particles. Gravity forces are easy to compute, require little

explanation, and are applied for all simulations.

*Hydraulic Forces*

Forces generated by water resulting from rainfall or overland flow are the primary loads affecting soil erosion. The hypotheses presented later in this dissertation are tested under overland flow conditions. In this context, overland flow is surface runoff that occurs when excess rainwater flows over the surface of a soil slope and this condition could be present for multiple reasons. For example, the soil could be hydrophobic, fully saturated, or the rain intensity could be so large that the water does not physically have enough time to infiltrate and starts to flow instead. Hydrophobic soils are water repellant and this can occur in burned soils because of water-repellent compounds released by burning plants (Ravi et al., 2009). When rainwater falls onto a hydrophobic soil during a rainfall event, the water collects and pools on the soil surface instead of infiltrating into the ground. This will cause overland flow to occur more quickly and cause higher erosion rates.

One simplification made for this research is that the particular reason that overland flow is initiated is not a concern; the assumption is simply made that overland flow has developed and is the driving force that moves the particles. One reason the assumption of overland flow is made is because the DEM model developed here does not have the capabilities of simulating the fluid itself, but rather only the forces on the particles from the fluid as a function of particle shape, sizes, and fluid properties. Therefore, more complicated fluid behavior would be much more difficult to model but is a possibility for future work.

The following equation was used to calculate the drag force on particle *i* at timestep *t*, $F_{drag_i}^{t}$, (Julien, 2010):

$$\mathbf{F^t_{drag_i}} = \frac{\mathbf{1}}{\mathbf{2}}\ \boldsymbol{\rho}\ \mathbf{V^2 C_d A_i} \qquad \text{[Equation 2-50]}$$

where $\rho$ is the density of the fluid (1,000 kg/m$^3$ for water), $V$ is the velocity of the fluid flow, $C_d$ is a shape factor (0.5 for spheres), and $A_i$ is the projected surface area perpendicular to flow of particle $i$ ($A_i = \pi R^2$ for spheres with radius $R$). To avoid sudden instabilities, simulations were performed with the velocity of flow linearly increasing until reaching a maximum value.

A schematic of the drag force applied to a particle is shown in Figure 2-8. The forces are applied on the surfaces of the particles and will also create a moment acting at the center of each of the surface particles about the axis into the plane. The assumption is made that the surface particles are submerged in water and that the buoyancy force will counteract the downward component of the drag force applied to these particles.

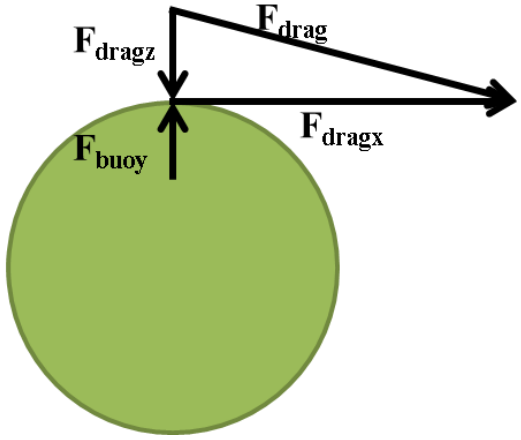


Figure 2-8: Drag Force from overland flow acting on the surface of a particle.

A surface particle identifying algorithm was written to decide which particles receive surficial drag forces. Details on the algorithm are described later in this dissertation with examples given on the actual particle slopes used for the simulations.

# Chapter 3 : VERIFYING THE DEM MODEL

Verifying a DEM model is essential (O'Sullivan, 2011). The research performed herein relies on verifying the DEM model with previously published results, simple analytical solutions, and experimental results. Force calculations and program performance were checked manually on simple cases (one or two particles, one boundary condition, and so forth) as the DEM code was constructed. The rest of this chapter details the benchmark tests that were used to verify the force calculations at the particle impact level.

## Benchmark Tests at Particle Impact Level

Chung and Ooi (2011) designed and proposed a set of eight benchmark tests for verifying DEM codes at a particle level for spherical contact and the tests are summarized in Table 3-1. The most commonly used commercial DEM software PFC3D and EDEM have been verified against Chung and Ooi's proposed benchmark tests.

Table 3-1: Summary of benchmark tests (Chung & Ooi, 2011)

| Test | Type of Test | Objective | Reference(s) |
|---|---|---|---|
| **1** | Elastic normal impact of two identical spheres | Check the elastic normal contact between two spheres | (Timoshenko & Goodier, 1970) |
| **2** | Elastic normal impact of a sphere with a rigid plane | Check the elastic normal contact between a sphere and a plane | (Timoshenko & Goodier, 1970), (Zhang & Vu-Quoc, 2002) |
| **3** | Normal contact with different restitution coefficients | Check the effect of damping ratio | (Ning & Ghadiri, 1996) |
| **4** | Oblique impact of a sphere with a rigid plane with a constant resultant velocity but at different incident angles | Check the tangential force calculation between a sphere and a plane | (Foerster et al., 1994), (Kharaz et al., 2001), (Renzo & Maio, 2004) |
| *5* | Oblique impact of a sphere with a rigid plane with a constant normal velocity but at different tangential velocities | Check the tangential force calculation between a sphere and a plane | (Maw et al., 1976), (Wu et al., 2003) |
| *6* | Impact of a sphere with a rigid plane with a constant normal velocity but at different angular velocities | Check the tangential force calculation between a sphere and a plane | (Vu-Quoc & Zhang, 1999) |
| **7** | Impact of two identical spheres with a constant normal velocity and varying angular velocities | Check the tangential force calculation between two spheres | (Chung, 2006) |
| *8* | Impact of two differently sized spheres with a constant normal velocity and varying angular velocities | Check the tangential force calculation between two spheres | (Chung, 2006) |

Because oblique impact at high velocity is not a concern for the simulations performed for this research, Tests 5, 6, and 8 are not used to verify the DEM model written for this research. The other five proposed benchmark tests, bolded in Table 3-1 (Tests 1, 2, 3, 4, and 7), are used to verify this DEM model. Two examples with differing materials were analyzed for each test. The titles of the tests are self-explanatory and only pertinent results are described in the following sub-sections of this dissertation. For the benchmark tests, the published results (Chung & Ooi, 2011) are first given and then the results for this DEM model are shown afterwards. Chung and Ooi give analytical solutions for Tests 1 and 2 and those are compared with the DEM solution. A more complete description of the reasoning for and details of each test are given by Chung and Ooi (2011). The input parameters used in the tests are shown in Table 3-2.

Table 3-2: DEM input parameters for benchmark tests (Chung & Ooi, 2011)

| **Input Parameters** | **Test 1** | | **Test 2** | | **Test 3** | |
|---|---|---|---|---|---|---|
| | Ex. 1 | Ex. 2 | Ex. 1 | Ex. 2 | Ex. 1 | Ex. 2 |
| | Glass | Limestone | Al. alloy | Mg. alloy | Al. oxide | Cast iron |
| Young's modulus E ($N/m^2$) | 4.80E+10 | 2.00E+10 | 7.00E+10 | 4.00E+10 | 3.80E+11 | 1.00E+11 |
| Poisson ratio ν | 0.20 | 0.25 | 0.30 | 0.35 | 0.23 | 0.25 |
| Friction coefficient | 0.350 | 0.350 | 0.000 | 0.000 | 0.000 | 0.000 |
| Restitution coefficient | 1.00 | 1.00 | 1.00 | 1.00 | different values | |
| Density ($kg/m^3$) | 2800 | 2500 | 2699 | 1800 | 4000 | 7000 |
| Radius (m) | 0.010 | 0.010 | 0.100 | 0.100 | 0.0025 | 0.0025 |
| Velocity (m/s) | ±10 | ±10 | 0.2 | 0.2 | 3.9 | 3.9 |
| **Input Parameters** | **Test 4** | | **Test 7** | | | |
| | Ex. 1 | Ex. 2 | Ex. 1 | Ex. 2 | | |
| | Al. oxide | Al. alloy | Al. alloy | Copper | | |
| Young's modulus E ($N/m^2$) | 3.80E+11 | 7.00E+10 | 7.00E+10 | 1.20E+11 | | |
| Poisson ratio ν | 0.23 | 0.33 | 0.33 | 0.35 | | |
| Friction coefficient | 0.092 | 0.092 | 0.400 | 0.400 | | |
| Restitution coefficient | 0.98 | 0.98 | 0.50 | 0.50 | | |
| Density ($kg/m^3$) | 4000 | 2700 | 2700 | 8900 | | |
| Radius (m) | 0.0025 | 0.0025 | 0.100 | 0.100 | | |
| Velocity (m/s) | 3.9 | 3.9 | 0.2 | 0.2 | | |

*Test 1: Elastic normal impact of two identical spheres*

**Published results:**

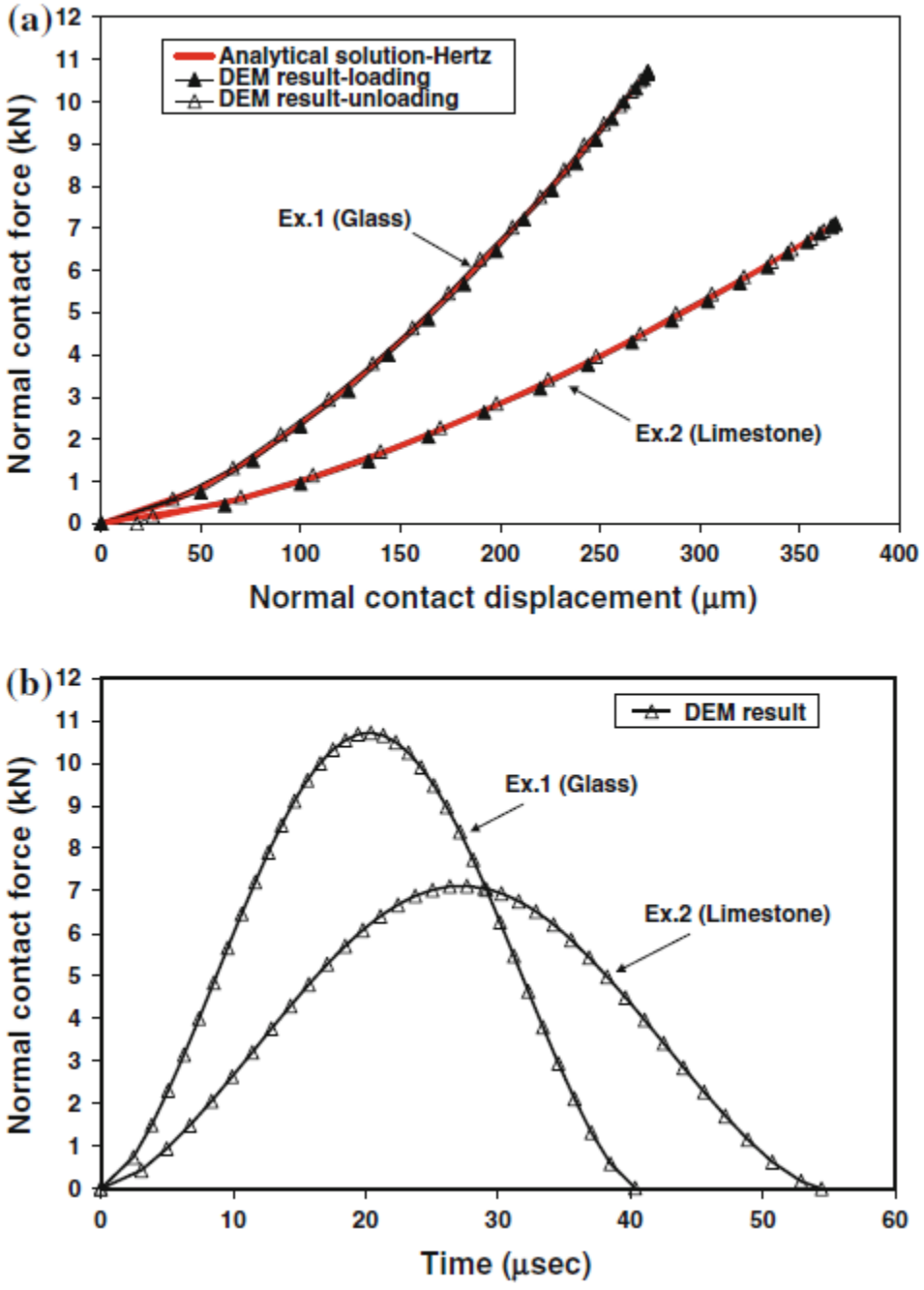


Figure 3-1: Test 1 published results for (a) force-displacement curve and (b) force-time curve (Chung & Ooi, 2011).

**DEM results:**

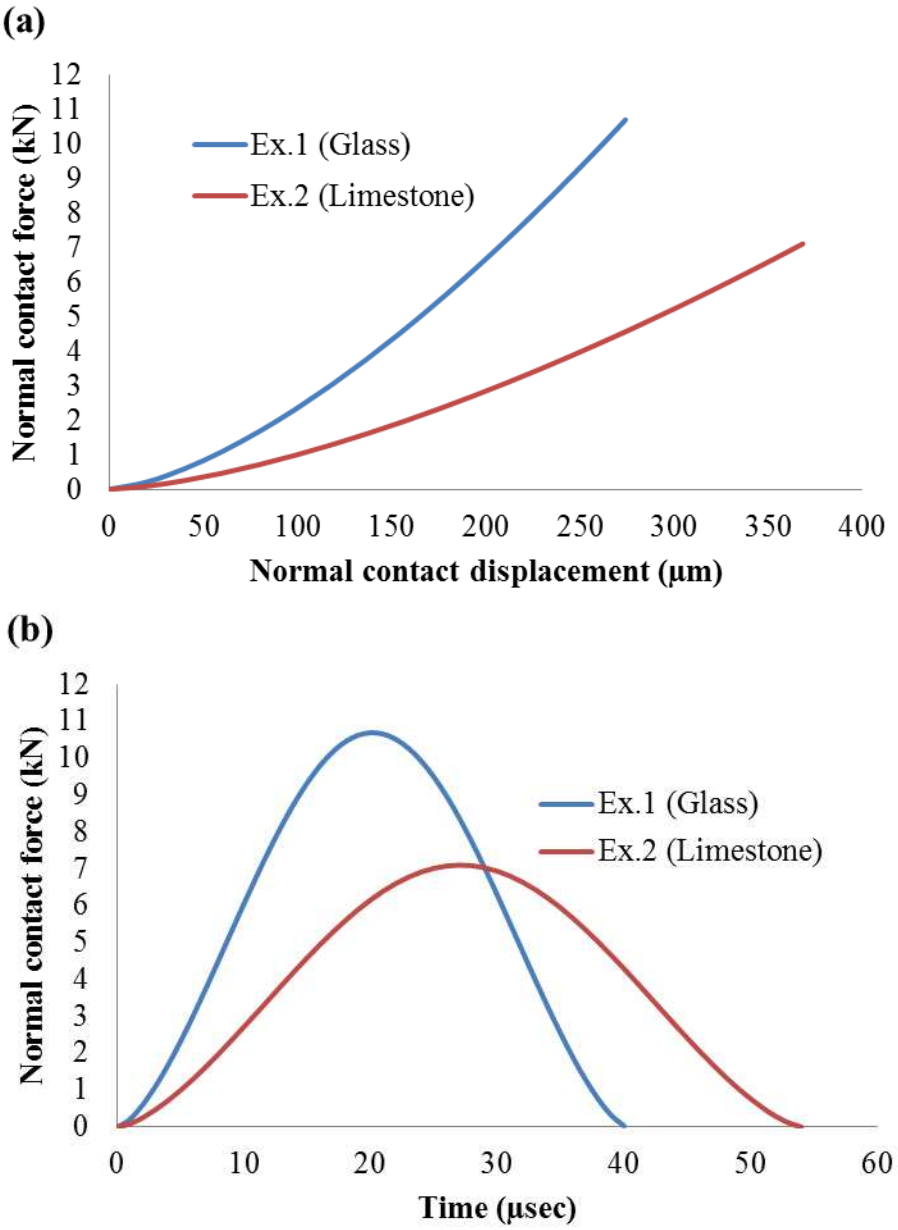


Figure 3-2: Test 1 DEM results for (a) force-displacement curve and (b) force-time curve.

Table 3-3: Comparison between DEM results and analytical solutions for Test 1

| | DEM Results | | Analytical Solution | | Percent Difference | |
|---|---|---|---|---|---|---|
| **Physical property** | Ex. 1 | Ex. 2 | Ex. 1 | Ex. 2 | Ex. 1 | Ex. 2 |
| Contact duration (µs) | 40 | 54 | 40 | 54 | 0.00% | 0.00% |
| Maximum displacement (µm) | 274 | 368 | 274 | 368 | 0.00% | 0.00% |
| Maximum force (N) | 10,701 | 7,110 | 10,697 | 7,108 | 0.04% | 0.03% |

Comparing Figures 3-1 and 3-2 shows that the DEM model matches the published results and analytical solutions for Test 1. The right columns in Table 3-3 show that the only parameter with any percent difference is the maximum force developed during the simulations and the percent differences between the analytical solutions and the DEM model are less than 0.05% for both examples.

*Test 2: Elastic normal impact of a sphere with a rigid plane*

**Published results:**

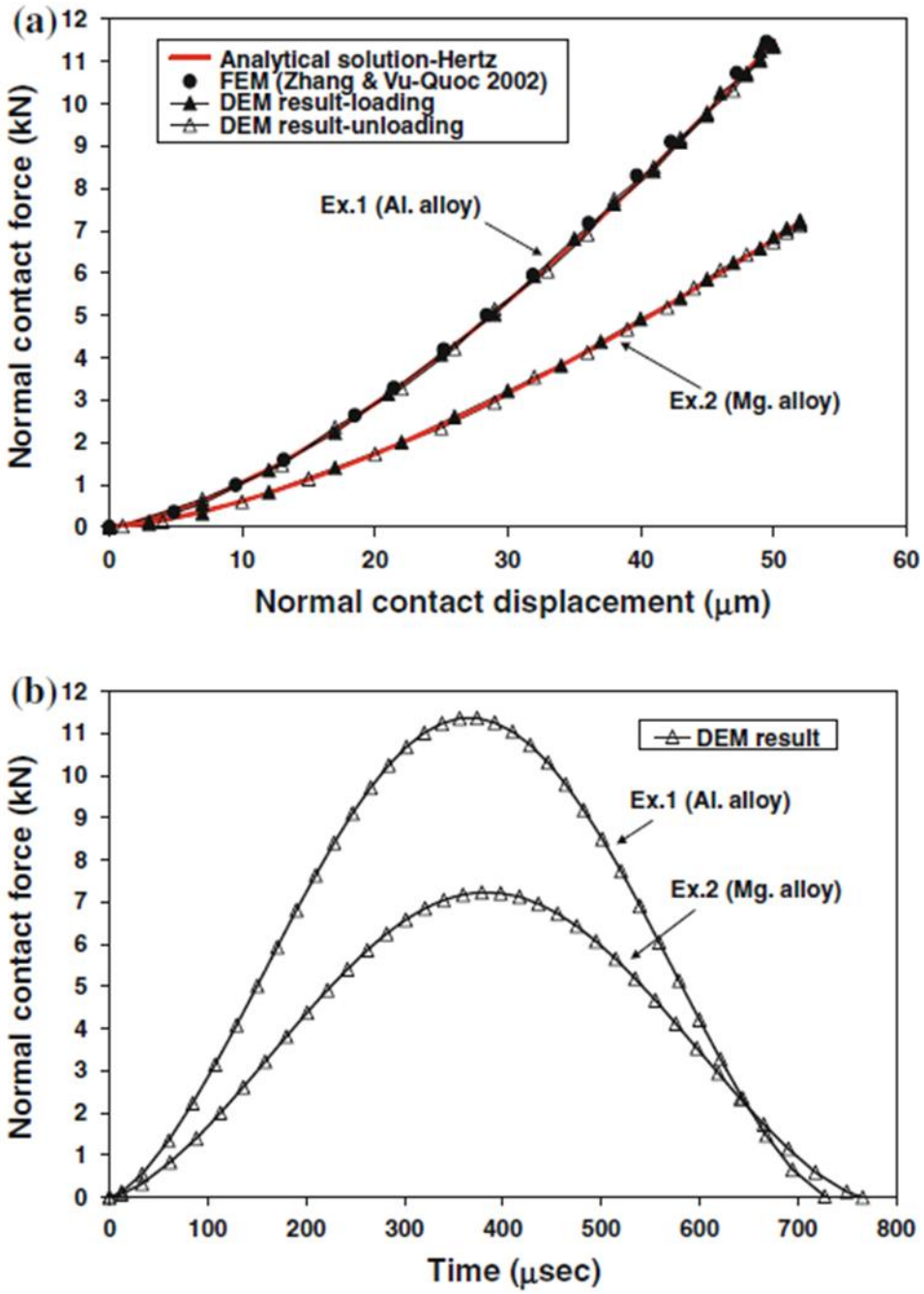


Figure 3-3: Test 2 published results for (a) force-displacement curve and (b) force-time curve (Chung & Ooi, 2011).

**DEM results:**

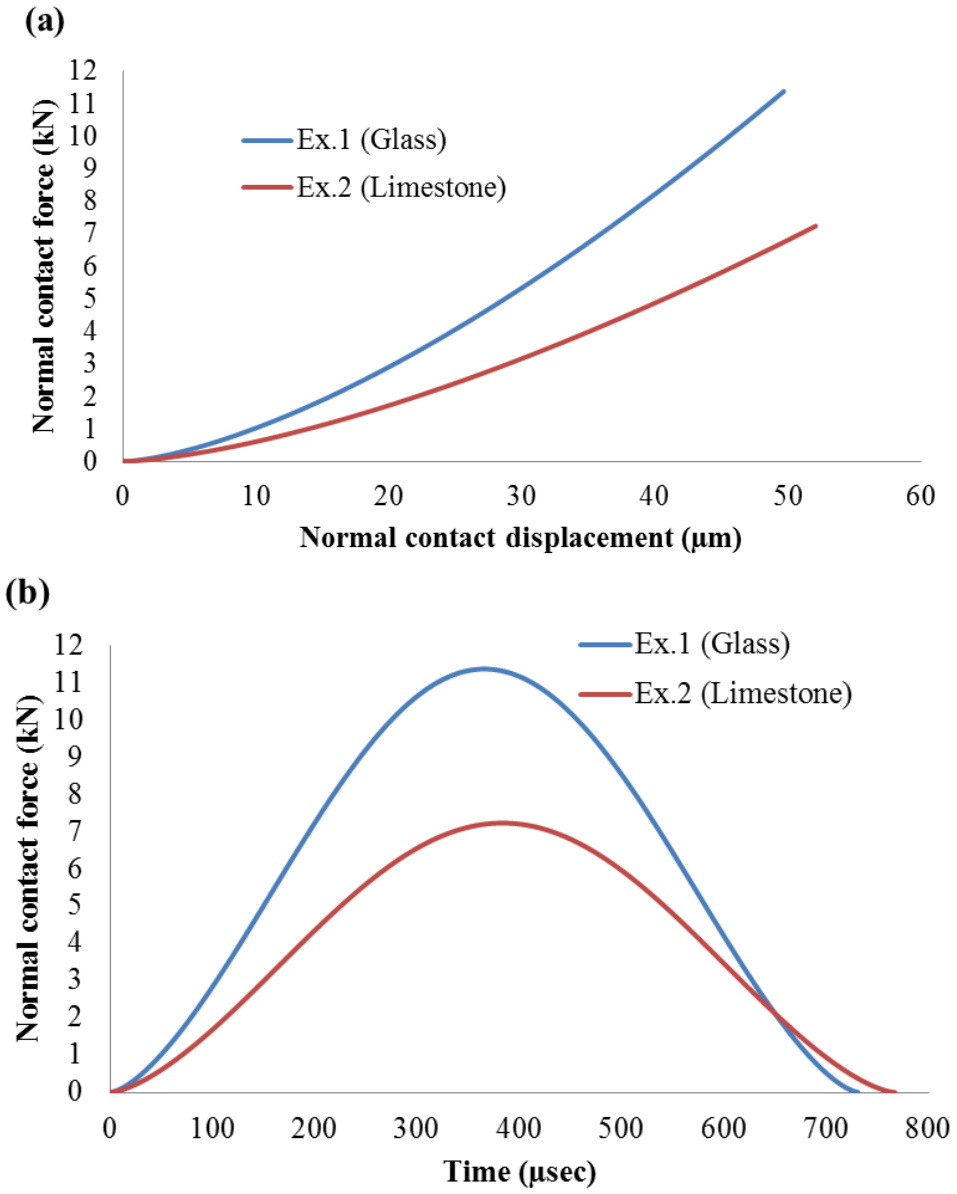


Figure 3-4: Test 2 DEM results for (a) force-displacement curve and (b) force-time curve.

Table 3-4: Comparison between DEM results and analytical solutions for Test 2

| | DEM Results | | Analytical Solution | | Percent Difference | |
|---|---|---|---|---|---|---|
| **Physical property** | Ex. 1 | Ex. 2 | Ex. 1 | Ex. 2 | Ex. 1 | Ex. 2 |
| Contact duration (μs) | 731 | 767 | 731 | 766 | 0.00% | 0.13% |
| Maximum displacement (μm) | 50 | 52 | 50 | 52 | 0.00% | 0.00% |
| Maximum force (N) | 11,370 | 7,233 | 11,370 | 7,233 | 0.00% | 0.00% |

Comparing Figures 3-3 and 3-4 shows that the DEM model matches the published results and analytical solutions for Test 2. The right columns in Table 3-4 show that the only parameter with any percent difference is the contact duration and the percent difference between the analytical solution and the DEM model is only 0.13% for one example.

*Test 3: Normal contact with different restitution coefficients*

**Published results:**

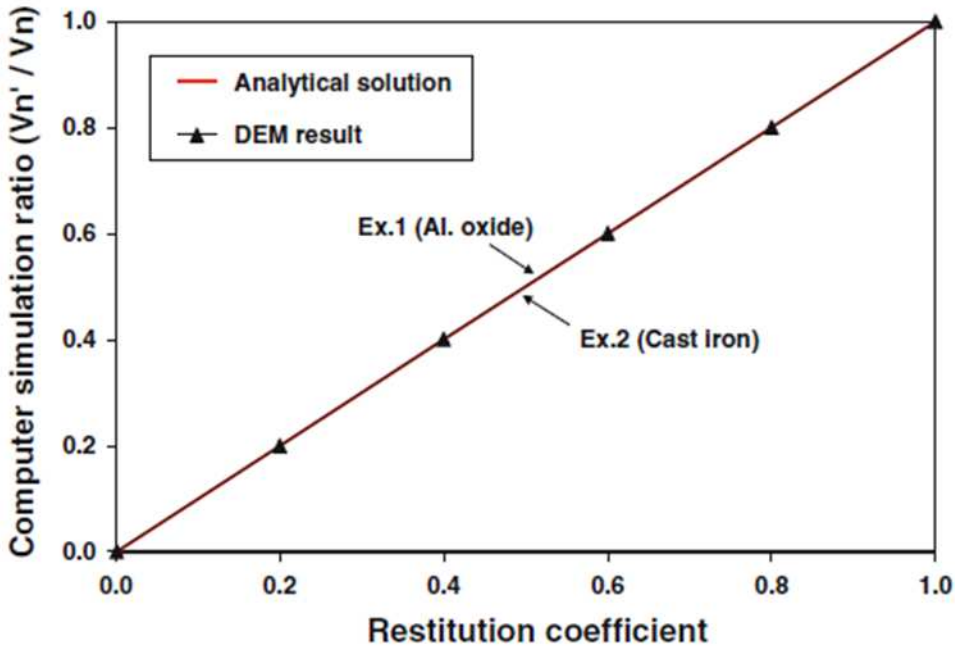


Figure 3-5: Test 3 published results for comparison between simulated velocity ratio and input value of the restitution coefficient (Chung & Ooi, 2011).

**DEM results:**

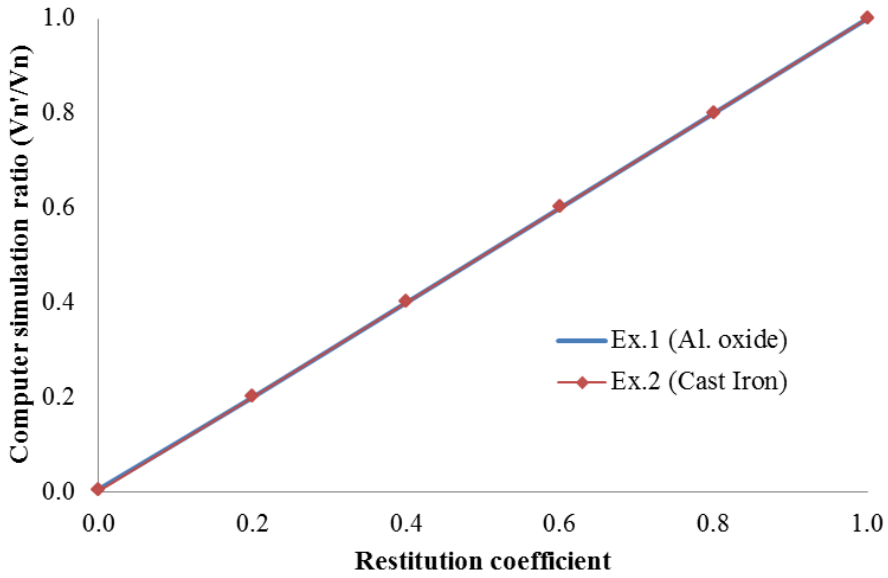


Figure 3-6: Test 3 DEM results for comparison between simulated velocity ratio and input value of the restitution coefficient.

Comparing Figures 3-5 and 3-6 shows that the DEM model matches the published results and analytical solution for Test 3.

*Test 4: Oblique impact of a sphere with a rigid plane with a constant resultant velocity but at different incident angles*

**Published results:**

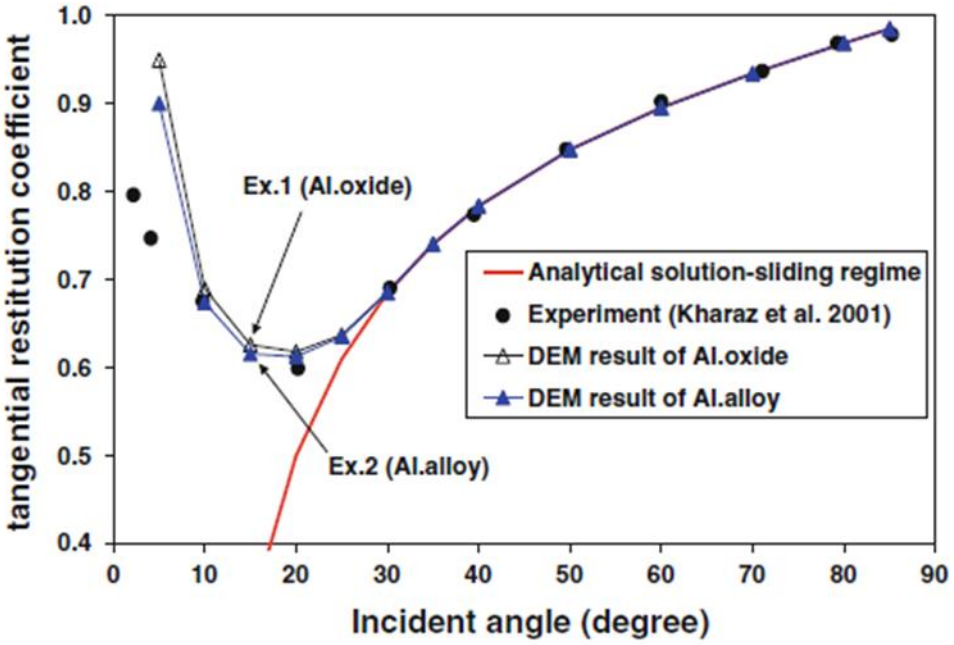


Figure 3-7: Test 4 published results for simulated, theoretical, and experimental tangential restitution coefficient $e_t$ for varying incident angles $\theta$ (Chung & Ooi, 2011).

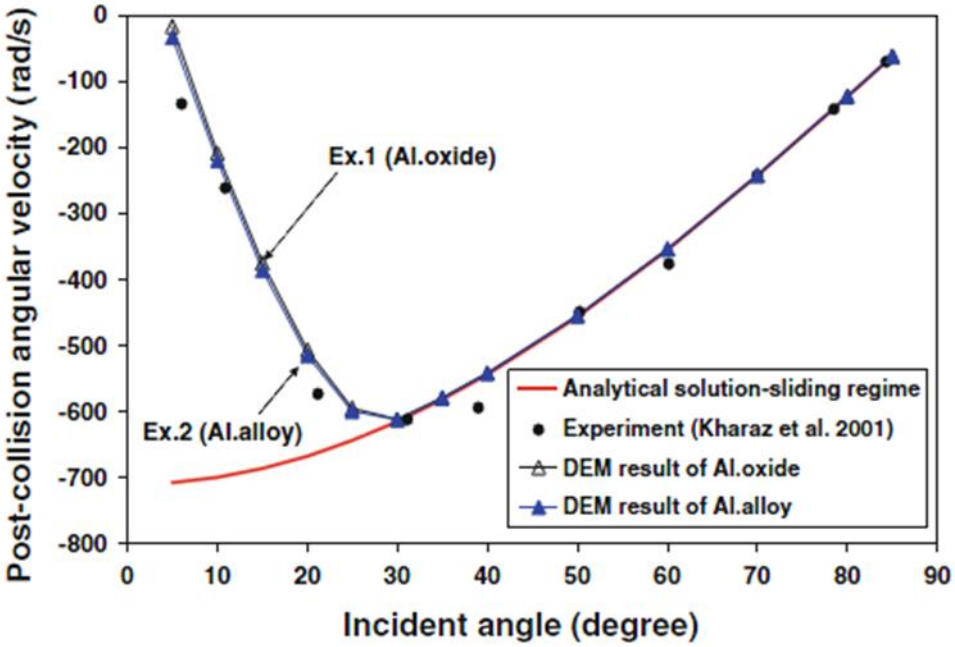


Figure 3-8: Test 4 published results for simulated, theoretical, and experimental post-collision

angular velocity $w_1$' for varying incident angles $\theta$ (Chung & Ooi, 2011).

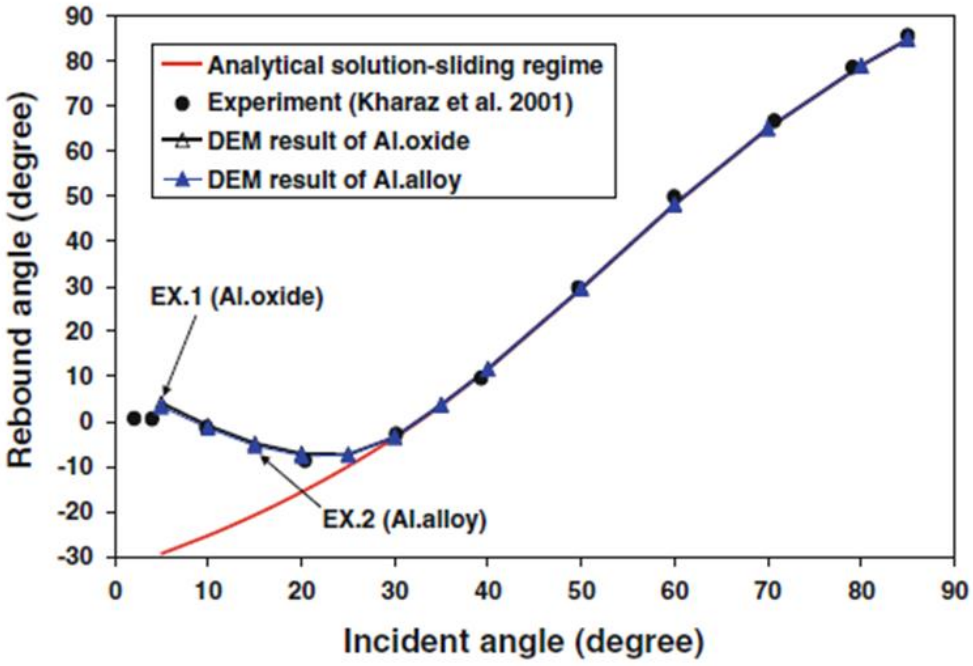


Figure 3-9: Test 4 published results for simulated, theoretical, and experimental rebound angles f for varying incident angles $\theta$ (Chung & Ooi, 2011).

**DEM results:**

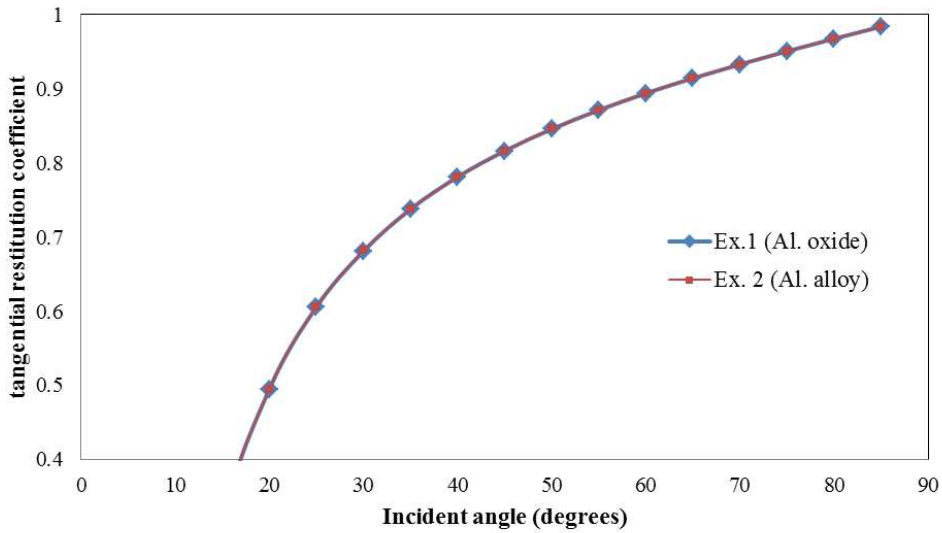


Figure 3-10: Test 4 DEM results for tangential restitution coefficient et for varying incident angles θ.

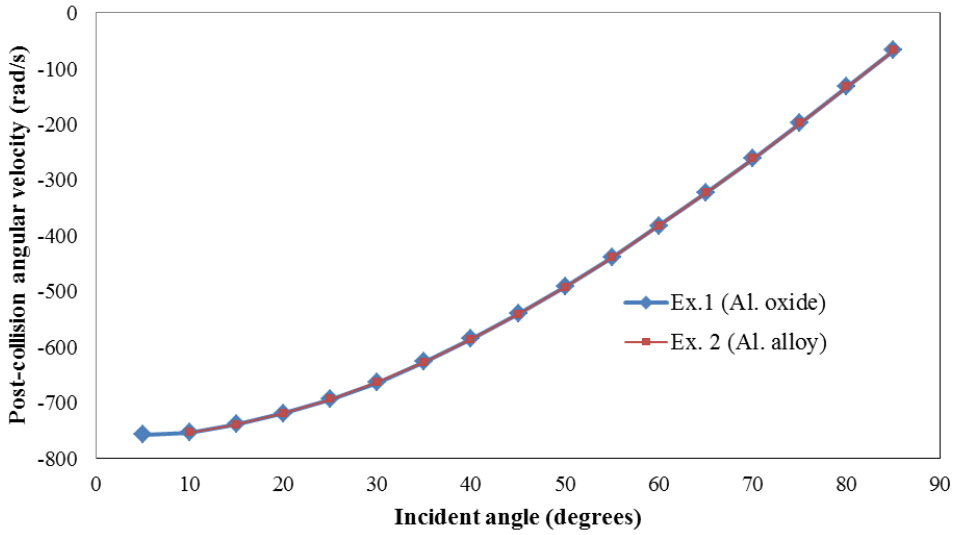


Figure 3-11: Test 4 DEM results for post-collision angular velocity w1' for varying incident angles θ.

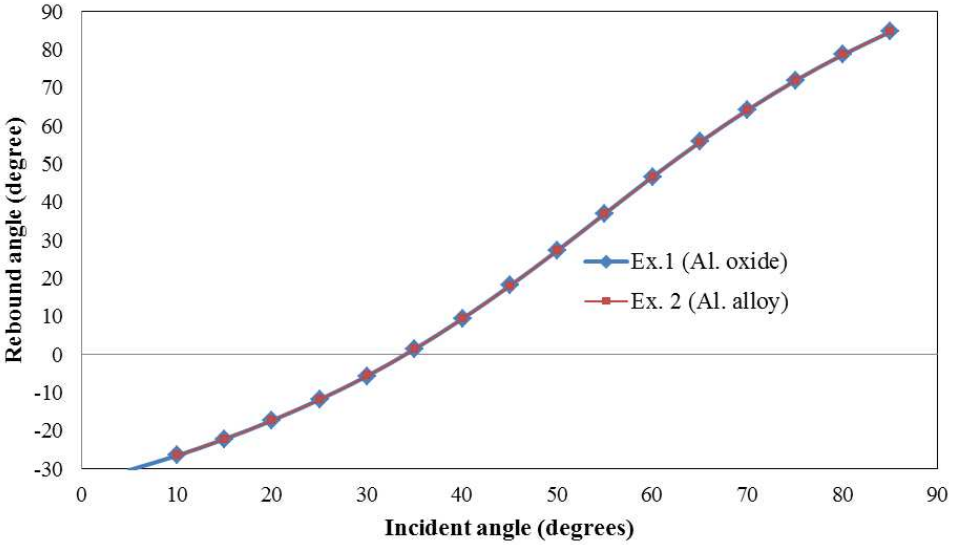


Figure 3-12: Test 4 DEM results for rebound angles f for varying incident angles θ.

Comparing Figures 3-7, 3-8, and 3-9 with Figures 3-10, 3-11, and 3-12, respectively, shows that the DEM model matches the analytical solutions for Test 4. The deviation of the published results from the analytical solution below about 28º incident angle is due to the inability of the analytical solution to predict behavior in the sticking regime. This discrepancy can be improved by using a more complete Hertz-Mindlin contact model (Chung & Ooi, 2011), whereas the DEM

model used for this research uses a Simplified Hertzian contact model (described by Equation 2-14). However, because the simulations performed for this research do not involve particle velocities anywhere near the velocity used for this benchmark test (3.9 m/s), one assumption made is that the deviation from the analytical solution below the critical impact angle would have negligible effects on the simulations and that the analytical solution has sufficient accuracy.

*Test 7: Impact of two identical spheres with a constant normal velocity and varying angular velocities*

**Published results:**

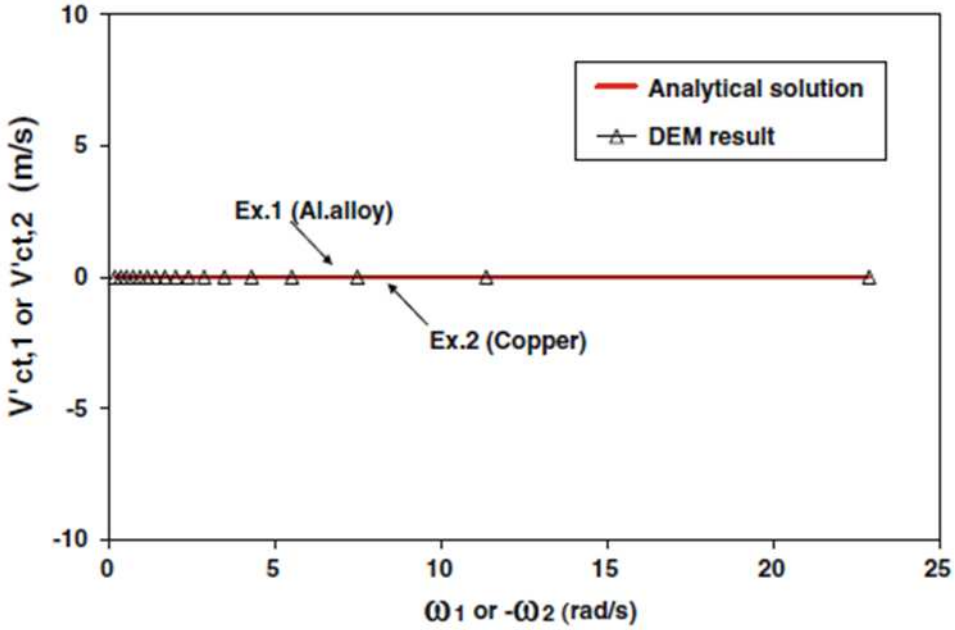


Figure 3-13: Test 7 published results for post-collision tangential velocity at the mass center for varying pre-collision angular velocities (Chung & Ooi, 2011).

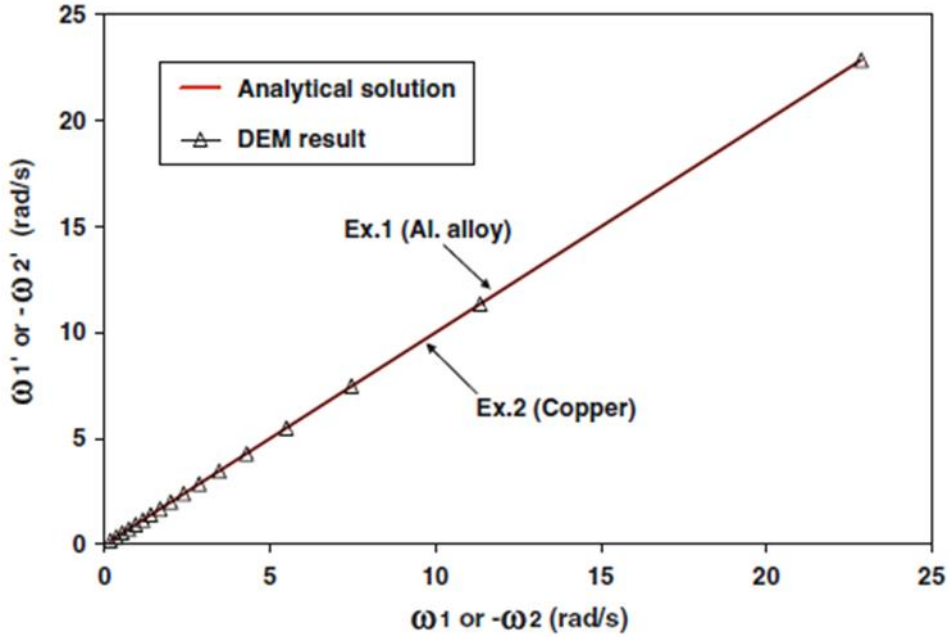


Figure 3-14: Test 7 published results for post-collision angular velocity for varying pre-collision angular velocities (Chung & Ooi, 2011).

**DEM results:**

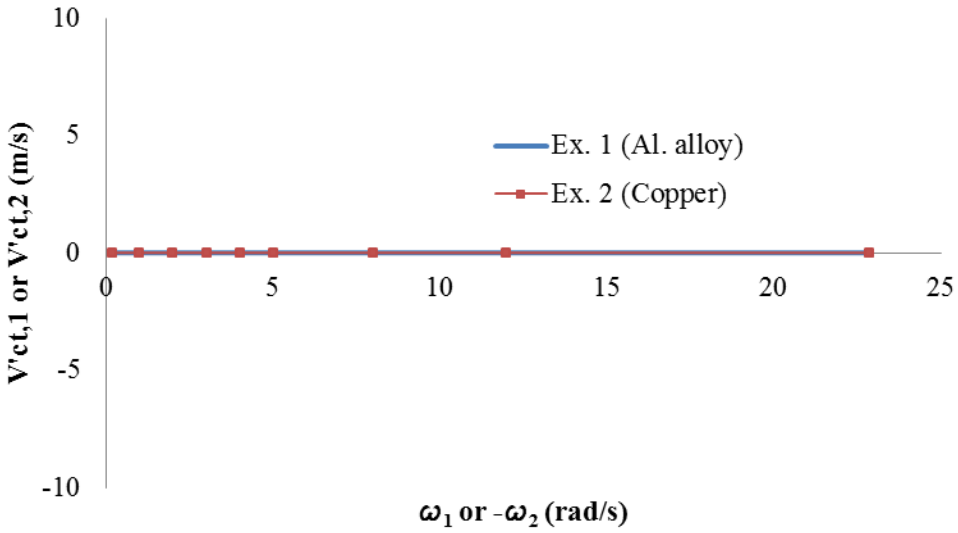


Figure 3-15: Test 7 DEM results for post-collision tangential velocity at the mass center for varying pre-collision angular velocities.

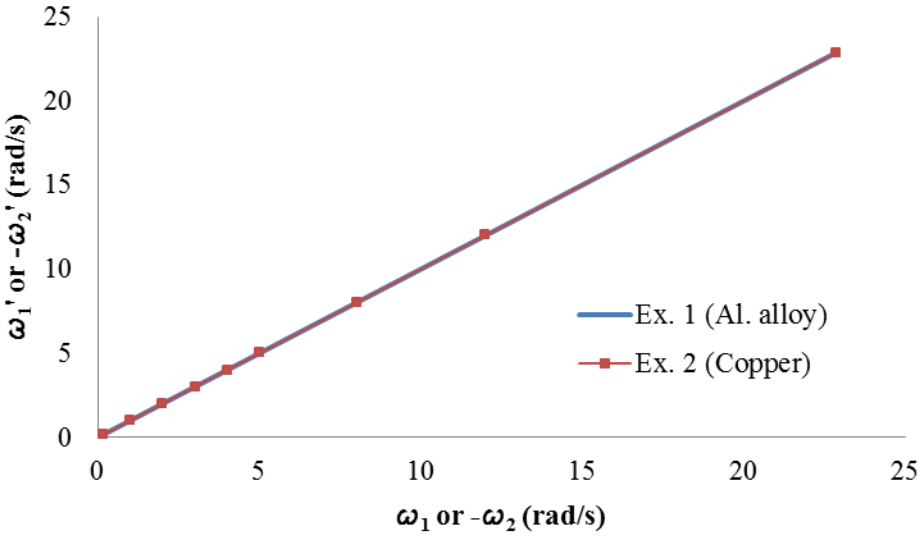


Figure 3-16: Test 7 DEM results for post-collision angular velocity for varying pre-collision angular velocities.

Comparing Figures 3-13 and 3-14 with Figures 3-15 and 3-16, respectively, shows that the DEM model matches the published results and analytical solutions for Test 7.

# Chapter 4 : NUMERICAL AND EXPERIMENTAL EVALUATION OF THE ERODIBILITY OF SURFACE TREATED PARTICLE PACKINGS[1]


## Summary

The erodibility of homogeneous two-dimensional spherical particle packings subjected to added mass surface treatments was explored using a combination of physical flume experiments and the discrete element method (DEM). Packings composed of spherical glass particles, with and without surface treatments and angled at two different slopes, were tested experimentally and simulated numerically under surficial flow conditions. The surface treatments acted to add mass to the surface of the particle packings. Particle erosion was quantified by tracking eroded particles as a function of fluid velocity. DEM simulations and flume experiments were first performed with a layer of steel particles that served as an extreme case of surface treatment. Similar trends were observed between the simulations and experiments, whereby the number of eroded particles decreased by an average of 90% when compared to untreated cases. The results from this surface treatment suggested that if the surface treatment mass is large enough, nearly all particle erosion under surficial flow conditions can be mitigated. Additional experiments were performed with surface treatments composed of increasing application rates of wetted agricultural straw. The particle erosion rates were dominated by piecewise linear behavior as a function of eroded mass versus fluid velocity. This behavior indicated a) an initial resistance to flow based on gravity, followed by b) a surface treatment movement that induced widespread failure or erosion at a much higher rate. Dislodgement and subsequent erosion of particles occurred at higher fluid velocities (over 50% higher for the highest straw application rate) when the surface treated cases were


[1] Peterson, K.L., Bareither, C.A., and Heyliger, P.R. (to be submitted) *Journal of Engineering Mechanics, ASCE*

compared to the untreated cases. Conclusions drawn from the simulation and experiment results indicated a direct correlation between added mass on the surface of a particle packing and decreased erosion under surficial flow conditions and showed that as slope increased, erosion levels increased and began at lower surficial flow fluid velocities.

## Introduction and Background

Soil erosion is the process of soil particles being physically transported by factors such as water, wind, ice, or earthen mass (Julien, 2010). Erosion can be mitigated with several different methods. For soil, vegetation is the most effective long-term means of erosion control (Demars et al., 2004). However, adequate vegetation is frequently not an option. During these cases, other erosion mitigation techniques are necessary. These include erosion barriers, mulching, or a combination of these options (Robichaud et al., 2010; Napper, 2006). In general terms of erosion control, materials are applied as surface treatments to base soils with the goal of mitigating particle movement and decreasing erosion.

Examples of cases when erosion control measures are necessary include burn sites after a wildfire or along rural access roads. In both cases, the soil is bare and un-reinforced. Precipitation events then lead to increased erosion (Stewart et al., 2003). Case studies on physical field observations have shown correlations between the application of surface treatments and the decrease of annual sediment yields. Robichaud et al. (2010) report that the most common post-fire soil stabilization technique currently used in practice is mulching. Straw mulch application rates in the rate of 3-4 Mg/ha were used on Colorado sites after the High Park Fire (Schmeer et al., 2018) and concentrations up to 5.6 Mg/ha were used after the Missionary Ridge Fire (deWolfe et al., 2008). After the 2000 Cerro Grande Fire in New Mexico, the application of straw mulch with

seed reduced mean annual sediment yields by 70% in the first post-fire year and 95% in the second post-fire year (Dean, 2001). Following the 2002 Hayman Fire near Colorado Springs, a 94% reduction in sediment yield was measured in post-fire year one and 90% in post-fire year two with straw mulch surface treatment swale compared to the untreated control swale (Robichaud et al., 2010). On access roads in the Appalachian Mountains, surface layers of gravel were demonstrated to reduce soil erosion on the roadbed and adjacent cut and fill slopes by 88% (Swift, 1984). Most case studies performed on surface treatments mitigating erosion are conducted on large areas of land and over a period of time of at least two years. All show similar trends. The mechanisms involved in how surface treatments work to reduce erosion have been hypothesized and most published assumptions indicate that treatments reduce raindrop impact, increase soil infiltration capacity and moisture content, and aid in seed retention on slopes to stimulate vegetative growth (Bautista et al., 1996; Bautista et al., 2009).

Laboratory experiments have been performed to evaluate effects of surface treatments on soil erosion. Jennings & Jarrett (1985) performed rain experiments on slopes with various mulch materials (straw, bark, burlap, rocks, and others) and tracked, among other outputs, the effect of the surface treatments on total erosion over a specified period of time. Montenegro et al. (2013) investigated runoff and sediment transport on slopes with and without straw mulch surface treatments. Moden (2018) performed rain experiments on burned soil samples with a range of straw mulch applications and evaluated effects of the surface treatments on soil erosion and runoff. Also, although not specific to analyzing effects of surface treatments, other laboratory experiments on erosion include analyzing slope shape effects (Rieke-Zapp & Nearing, 2005), evaluating rough and smooth surfaces (Gomez & Nearing, 2005), and scaling effects (Sadeghi et al., 2015).

However, the literature is limited in research pertaining to the optimal amount of surface

treatment, the exact role of surface objects on the motion of underlying particles and coupling the use of small-scale laboratory experiments with numerical simulations at a particle level to evaluate the effects of surface treatments to stabilize slopes and reduce erosion during surficial flow conditions. Discrete element modeling provides one means of such numerical simulations at the particle level. This is a convenient technique used to represent granular matter as an idealized assembly of particles with overall macroscopic behavior resulting from the collection of all particle interactions (O'Sullivan, 2011). One advantage of DEM modeling is that particle-scale information can be tracked and recorded throughout the simulations, such as individual particle orientations and rotations. This can be a relatively difficult task (if not impossible) to evaluate during laboratory tests. Laboratory testing has the advantage of capturing physical material response whereas DEM simulation results are subject to validation and calibration of the model. Research completed with both numerical simulations and physical experiments can benefit from the advantages of both. The study considered here employs this strategy.

Using the DEM, several field scale boundary value problems of soil and rock slopes have been modeled (Lu et al., 2014; Stead et al., 2006; Zhang et al., 2005; Taboada & Estrada, 2009). The DEM has also been used to simulate soil laboratory experiments including, for example, biaxial compression tests (Iwashita & Oda, 1998; Potyondy & Cundall, 2004), triaxial tests (Thornton, 2000; Cui et al., 2007; Ng, 2004), plane strain tests (Ng, 2004; Powrie et al., 2005), direct shear tests (Masson & Martinez, 2001; Cui & O'Sullivan, 2006), simple shear tests (Matsushima et al., 2003), interface shear tests (Wang et al., 2007), and penetration tests (Huang & Ma, 1994; Butlanska et al., 2009). In general, coupled experimental and numerical research have involved comparisons between DEM simulations and laboratory-scale experiments as opposed to field-scale experiments (O'Sullivan, 2011).

The research presented herein evaluates the hypothesis that compressive stress from added mass on the surface is a major contributor to the effectiveness of surface treatments in decreasing erosion. Gravitational forces from the added mass that surface treatments provide may hold surface particles in place while the cover material provides a physical barrier that adds frictional forces acting to reduce surface particle rolling and sliding. The possibility of these additional forces acting on the surface of a slope has not been investigated at the particle level either in the lab or in simulations. The hypothesis was tested by investigating particle erosion of particle packings subjected to surficial flow conditions with and without surface treatments via physical experiments using a flume and numerical simulations using the DEM. Investigating surface treatments applied to bare particle packings to mitigate erosion is applicable to any bare slope where some type of surface cover is applied to limit particle movement.

**Methods and Materials**

The behavior of homogeneous two-dimensional spherical particle packings at two different slopes subjected to surficial flow conditions were investigated with different types and amounts of surface treatments. An experimental apparatus was designed to assess particle erosion within a control volume, and tests were performed to compare physical experiments with DEM simulations of spheres confined to move in a single plane subjected to surficial flow. Preliminary dry experiments and simulations on particle erosion under gravity loading were performed and the results were used to refine the values used for the friction coefficient between particles, friction coefficient between the particles and the Plexiglass walls, mass damping coefficient, and particle-particle contact damping coefficient. The final values for these parameters resulted in particle movement beginning in the simulations at the same angle as the physical experiments and

matching bounce and timing characteristics. Next, experiments and simulations were performed with and without surface treatments. Glass spheres (marbles) were used as the particles and two materials, steel ball bearings and agricultural straw, were used as surface treatments.

The glass spheres had a density of 2500 kg/m3, a Poisson ratio of 0.22, and an elastic modulus of 70 GPa (Saint-Gobain, 2018). The glass spheres were not perfectly uniform in size, due to ball imperfections from manufacturing (MagLite, 2018), and caliper measurements on twenty spheres yielded diameters ranging between 13.28 mm and 14.06 mm. The steel ball bearings had a density of 7833 kg/m3, Poisson's ratio of 0.285, and Young's modulus of 200 GPa (BC Precision, 2018) and had precise diameters of 12.7 mm. The steel ball bearings were chosen as a surface treatment type for four reasons: 1) they were roughly the same size as the glass particles, and therefore fit in the experimental setup; 2) they were spherical and simulated similarly to the glass particles in the DEM model; 3) steel density is over three times that of the glass particles and easily simulated surface pressure; and 4) they were distinguishable from the glass particles and could be tracked during the experiments.

Agricultural straw was used in this study as the second surface treatment as this material is common, cost-effective, and readily available. Straw mulch application rates of 1.12, 2.24, 5.60, and 11.21 Mg/ha (dry mass basis) were used. The range of 1.12-11.21 Mg/ha is inclusive of actual application rates (Schmeer et al., 2018; deWolfe et al., 2008) while also allowing for a larger spread of data. In the straw surface treatment experiments, the target mass of dry straw mulch was weighed and then soaked in water prior to application as a surface treatment. Soaking the straw mulch simulated initial wetting that would be anticipated during a precipitation event, prior to development of surficial flow.

There is a significant issue of scaling in this study regarding application of conventional

straw to the glass particles, which were orders of magnitude larger than soil particles encountered in actual slopes (e.g., sand and silt). However, the physical process of applying surface treatment to particles is analogous and the use of the larger particles allowed visual particle tracking that would be impossible with smaller soil particles. The advantage of conducting experiments on a progression of increased agricultural straw application rates was that the hypothesis of added compressive mass to mitigate erosion could be tested without changing materials while still tracking individual particle behavior.

The flow rate was recorded during the physical flume experiments, whereas the input parameter for the hydraulic force calculations in the DEM model was fluid velocity. Videos were taken of the flume experiments and flow rates were converted to fluid velocities using the height of water above the surface of the particles throughout the experiments. Data was collected on eroded particles versus fluid velocity and the data points were averaged for all experiments of the same surface treatment type.

**Flume Experiments**

Experiments were performed on a planar packing of spheres in a planar flume. The experimental setup is shown in Figure 4-1 with a homogeneous packing of the glass spheres. The control domain was approximately 60 cm long (in the direction of fluid flow), 14 cm tall, and 1.6 cm thick (one unit into the plane) and was bounded by Plexiglass sheets. The geometry was chosen such that DEM simulations could be directly compared with the flume experiments, DEM simulations could be completed in reasonable runtimes, and a sufficiently large surface area captured the influence of the surface treatments.

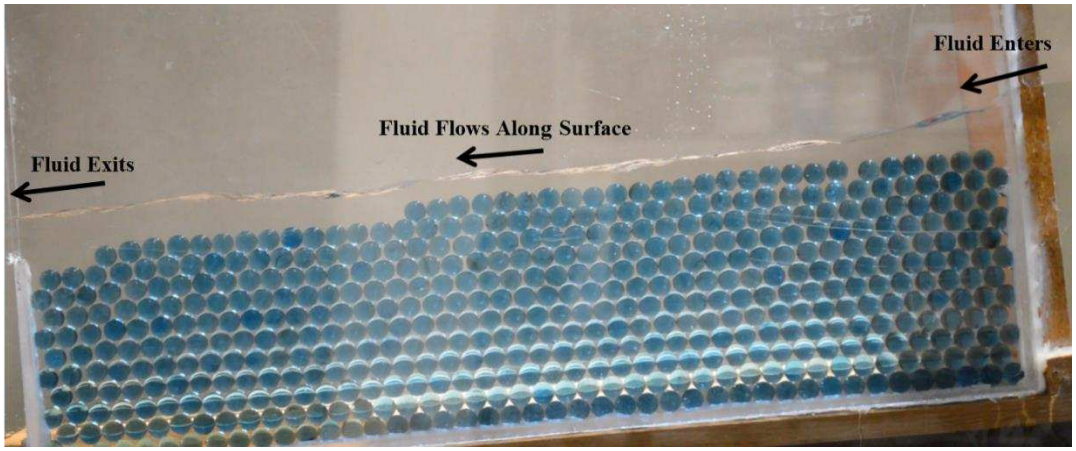

Figure 4-1: A packing of uniform glass spheres during the erosion process positioned inside the flume. Arrows signify the direction of fluid flow.

Slopes of 6º and 11º were tested and example initial configurations on the 6° slope of the four straw treatment application rates are shown in Figure 4-2. The straw was aligned along the length of the flume before being dropped down on top of the glass particles. This was done to alleviate artificial boundary effects that could arise from the straw being compressed by the Plexiglass boundaries if the straw was not aligned. Multiple experiments were performed for each quantity of straw until trends were observed and the data were repeatable.

a) 1.12 Mg/ha

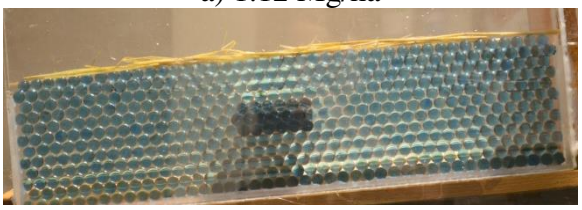

b) 2.24 Mg/ha

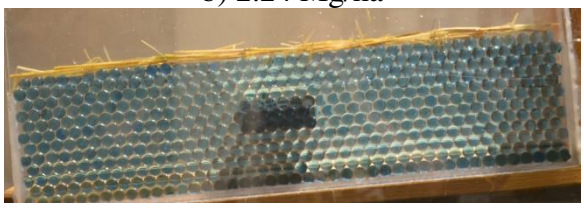

c) 5.60 Mg/ha

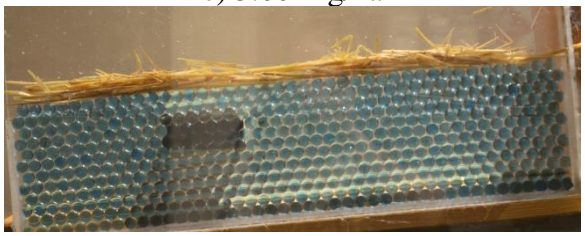

d) 11.21 Mg/ha

Figure 4-2: Initial configurations of the agricultural straw surface treatments on the 6º slope experiments for four application rates.

Flow rates were varied in the experiments using a motor-controlled flume pump. The

smallest increment on the motor resulted in an average fluid velocity increase of 0.05 m/s. As flow initiated within the particle domain, voids between the particles filled as the water surface approached the upper surface of the particles. Subsequently, surface flow initiated and surface treatments and glass particles could be dislodged and eroded downstream. Particles that exited the domain during the experiments were collected as water continued to flow through the particle domain. The number of particles eroded was counted as a function of time for a given experiment. The experimental setup allowed physical observations of individual particle movement under the primary fluid forces that drive erosion.

## The DEM Model

Specific details on the theory used for DEM analyses were originally presented by Cundall and Strack and can be found elsewhere (O'Sullivan, 2011; Cundall & Strack, 1979). The DEM model developed for the research presented here was verified using Tests 1, 2, 3, 4, and 7 from the set of benchmark tests proposed by Chung and Ooi (2011). Details on the contact models, damping, and hydraulic loading will be discussed.

### *Normal Contact Model*

The contact model for normal contact forces between two particles was the simplified Hertzian contact model. The contact stiffness is a function of the radii, shear moduli, Poisson's ratios, and overlap distance of the two particles in contact. The equations amount to an effort to replicate the actual deformation between two elastic spheres with a relatively simple one-dimensional relationship rather than using the full equations of three-dimensional elasticity. The normal contact force between the particles is then calculated by multiplying the stiffness by the

sphere overlap distance. The simplified Hertzian contact model is effective for use in DEM simulations because the model provides a logical basis for the link between spring stiffness and actual material properties. Also, in general, the model provides efficient and accurate calculations for non-cohesive granular materials such as the glass marbles modeled here (Bossy & Safuryn, 2016).

*Tangential Contact Model*

The DEM model used a simplified Mindlin-Deresiewicz tangential contact model (Mindlin & Deresiewicz, 1953; Vu-Quoc et al., 2000) for the tangential forces between two particles, where tangential stiffness is a function of the current normal stiffness and the Poisson ratios of the particles in contact. Tangential contact forces differ from normal contact forces, because the stiffness is not simply multiplied by the sphere overlap distance, but rather by the summed incremental tangential displacements (relative velocities multiplied by the time increment) occurring throughout the contact. The relative velocity between the particles for each time step is a function of the translational velocities, rotational velocities, and centroidal locations of each particle and are calculated using the permutation tensor multiplied by the time increment and summed throughout the contact. The tangential forces are then added to the normal forces and also cause moments about the centers of the particles. Finally, the tangential forces are limited by a Coulomb friction criteria based off a defined friction coefficient between the particles.

*Damping*

One limitation to the simplified Hertzian contact model is that the energy dissipation that occurs physically is not captured (O'Sullivan, 2011). Particle-particle contact damping is applied,

with a specified coefficient, to alleviate issues with non-physical particle vibrations. Mass damping (also called global damping), originally proposed by Cundall and Strack (1979), is also applied with a specified coefficient. Mass damping is applied to the resultant velocities of each particle. The details for both particle-particle contact damping and mass damping can be found elsewhere (O'Sullivan, 2011).

*Hydraulic Loading*

In the DEM simulations, the fluid flowing along the surface of the experiments was simulated by subjecting the surface particles to drag forces. The drag force is given with the following equation for drag force on a sphere, accounting for properties of the fluid (Julien, 2010):

$$F_D = \frac{1}{2}\rho V^2 C_d A_i \qquad \text{[Equation 4-1]}$$

where $\rho$ is the density of the fluid (1,000 kg/m$^3$ for water), $V$ is the velocity of the fluid flow, $C_d$ is a shape factor (0.5 for spheres), and $A_i$ is the projected surface area of particle $i$ perpendicular to the flow ($A_i = \pi R^2$ for spheres with radius $R$). To avoid instabilities, flow velocities were increased linearly during the simulations until reaching a maximum value. Drag forces were applied horizontally on the surfaces of the particles. These forces created a moment acting at the center of each of the surface particles about the axis into the plane.

For all simulations, the drag forces were initially applied to the top row of particles exposed to the fluid flow. As the particles eroded, the drag forces were applied to newly exposed surface particles. In the case of steel particles used as surface treatment, drag forces were applied to the surface treatment particles along with the top row of glass particles. Only the fluid velocity and surface treatment were varied in this study, although in reality the physical surface treatment could also act to decrease drag forces on the upper-most glass particles. The precise nature of how surface

treatment objects affect drag forces on the particles beneath them is at present unknown. However, assuming that the upper-most layer of glass particles was subjected to the same drag force magnitudes with and without a surface treatment was a worst-case scenario and allowed for direct comparisons between surface treatments without having to take into account varying drag force.

Initial simulations were performed with an 11° slope and untreated glass particles (control) revealed that particle movement initiated at a fluid velocity of 0.66 m/s. During the flume experiments, the fluid velocity was increased every 15 s (approximately + 0.05 m/s each increment). This time interval was chosen since 15 s was necessary to allow the flume pump to increase the flow rate to measurable levels. In the DEM simulations, fluid velocity was changed instantaneously. Fluid velocity in the DEM simulations was initially linearly increased by 0.01 m/s per hundredth of a second, from 0 m/s to 0.66 m/s, and then held constant until 1 s. Fluid velocity was then increased by 0.01 m/s every 0.25 s until a velocity of 0.9 m/s was achieved and maintained for 0.25 s. This computation sequence resulted in a total simulation time of 7 seconds, which was generally long enough to simulate the evolution of large-scale erosion.

**Simulation Details**

DEM simulations were performed on the untreated glass particles and the steel particles used as surface treatment. Side by side comparisons between initial configurations of the simulations and experiments are shown in Figure 4-3 for the 6° slope. The DEM simulations only modeled 6 rows of glass particles, as opposed to 12 rows in the flume experiments. This difference between the DEM simulations and physical experiments did not affect the results and allowed for faster computation times.

a) Untreated Geometry: Glass Particles Only

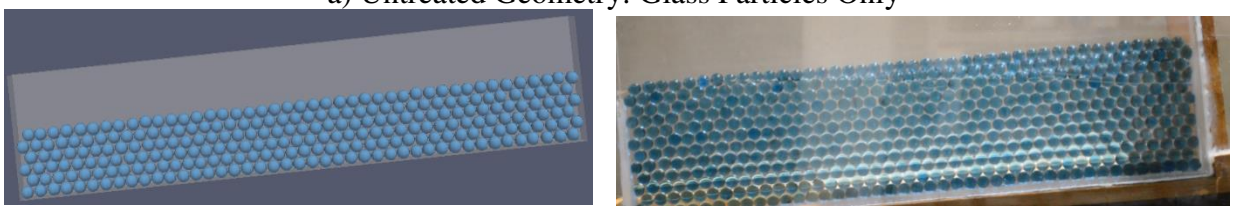

b) Surface Treatment 1: Layer of Steel Particles

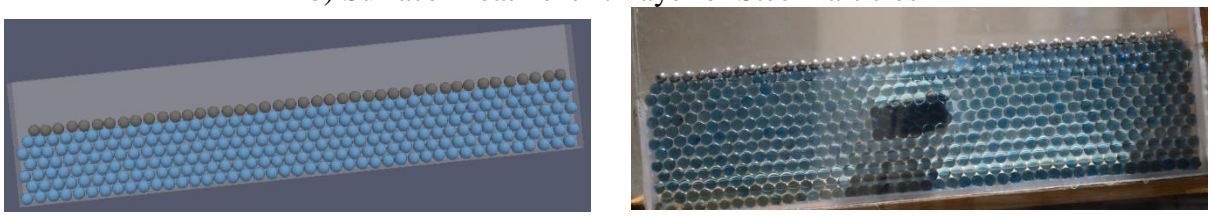

Figure 4-3: Initial configurations of 6º slope simulations (left) and experiments (right).

A particle size distribution was assigned to the simulated glass particles corresponding to an assumed uniform distribution between the measured minimum and maximum diameters. For the untreated glass particle simulations, particle locations were extracted at 6º and 11º slopes from the dry tilt packings and were then simulated under gravity loading to ensure the initial geometries were in states of equilibrium. The particles used for the layer of steel particle surface treatment were given initial locations above the non-tilted (0º), untreated glass particle equilibrated state. The particles settled under gravitational loading.

For all simulations, the out-of-plane boundary conditions consisted of the Plexiglass walls and were simulated by specifying rigid wall boundary conditions at the appropriate locations. In the DEM model, the normal and tangential contact forces between particles and rigid walls were calculated with the same contact models previously defined.

Constants used for the simulations are listed in Table 4-1. The limiting time increment for DEM simulations with spheres and a Hertzian contact model is a function of the minimum radius of all particles in the simulation and the material properties of that particle (Sheng et al., 2004). The time step increment used for the simulations was below the critical time increment required.

The friction and damping coefficients determined from preliminary dry experiments and simulations are in line with expected values.

Table 4-1: Input Parameters for DEM Simulations

| Material | Parameter (units) | Value | Source |
|---|---|---|---|
| All Simulations | Acceleration due to gravity ($m/s^2$) | 9.81 | - |
| | Time step increment (second) | $1.0 \times 10^{-6}$ | - |
| | Particle-particle friction coefficient | 0.6 | Values determined from preliminary dry experiments and simulations under gravitational loading |
| | Particle-rigid wall friction coefficient | 0.6 | |
| | Mass damping coefficient | 10 | |
| | Particle-particle contact damping coefficient | 0.15 | |
| Glass Marbles | Number of Particles | 258 | - |
| | Density ($kg/m^3$) | 2500 | (Saint-Gobain, 2018) |
| | Poisson's Ratio | 0.22 | (Saint-Gobain, 2018) |
| | Young's modulus (GPa) | 70 | (Saint-Gobain, 2018) |
| | Diameter (mm) | 13.28 - 14.06 | caliper measurements |
| Steel Ball Bearings | Number of Particles | 42 | - |
| | Density ($kg/m^3$) | 7833 | (BC Precision, 2018) |
| | Poisson's Ratio | 0.285 | (BC Precision, 2018) |
| | Young's modulus (GPa) | 200 | (BC Precision, 2018) |
| | Diameter (mm) | 12.7 | caliper measurements |

**Assumptions and Simplifications**

Several simplifications were made in the DEM model regarding the calculation and application of hydraulic forces. In the simulations, the fluid was not modeled but rather the hydraulic forces generated by the fluid on the particles. Because of the nature of the fluid flow at the exit during the experiments, the left-most surface particle was subjected to larger forces than the other surface particles. This phenomenon was not captured in the drag forces calculated in in the DEM simulations.

The flume used for the simulations had a maximum flow rate of 0.028 $m^3/s$. This maximum flow rate corresponded to maximum fluid velocity of about 65 m/s in the physical experiments. Considering that the experiments were performed at low flow rates that corresponded to fluid

velocities ranging between 0.4 – 1.0 m/s, there may be slight differences between measured flow rate and the estimated fluid velocity in the physical experiments. In addition, the smallest flow rate increment in the flume corresponded to an increase in fluid velocity of approximately 0.05 m/s, whereas the fluid velocity in the DEM simulations could be precisely controlled at any specified increment. Although the physical experiments and DEM simulations were conducted in the same ranges of fluid velocities, fluid velocities are not quantitively compared between experiments and simulations due to the limited precision in controlling fluid velocity in the flume.

Particles eroded from the initial DEM configurations can be exactly tracked throughout the simulations whereas particles eroded during the experiments are manually counted and summed for a specific fluid velocity. Therefore, the nature of collecting data for the flume experiments versus writing data to an output file during the DEM simulations also lends to slight differences in the data collection.

**Results and Discussion**

The simulations and experiments performed for both slopes are summarized in Table 4-2. The results for untreated packings are presented first and comparisons are made between the simulations and experiments. Next, the results from the surface treatment of the layer of steel particles are presented and compared to the untreated cases for both simulations and experiments. Only experiments were performed for the surface treatment of the agricultural straw and results are presented and compared as a function of application rate to the untreated cases and between application rates. Throughout the discussion of results, comparisons are also made between particle packing slopes.

Table 4-2: Summary of Simulations and Experiments

| Surface Treatment | Simulation (S) or Experiments (E) and Key Behaviors Plotted |
|---|---|
| Untreated | S - slope of linear erosion rates versus fluid velocity |
| | E - slopes of piecewise linear erosion rates versus fluid velocity |
| Layer of steel particles | S - decreased slope of linear erosion rates versus fluid velocity compared to untreated |
| | E - decreased slope of linear erosion rates versus fluid velocity compared to untreated |
| Straw 1.12 Mg/ha | Experiments<br>1) piecewise linear erosion rates versus fluid velocity<br>2) increased failure fluid velocities compared to untreated and as a function of increased straw application rate |
| Straw 2.24 Mg/ha | |
| Straw 5.60 Mg/ha | |
| Straw 11.21 Mg/ha | |

*Untreated Particle Packings*

Screenshots of the DEM simulation and photographs of the physical experiment on untreated glass particles with a 6º slope are shown in Figure 4-4. In the physical experiments, water gradually filled the voids around the particles until surficial flow conditions developed and particles began to erode at the left side of the packing. Fluid forces acting on the left-most particle in the physical experiment were higher than modeled in the DEM simulation (discussed previously), and thus the left-most surface particles in the experiments (Figure 4-4b and d) eroded at a fluid velocity of approximately 0.42 m/s. In contrast, the surface layer of particles in the DEM simulation started to erode together at a fluid velocity of 0.68 m/s (Figure 4-4c). Similarities in particle erosion behavior are highlighted in Figure 4-4c for the simulation (fluid velocity = 0.68 m/s) and Figure 4-4f for the experiment (fluid velocity ≈ 0.76 m/s). In the DEM simulation, 44 particles eroded at a fluid velocity of 0.81 m/s, whereas in the physical experiments, 44 particles eroded at an average fluid velocity of 0.92 m/s (Figure 4-4h).

Fluid velocity of ~0.42 m/s

a) No movement

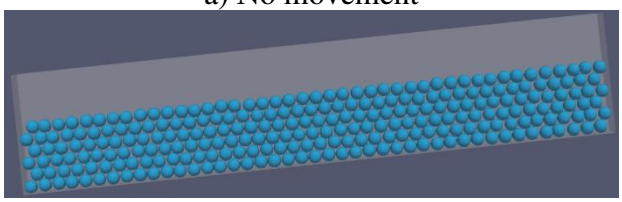

b) Left-most particles begin to displace

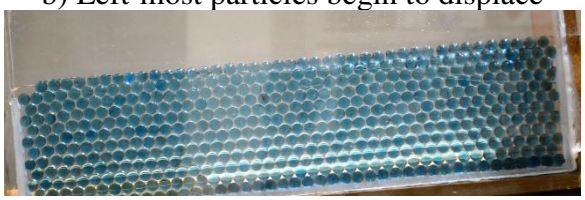

Fluid velocity of ~0.68 m/s

c) Particle movement is initiated

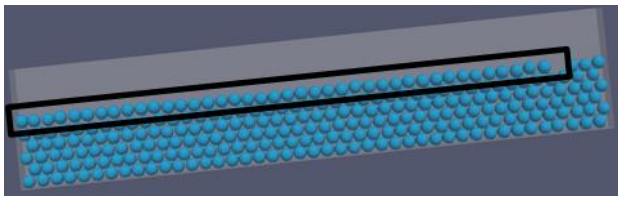

d) Eight particles (on average) washed away; one at a time

Fluid velocity of ~0.76 m/s

e) Particles in motion

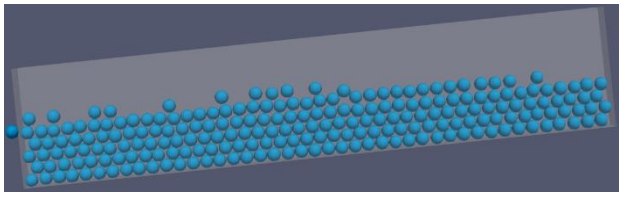

f) Same particle movement as simulation at 0.68 m/s (Figure 4-4c)

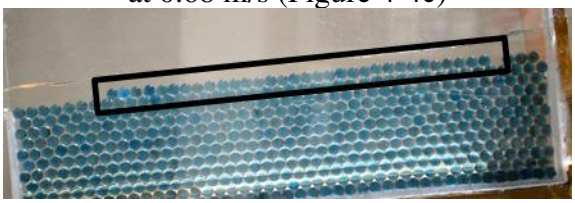

Final Configurations

g) 62 particles eroded at a fluid velocity of 0.88 m/s

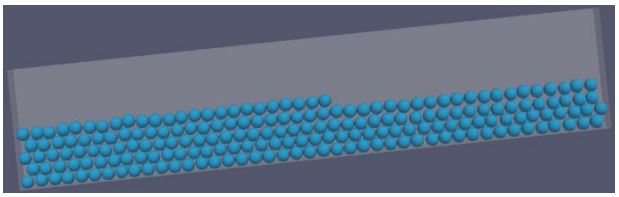

h) 44 particles (on average) eroded at a fluid velocity ≈ 0.92 m/s

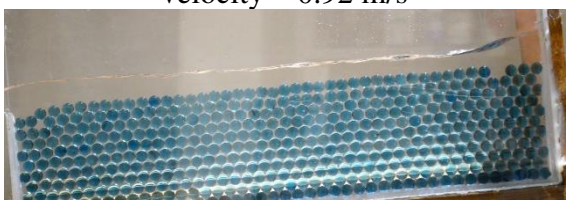

Figure 4-4: Example progression of the untreated geometry simulation (left) and experiment (right) on the 6º slope.

The relationships between particles eroded during the experiments and simulations versus fluid velocity are shown in Figure 4-5 for slopes of 6° and 11°. As previously noted, the left-most particles washed away one by one during the experiments as fluid velocity increased, whereas particles in the DEM simulation experienced a nearly complete intact movement along the top row of particles. This phenomenon is observed as a slower accumulation of eroded particles during

the physical experiments as fluid velocity increased. In contrast, trends of eroded particles versus fluid velocity from the DEM simulations depict the onset of erosion at a specified fluid velocity (i.e., *x*-axis intercept) and more consistent loss of particles with increasing fluid velocity. The simulation results were linear, and the behavior of the experiment plots can be described as piecewise linear. The slope magnitudes are shown beside each line in the plot. The slopes depict how many particles would be eroded with an increase in fluid velocity of 1.0 m/s, however only the magnitudes will be discussed.

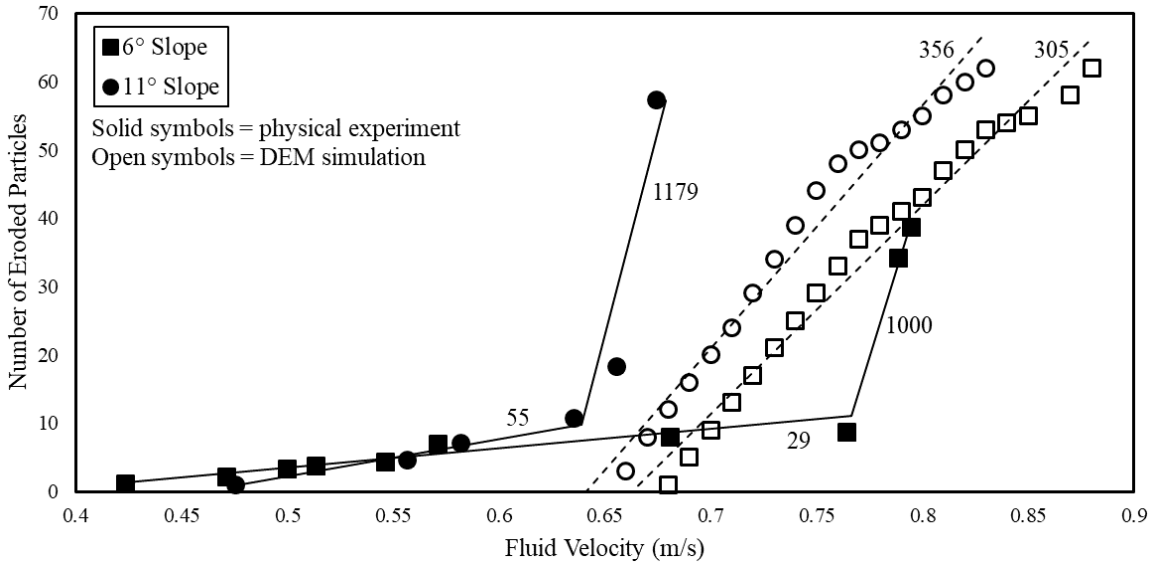


Figure 4-5: Eroded particles as a function of fluid velocity for untreated packings with trendline slopes given.

At low fluid velocities (0.4 – 0.6 m/s) particle motion was resisted (completely during the simulations) and this corresponds to the initial smaller sloped linear trend for the experimental data. Once substantial particle motion began, a large number of particles were subsequently eroded. This failure behavior is shown on Figure 4-5 by the steeper sloped linear trends after 0.63 m/s for the 11° experiment data and after 0.76 m/s for the 6° experiment data. As expected, for both the simulations and experiments, particles eroded at lower fluid velocities (as well as lower rates depicted by the trendline slopes) on the steeper slope than for the smaller slope. The slopes

of the failure regions of the physical experiments (second line on the piecewise linear functions) are about the same, with the 11° slope data resulting in a slightly higher rate of eroded particles versus fluid velocity. The same comparison is made between the DEM simulations. Specifically, for the untreated slopes, the DEM simulations and physical experiments showed that an increase in slope of 5° resulted in an average increase in erosion rate as a function of fluid velocity of 17.3% (16.7% for simulations and 17.9% for experiments in the failure range).

Comparing between the experiments and simulations, for both the 6° and 11° slopes, the slopes of the experiment data in the failure range are a multiple of 3.3 times the slopes for the respective simulations. The differences in rates of particles eroded versus fluid velocity can be attributed to the application of the fluid forces, with the velocity increased an average of 0.05 m/s approximately every 15 s for the experiments versus exactly 0.01 m/s every 0.25 s in the simulations. The steady, exact nature of the fluid force application in the simulations seems to have resulted in the steady, linear erosion of particles shown on Figure 4-5. However, overall similar trends are observed between the experiments and simulations as well as similar numbers of eroded particles.

*Influence of Steel Particles as Surface Treatment*

A side by side comparison is made between the layer of steel particles surface treatment experiments and simulation in Figure 4-6 for the 6° slope. Both the experiments and simulations had particle erosion start with the weight from the left-most steel particle pushing the left-most glass particle out of the control domain, shown at the upper left corner of Figures 4-6a and 4-6b. For the simulation (Figure 4-6a) this occurred at a fluid velocity of 0.67 m/s and for the experiments (Figure 4-6b) between 0.47 and 0.55 m/s. For the same reason as described for the

untreated cases, the layer of steel particle experiments had particle erosion occur at lower fluid velocities than the simulation. Example final configurations are shown in Figure 4-6c for the simulation and Figure 4-6d for the experiment.

a) Simulation initial particle movement

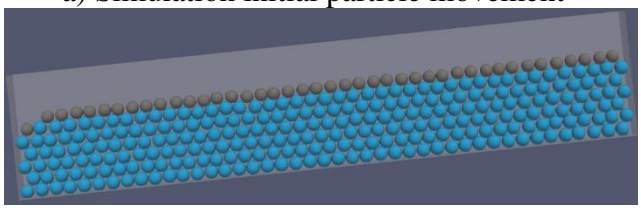

b) Experiment initial particle movement

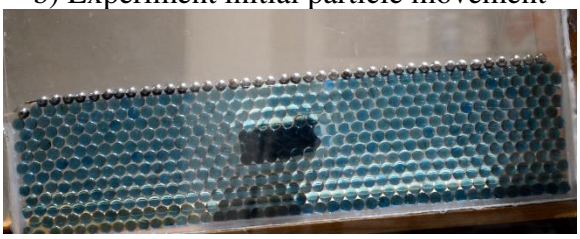

c) Simulation final configuration

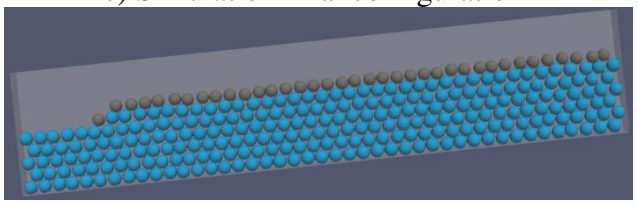

d) Experiment final configuration

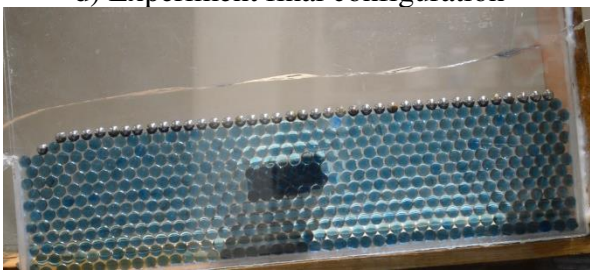

Figure 4-6: Layer of steel particles simulation (left) and experiments (right) for the 6º slope.

Eroded particle rates as a function of fluid velocity are plotted in Figure 4-7 for the 6º and 11° slopes to compare the untreated experiments and simulations with the layer of steel particles surface treatment. The data is not shown above 35 particles to show a higher resolution of the lower values of eroded particles. Again, the slope magnitudes are shown beside each trendline and they signify how many particles would be eroded with an increase in fluid velocity of 1.0 m/s.

a) 6° Slope

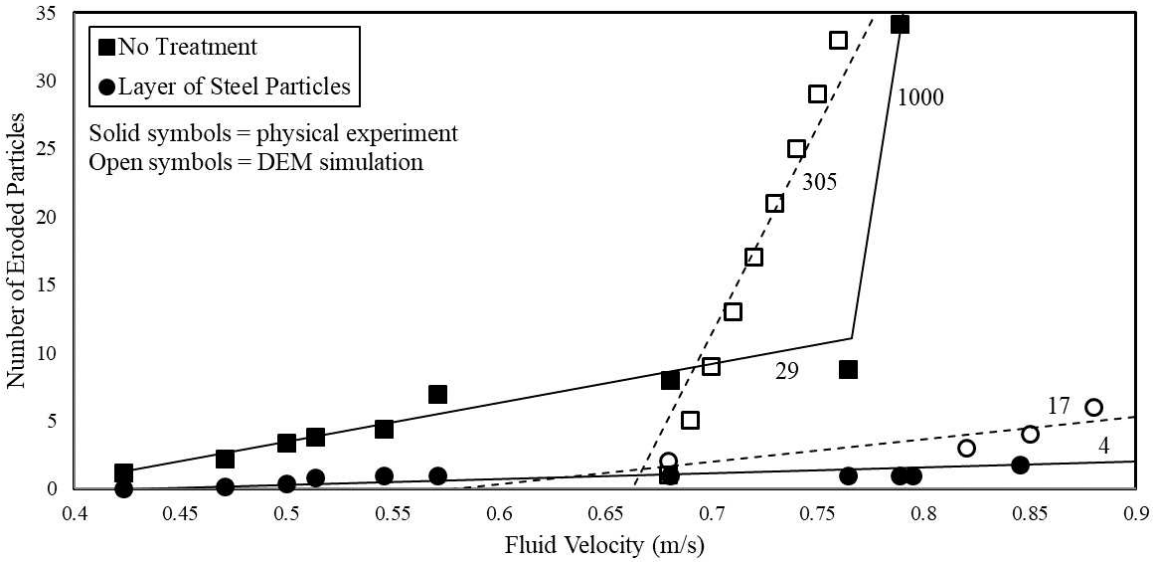


b) 11° Slope

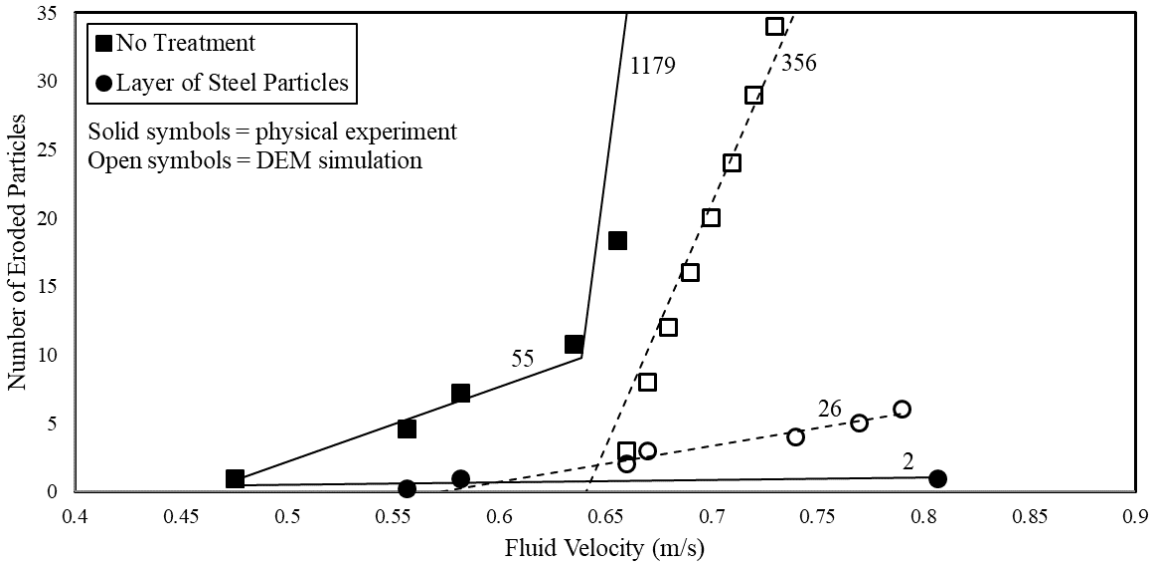


Figure 4-7: Eroded particles as a function of fluid velocity for layer of steel particles surface treatment and untreated packings with trendline slopes given.

The steel ball bearings were effective at inhibiting particle movements, even at high flow rates, and the treated particle packings resulted in significantly decreased particle erosion in both the physical experiments and DEM simulations. The surface treatment results are smooth, have much smaller slopes as compared to the untreated counterparts, and resist catastrophic particle motion over the entire range of fluid velocities (i.e. no piecewise linear behavior as for the

untreated experiments). With respect to total eroded particles, the simulations and experiments for both slopes decreased particle erosion by an average of 90%, with a standard deviation of 0.71% (89% average decrease for the 6° experiments, 91% average decrease for the 11° experiments, and a 90% decrease for the simulations at both slopes).

*Influence of Straw Mulch as Surface Treatment*

Straw mulch application rates of 1.12, 2.24, 5.60, and 11.21 Mg/ha (dry mass basis) were used as surface treatments and an example progression of the 11.21 Mg/ha treatment experiments is shown in the photographs of Figure 4-8. Before the straw was washed away, the left-most particle(s) was again picked away at lower velocities (Figures 4-8b and 4-8c), although still at higher velocities than the untreated cases. As the water level rose, the straw was lifted (floated, Figure 4-8d) and then washed away once dislodged from the glass particles beneath (Figures 4-8e and 4-8f). The water levels in the photographs are shown by the line near the water entrance. After the straw was washed away, "catastrophic" failure occurred and large numbers of particles were eroded (as many as were eroded during the untreated experiments) once exposed to the higher hydraulic forces. Therefore, final numbers of particles eroded are not compared for the straw treatment cases as were for the layer of steel particles treatment cases.

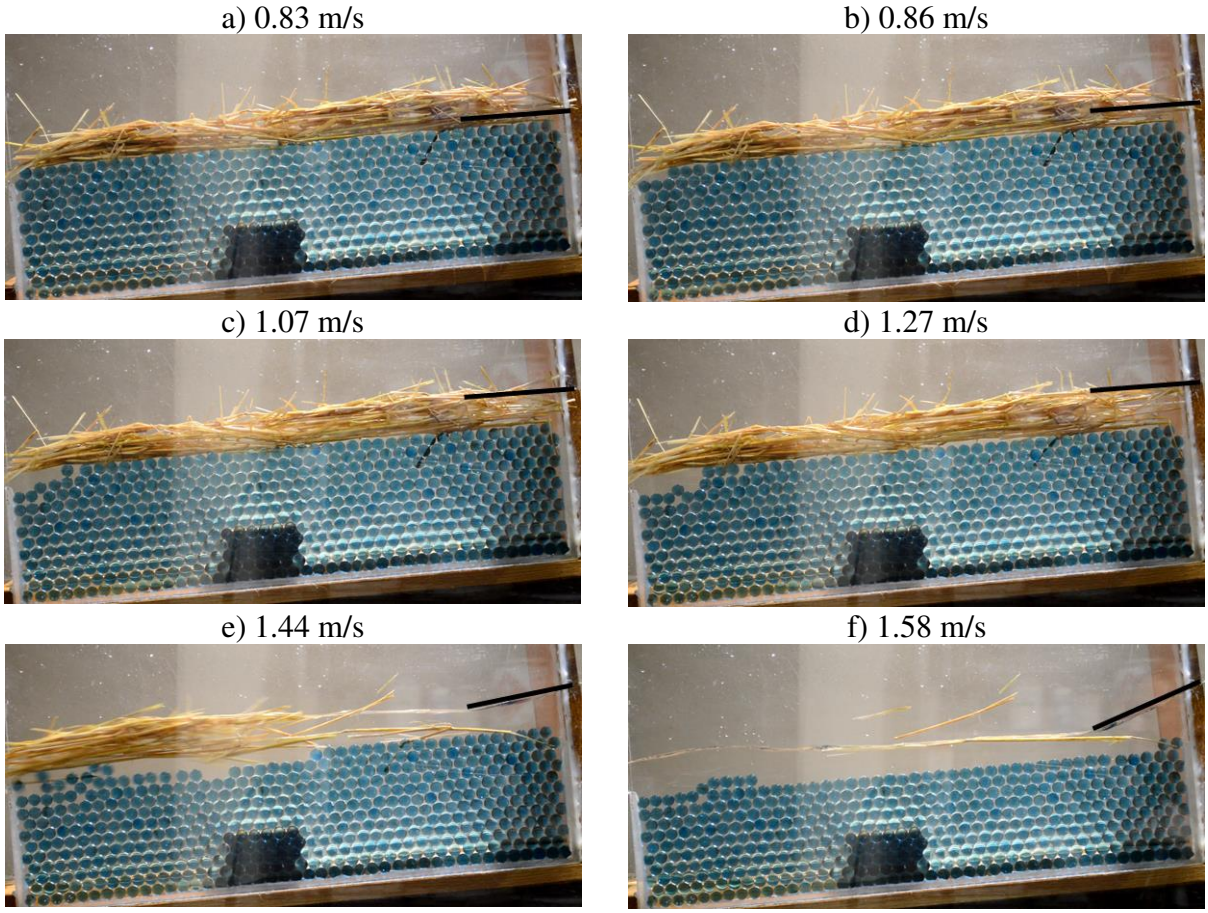


Figure 4-8: Example Progression of a 11.21 Mg/ha Straw Treatment Experiment on the 6º slope. Approximate fluid velocities are shown above each photograph and water levels shown with lines at the right sides of the photographs.

Eroded particles versus fluid velocity for the straw surface treatments are plotted in Figure 4-9 for the 6º and 11° slopes. Trendlines are plotted for the data in the catastrophic failure region. Next to each trendline, the *x*-axis intercept is shown, depicting the fluid velocity at which the onset of catastrophic erosion occurs.

a) 6° Slope

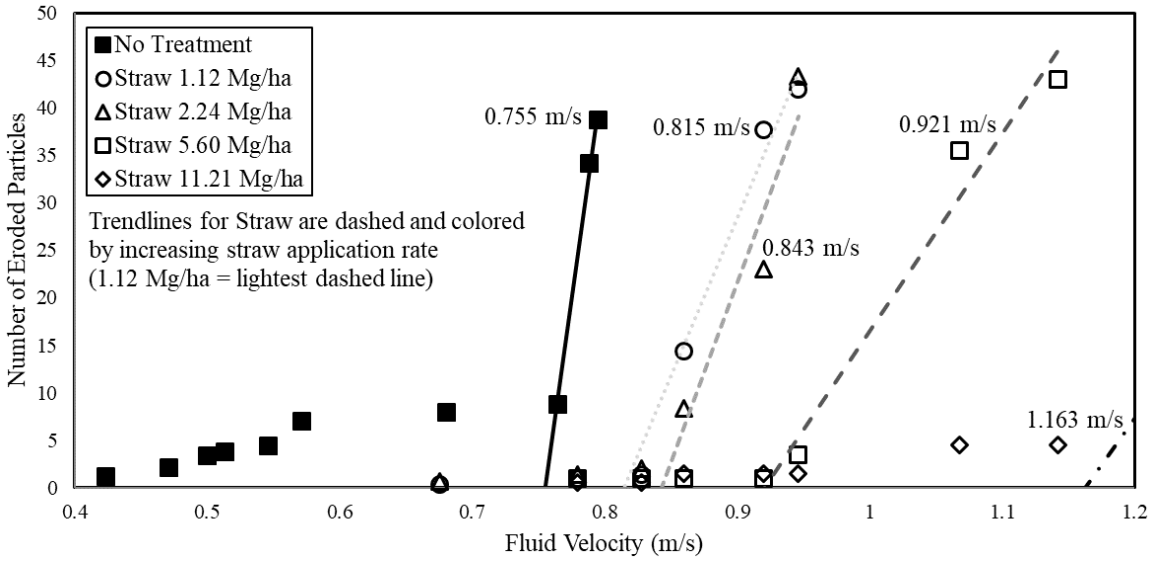


b) 11° Slope

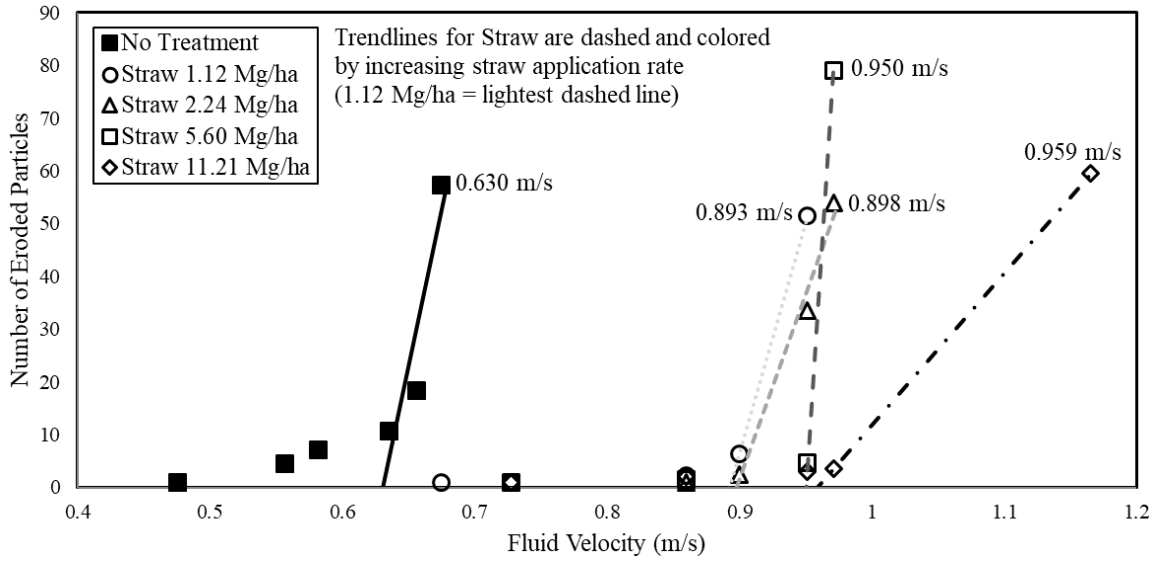


Figure 4-9: Eroded particles as a function of fluid velocity for straw treatments with velocities at primary mass movement given.

As the surface treatment mass increased, particle erosion was decreased. The straw treatment cases fall to the right of the untreated experiment data. For both slopes, the least number of particles were eroded during the highest straw treatment rate experiments (11.21 Mg/ha) as the fluid velocity increased. Initial particle movement was consistently delayed when the straw treatments were in place. From the untreated case to the lowest straw treatment case (1.12 Mg/ha),

the fluid velocity at which particle movement initiated increased by an average of 60% for the 6° slope and 42% for the 11° slope. From the untreated case to the highest straw treatment case (11.21 Mg/ha), the fluid velocity at which particle movement initiated increased by an average of 84% for the 6° slope and 53% for the 11° slope.

The fluid velocities labeled next to each trendline in Figure 4-9 represent the *x*-axis intercept of the second linear portion (of the overall piecewise linear behavior) representing when catastrophic failure occurred and large numbers of particles were eroded. The data shows that increased straw mass increases the fluid velocity at which catastrophic failure is initiated. A comparison of the failure fluid velocities is shown in Table 4-3 for the straw treatment experiments. The fourth column is the percent increase in the failure fluid velocity of each surface treatment compared to the untreated case. The percent increases are then compared in Figure 4-10.

Table 4-3: Percent Increases in Fluid Velocities Corresponding to Large Erosion Rates for the Straw Surface Treatment Experiments Compared to the Untreated

| Slope | Added surface mass | Failure fluid velocity (m/s) | % increase from untreated |
|---|---|---|---|
| 6° | None (untreated) | 0.755 | - |
| | + 1 gram (1.12 Mg/ha) | 0.815 | 8% |
| | + 2 grams (2.24 Mg/ha | 0.843 | 12% |
| | + 5 grams (5.60 Mg/ha) | 0.921 | 22% |
| | + 10 grams (11.21 Mg/ha) | 1.163 | 54% |
| 11° | None (untreated) | 0.630 | - |
| | + 1 gram (1.12 Mg/ha) | 0.893 | 42% |
| | + 2 grams (2.24 Mg/ha | 0.898 | 43% |
| | + 5 grams (5.60 Mg/ha) | 0.950 | 51% |
| | + 10 grams (11.21 Mg/ha) | 0.959 | 52% |

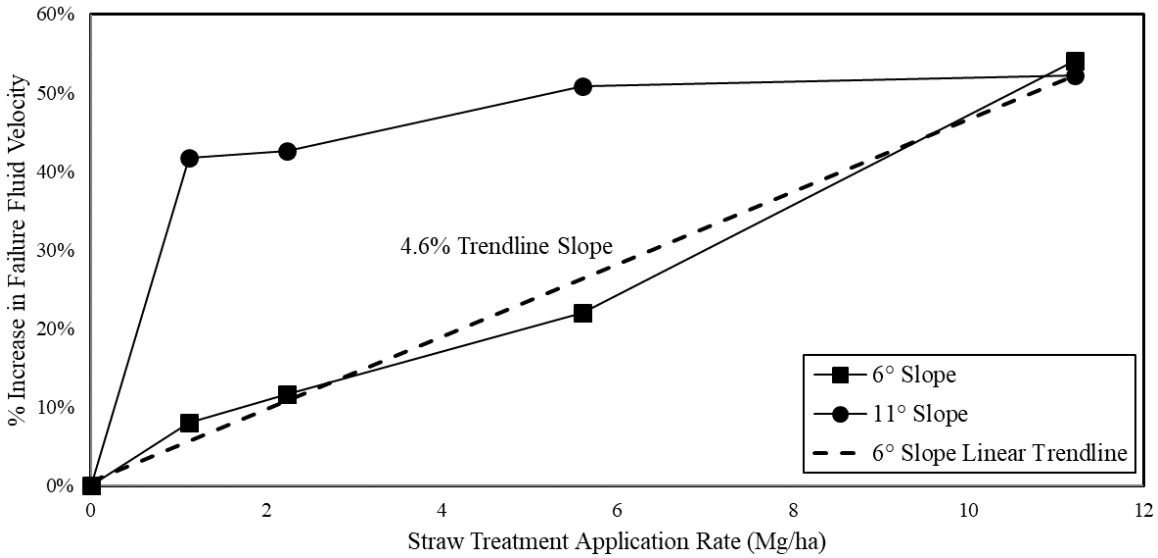


Figure 4-10: Percent increases in failure fluid velocity versus application rate for straw treatment experiments.

The trends shown in Table 4-3 and Figure 4-10 suggest that at higher slopes there may be a point of diminishing returns with increased surface treatment application rates. For the 6° slope, the increase in failure fluid velocity linearly increases as a function of increased added mass on the surface. The slope of the linear trendline on Figure 4-10 shows that for the 6° slope, there is a 4.6% increase in failure fluid velocity for every 1 Mg/ha increase in straw application rate. Contrarily, for the 11° slope, the initial addition of added mass on the surface (1.12 Mg/ha) increases the failure velocity by 42% and then 10 times the added mass (1.12 Mg/ha to 11.21 Mg/ha) only increases the failure velocity by another 10%.

Moden (2018) performed rain experiments on burned soil samples with a range of straw mulch applications and results of straw mulch application rate versus total sediment yield are shown in Figure 4-11a. The same straw mulch material was used between both Moden's rain experiments and the flume experiments presented herein. Although there are different hydraulic loading mechanisms being explored (rainfall versus surficial flow) between Moden's work and the research presented here, both attempt to evaluate the effects of increasing straw mulch application

rates on erosion. The total sediment yield shown in Figure 4-11a can be compared with particles eroded during the flume experiments (both a function of mass exiting the experiments). A comparison of particle erosion as a function of the added mass for the 11° slope at a fluid velocity of ~0.95 m/s for the flume experiments is shown in Figure 4-11b. The average number of particles washed away for the untreated (zero application rate) and the straw treatment experiments are plotted. For comparison with Moden's data, the straw application rates (1.12 Mg/ha, 2.24 Mg/ha, 5.6 Mg/ha, and 11.21 Mg/ha) were converted from Mg/ha to kg/m$^2$ (1 Mg/ha = 0.1 kg/m$^2$). The fluid velocity of ~0.95 m/s was chosen for the mulch application rate comparison, because just before that velocity was when failure began to occur for the experiments (increased slopes for data sets on Figure 4-9b at ~0.95 m/s and velocities shown in Table 4-3 for 11° slope).

a) Relationships of total sediment yield versus straw mulch application for successive simulated rainfalls (adapted from Moden (2018))

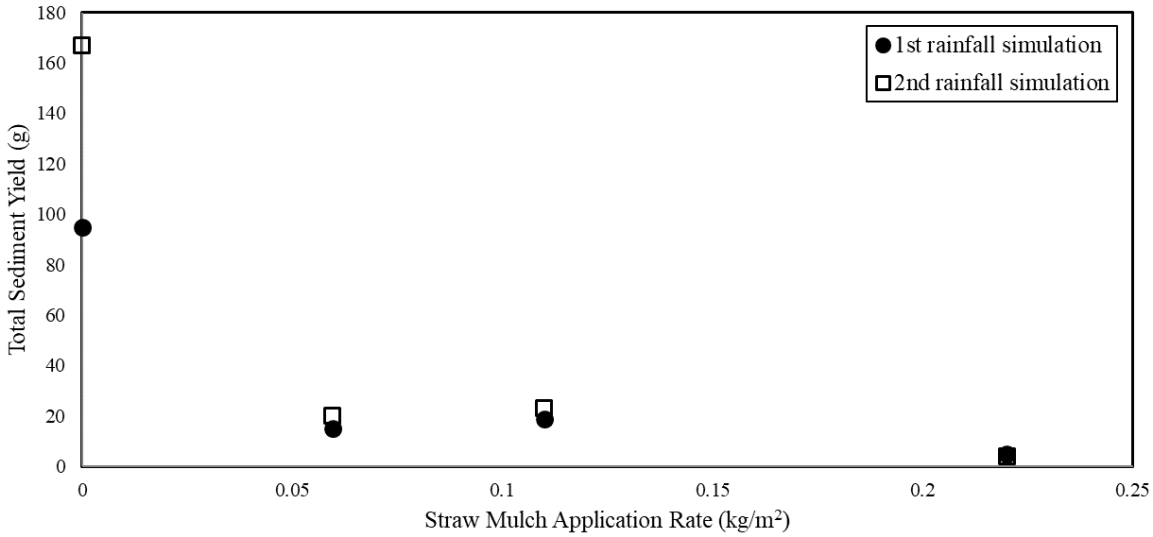


b) Relationships of eroded particles versus straw mulch application rate for the 11° slope experiments at a fluid velocity of ~0.95 m/s

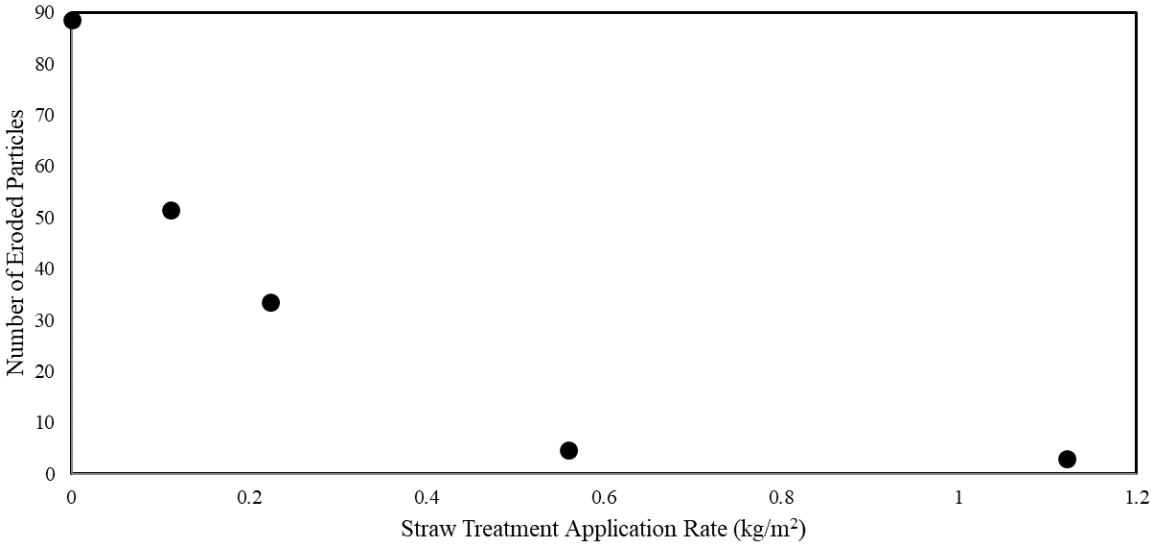


Figure 4-11: Comparison between Moden (2018) and Flume Experiments.

Figure 4-11a and 4-11b show similar trends where the sediment yield (or number of eroded particles) was reduced with any straw mulch application applied on the surface. The flume experiments tested a larger range of straw mulch application rates. Moden's experiments found that the total sediment yield was greatly decreased with the lowest rate of straw mulch application, while the number of eroded particles decreased at a slower rate for the flume experiments. This

difference can be attributed to the relatively high surficial flow velocity of ~0.95 m/s acting on the straw versus the rain forces. Although the driving hydraulic forces are different between the two sets of experiments, they both directly test the changes in sediment yield with increased straw mulch application.

*Discussion*

The results from the layer of steel particle simulations and experiments show that if the surface mass is large enough, particle erosion can be greatly reduced when subjected to a large enough surface traction. The layer of steel particles added a total mass of 353 grams to the surface of the particle packing, versus an added mass of 10 grams for the largest agricultural straw surface treatment. Specifically, all of the simulations and experiments reinforced by a layer of steel particles exhibited a decrease in erosion by an average of 90% when compared to the untreated cases. There was no difference in magnitude of decreased erosion between the two slopes.

If the surface mass is not large enough to stop most erosion, then the particle erosion rates under surficial flow are dominated by piecewise linear behavior (Figures 4-7 and 4-9) as a function of eroded mass versus fluid velocity. This shape of the plots indicates a) an initial resistance to flow that is based on gravitational restrain of the surface treatment, followed by b) movement that induces widespread failure or erosion at a much higher rate. Overall for the experiments, initial particle movements were delayed until higher fluid velocities as the surface treatment masses were increased. Also, the failure fluid velocity was increased for all surface treatments compared to the untreated cases. For both slopes the failure fluid velocity was increased by over 50% when the highest treatment mass is compared to the untreated cases. However, unlike the layer of steel particles surface treatment, there were differences between the two slopes for the agricultural straw

surface treatments. At a smaller slope of 6°, the failure fluid velocity steadily increased as surface treatment mass increased. Whereas at a larger slope of 11°, there was almost no difference in failure fluid velocity between the first two and last two surface treatment masses, and only an additional 10% increase after the initial 40% increase for 10 times the amount of added mass. These results show that particle erosion is more dependent on differences in surface treatment application rate at lower slopes; whereas at higher slopes, just an initial surface treatment application (as low as a 1.12 Mg/ha rate) makes a large difference in erosion compared to untreated.

## Conclusions

This research investigated the hypothesis that compressive stress from added mass on the surface of particles contributes to the effectiveness of surface treatments in decreasing erosion. A DEM model and a physical experiment were developed and tested, and simulations and experiments were performed on semi two-dimensional glass particle packings with different types and amounts of surface treatments. Particle erosion was tracked as a function of fluid velocity for each simulation and experiment. Surface treatments included a layer of steel particles and differing application rates of agricultural straw.

Overall, the results from the simulations and experiments indicated that surface treatments acted to decrease particle erosion and/or delay particle motion. Results from both the DEM simulations and flume experiments support the hypothesis and good agreement was found between the simulations and experiments for the untreated and layer of steel particles surface treatment cases. Specific conclusions from the work are bulleted here:

- A correlation exists between added mass on the surface of a particle packing and decreased erosion under surficial flow conditions.
    - For the glass spheres tested here, eroded mass was consistently decreased by an average of 90% with increased surface mass for the large added mass of the steel particles surface treatment.
- As slope increases, erosion rates increase.
    - For the untreated slopes, the DEM simulations and physical experiments showed that an increase in slope of 5° resulted in an average increase in erosion rate as a function of fluid velocity of 17.3%.
- If the surface mass is not large enough to stop most erosion, the particle erosion rates under surficial flow are dominated by piecewise linear behavior as a function of eroded mass versus fluid velocity, indicating an initial resistance to flow followed by widespread failure or erosion at a much higher rate.
- On lower sloped particle packings treated with straw, the surficial flow fluid velocity needed to cause substantial particle erosion is linearly dependent on the application rate.
    - For the straw treatment experiments on the 6° slope, there was a 4.6% increase in failure fluid velocity for every 1 Mg/ha increase in straw application rate.
- On higher sloped particle packings treated with straw, the surficial flow fluid velocity needed to cause substantial particle erosion is not dependent on the application rate. Rather, the results indicate there is little advantage of higher application rates after a certain point and there exists a point of diminishing return with respect to straw application rate.
    - For the 11° slope, the initial addition of added mass on the surface (1.12 Mg/ha) increased the failure fluid velocity by 42%. Then doubling the treatment rate only

increased the failure fluid velocity by another 1%. Finally, 10 times the treatment rate (1.12 Mg/ha to 11.21 Mg/ha) only increased the failure velocity by another 10%.

The overarching goals of this research were not only to assess the effect of increased surface mass on particle erosion, but also to provide insight to a tool, a DEM model, that has the potential to assess surface treatment effectiveness numerically, before conducting large scale field studies. Future work building on the research presented here could lead to a better understanding of the physical process of particle erosion with surface treatments in place, investigate modelling techniques for non-spherical surface treatments, and allow for rapid assessment of erosion mitigation controlling parameters.

# Chapter 5 : NUMERICAL EVALUATION OF THE ERODIBILITY OF PARTICLE PACKINGS WITH SPRING REINFORCEMENTS USING THE DISCRETE ELEMENT METHOD[2]


## Summary

The erodibility of three-dimensional particle packings reinforced numerically with elastic springs and subjected to overland flow conditions was explored using the discrete element method (DEM). Particle packings at three slopes, subjected to overland flow at two fluid velocities, and four reinforcement configurations resulted in a total of 24 datasets of simulation results for comparisons to be made. The three slopes were composed of the same 2400 particles with coarse sand material properties and a uniform distribution of diameters between 1.8 and 8.0 millimeters. The elastic spring reinforcements represent a potential modeling technique for root development in a soil. The spring reinforcement technique presented here is a proof-of-concept attempt to model three-dimensional slopes at up-scaled particle sizes, root stiffness, and fluid velocities. Particle displacements were tracked and compared as functions of time, reinforcement level, and slope. The results suggest linear relationships between decreased particle movement with increased percent reinforced surface particles, increased particle movement with increased slope, and decreased sediment yields with increased percent reinforced surface particles. Also, at the lower fluid velocity, particle displacements were more dependent on incremental changes in slope; whereas at the higher fluid velocity, particle displacements were not dependent on small changes in slope. Overall, the results from the simulations and experiments showed the influence of elastic spring reinforcements on particle movements and the next step of the research would be to assess the scaling effects and apply the root model to smaller particles, more indicative of where roots


[2] Peterson, K.L., Bareither, C.A., and Heyliger, P.R. (to be submitted) *Granular Matter, Springer*

are expected to grow.

## Introduction and Background

Soil erosion is the process of soil particles being physically transported by factors such as water, wind, ice, or earthen mass (Julien, 2010). For soil, vegetation is the most effective long-term erosion control measure (Demars et al., 2004). Figure 5-1 shows a schematic of the differences in runoff and sediment transport between a vegetatively reinforced slope versus a relatively bare slope. Soil erosion due to overland flow conditions are a concern for unreinforced soil slopes (no vegetation present) because less infiltration, higher runoff velocities, and more sediment transport are associated with these surface conditions.

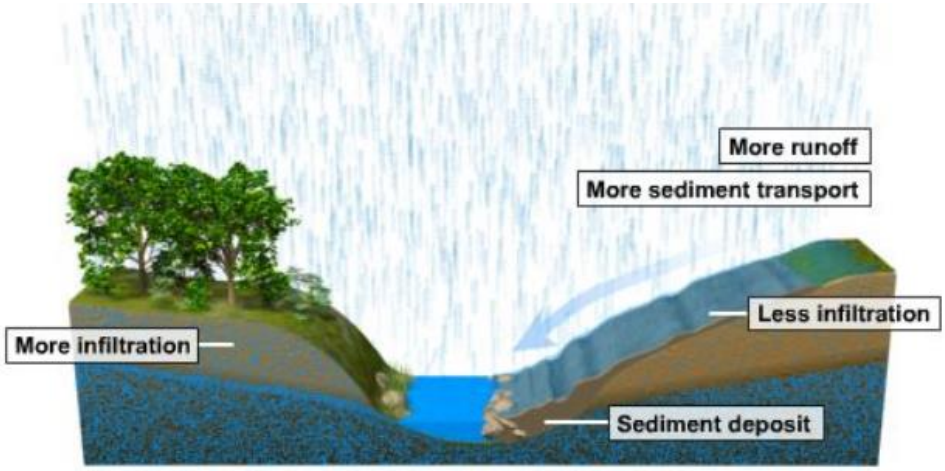


Figure 5-1: Influences of ground cover loss on runoff, groundwater, and sediment transport (University Corporation for Atmospheric Research, 2010).

The natural recovery of native vegetation reduces erosion over time and soils with more vegetation and organic matter have been shown to have higher infiltration rates and a more reinforced and strengthened soil structure (Robichaud et al., 2010). Vegetation the preferred long-term erosion control measure for several conditions, including burned soil slopes, stream banks, and grass-lined channels used to convey stormwater runoff. In general, studies have shown that

natural vegetation effectively protects against erosion if the slope is not greater than ~70° and the surficial flow velocity is not greater than 1.5 m/s (Halff Associates, 1998). Increased erosion is expected after a fire, because burned soils are more susceptible to unusual volumes of overland flow (Geertsema et al., 2010) and therefore increased sediment yields after a storm. Different plants are chosen for stream bank erosion control depending on the distance from the average stream flow (terrace, bank, splash, or toe zones) (Halff Associates, 1998). For grass-lined channels, the vegetation has been shown to slow down the runoff velocity and increase infiltration (Smolen et al., 2001). Large-scale field studies have drawn conclusions about reduced sediment yields with increased vegetative growth. For example, Schmeer et al. (2018) collected measurements on ground cover, rainfall, topographic, and sediment yield from 29 hillslopes over a period of two years after the High Park Fire in northern Colorado. One of the uses of the data was to develop an empirical model to predict sediment yield as a function of percent bare soil. Also, the data collected showed that a year after the fire there was, on average, about 15% live vegetative ground cover and the most recent data showed the percent live vegetative ground cover reaching a maximum of 50-60% three years after the fire. All increases in ground cover corresponded to decreased sediment yields tracked.

Although shown with large-scale field studies, there is little research published on analyzing the effect on erosion that root development has in a soil using the discrete element method (DEM). The DEM is a convenient modeling technique used to represent granular matter as an idealized assembly of particles with overall macroscopic behavior resulting from the collection of all particle interactions (O'Sullivan, 2011). The research presented here tests the hypothesis that decreased erosion that occurs as a function of increased root development can also be shown using the DEM to model root reinforcements numerically with elastic springs. To test

this hypothesis, simulations were performed using a DEM model, with reinforcements simulated as elastic springs. Physically, this modeling technique attempts to represent roots bonded to the particles, acting to reinforce them and stabilize the slope. The spring reinforcement technique presented here is a proof-of-concept attempt to model three-dimensional slopes under overland flow conditions with reinforcements present and assess the simulation results with modifications made to the slope, fluid velocity (therefore, hydraulic force magnitude), and amounts of reinforcement. Specifically, simulations were performed on three slopes with two fluid velocities and four reinforcement amounts (including control unreinforced geometries) to test the hypothesis.

An overall schematic of the processes modelled in the DEM simulations is shown in Figure 5-2. Overland flow conditions exist on the surfaces of the equilibrated three-dimensional particle packings, reinforced surface particles are connected to particles beneath the surface with elastic springs (representing a root in actual soil), and particles that exit the boundary on the right are no longer included in calculations and the masses are used to calculate percent sediment yields. More detailed descriptions on how these processes are modelled are included in subsequent sections.

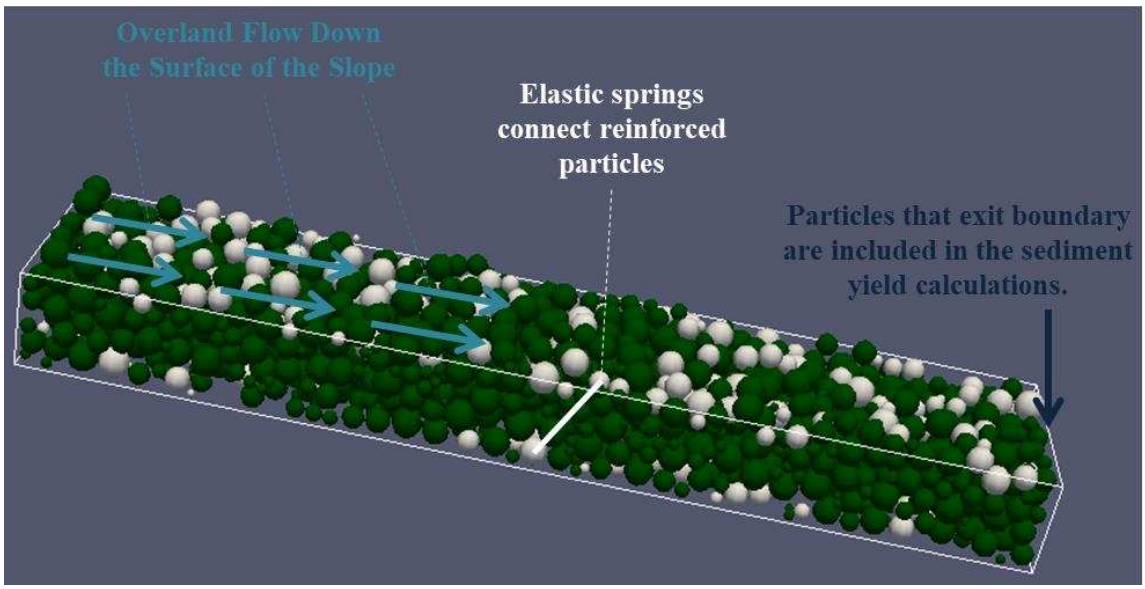

Figure 5-2: Schematic of processes modelled in the simulations. Reinforced particles are white.

The particles simulated for this research have diameters representative of coarse sand particles. Although the particles are larger then what would be typical of a soil where vegetation develops for erosion protection, the simulations are a first effort towards analyzing a new approach to modeling roots using the DEM. The sizes of the particles allowed for a physical soil volume of 375 $cm^3$ to be modeled with 2400 particles and simulations could be performed in reasonable computational times. The research is a proof-of-concept attempt and the particle size range, along with the root stiffness and overland flow fluid velocities, are upscaled. Future research would allow for smaller particles, more indicative of where roots are expected to grow, to be simulated.

**The DEM Model**

Specific details on the theory used for DEM analyses were originally presented by Cundall and Strack and can be found elsewhere ((O'Sullivan, 2011; Cundall & Strack, 1979). The DEM model developed for the research presented here was validated using Tests 1, 2, 3, 4, and 7 from the set of benchmark tests proposed by Chung and Ooi (2011). Details on the contact models,

damping, and hydraulic loading will be discussed.

*Normal Contact Model*

The contact model for normal contact forces between two particles was the simplified Hertzian contact model. The contact stiffness is a function of the radii, shear moduli, Poisson's ratios, and overlap distance of the two particles in contact. The equations amount to an effort to replicate the actual deformation between two elastic spheres with a relatively simple one-dimensional relationship rather than using the full equations of three-dimensional elasticity. The normal contact force between the particles is then calculated by multiplying the stiffness by the sphere overlap distance. The simplified Hertzian contact model is effective for use in DEM simulations because the model provides a logical basis for the link between spring stiffness and actual material properties.

*Tangential Contact Model*

The DEM model used a simplified Mindlin-Deresiewicz tangential contact model (Mindlin & Deresiewicz, 1953; Vu-Quoc et al., 2000) for the tangential forces between two particles, where tangential stiffness is a function of the current normal stiffness and the Poisson ratios of the particles in contact. Tangential contact forces differ from normal contact forces, because the stiffness is not simply multiplied by the sphere overlap distance, but rather by the summed incremental tangential displacements (relative velocities multiplied by the time increment) occurring throughout the contact. The relative velocity between the particles for each time step is a function of the translational velocities, rotational velocities, and centroidal locations of each particle and are calculated using the permutation tensor multiplied by the time increment and

summed throughout the contact. The tangential forces are then added to the normal forces and also cause moments about the centers of the particles. Finally, the tangential forces are limited by a Coulomb friction criteria based off a defined friction coefficient between the particles.

*Damping*

One limitation to the simplified Hertzian contact model is that the energy dissipation that occurs physically is not captured (O'Sullivan, 2011). Particle-particle contact damping is applied, with a specified coefficient, to alleviate issues with non-physical particle vibrations. Mass damping (also called global damping), originally proposed by Cundall and Strack (1979), is also applied with a specified coefficient. Mass damping is applied to the resultant velocities of each particle. The details for both particle-particle contact damping and mass damping can be found elsewhere (O'Sullivan, 2011).

*Hydraulic Loading*

The overland flow conditions were simulated by subjecting surface particles to drag forces. The drag force is given with the following equation for drag force on a sphere, accounting for properties of the fluid (Julien, 2010):

$$F_D = \frac{1}{2}\rho V^2 C_d A_i \qquad \text{[Equation 5-1]}$$

where $\rho$ is the density of the fluid (1,000 kg/m$^3$ for water), $V$ is the velocity of the fluid flow, $C_d$ is a shape factor (0.5 for spheres (The Engineering Toolbox, 2004)), and $A_i$ is the projected surface area of particle $i$ perpendicular to the flow ($A_i = \pi R^2$ for spheres with radius $R$). Fluid velocities of 0.25 and 0.50 m/s were simulated. A study performed by Emmett (1970) reported measurements of overland flow fluid velocity on hillslopes during a rain event to be a maximum of about 0.15

m/s, therefore the fluid velocities explored here are scaled above this value. Preliminary simulations on the particle packing explored here under a surficial fluid velocity of 0.10 m/s showed that no movement occurred, and the slopes were stable.

To avoid sudden instabilities, the velocities simulated were linearly increased from zero to full value over a time period of two seconds and were then held at full value for the durations of the simulations. The fluid velocities used were estimated from physical overland flow velocities expected for soil slopes, usually calculated as a function of distance, uniform-flow friction-slope, friction factors, and rainfall excess (Kilinc & Richardson, 1973). The drag forces were applied horizontally on the surfaces of the particles. These forces created a moment acting at the center of each of the surface particles about the axis into the plane.

*Spring Reinforcements*

The elastic spring reinforcement forces were simulated in this DEM model by connecting the centers of surface particles to centers of deeper particles by springs with a specified stiffness. The connected surface particles are referred to as reinforced particles and a schematic of this is shown in Figure 5-3.

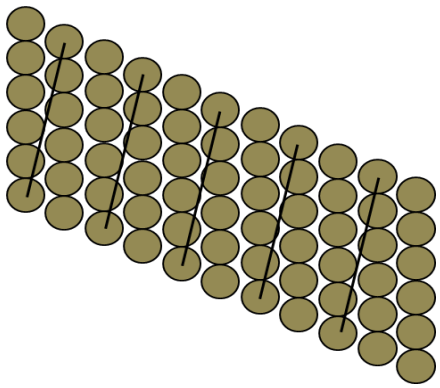

Figure 5-3: Schematic of elastic spring reinforcements. The black lines represent the springs connecting surface particles to particles below the surface of the slope.

Initially there are no forces between reinforced particles. In a manner similar to that of a spring, as the surface particles begin to flow and the distances between the particles grow (i.e., the spring extends), forces are developed that act to hold the surface particles in place. The forces between two connected particles can be tensile or compressive and are calculated by multiplying the change in distance by the spring stiffness. The key is that the spring stiffness is multiplied by the change in initial distance between the particles so that there are no spring forces generated between the particles until they start to move.

Numerically, the spring forces simply act to hold the surface particles in place. As an example, the forces in the DEM model will behave similarly to when weeds are pulled and soil clumps are connected to the roots. If one soil clump is pulled away, the particles will be held by the connected root system. The simulated springs are a preliminary attempt to represent the bulk of natural force potential generated by root attachment.

To evaluate a range of realistic root stiffnesses, the following equation was used:

$$K = \frac{AE}{L} \qquad \text{[Equation 5-2]}$$

where K is the stiffness, A is the cross-sectional area, E is the elastic modulus, and L is the length of the specimen. This is a standard formula used in one-dimensional bar mechanics. Using values provided by 1) Cofie et al. (2000) for beech roots resulted in a range of stiffnesses of 200 – 1,300 kN/m, 2) Commandeur and Pyles (1991) for Douglas-fir roots, a range of 14 – 1,170 kN/m, and 3) Greenberg et al. (1989) for ryegrass, a range of 0.4 – 1.3 kN/m. There is a lot of variability for these stiffnesses. Considering the data from Greenberg (1989) for ryegrass, a scaled-up value of 20 kN/m was chosen for the spring stiffness of the reinforcements used here.

**Simulation Details**

The DEM output files were written in appropriate syntax to link with ParaView (Ahrens et al., 2005) for post processing the DEM simulation results. This visualization process allowed for sophisticated imaging of the DEM results and the potential to develop videos of particle behavior. All figures of particles shown are screenshots from ParaView and give a visual to observe overall particle behavior. A description about a caveat is in order related to the output screen shots from ParaView. This software tool has limitations on how many particles are plotted. For over about 500 particles, not every particle shows up in the figures. An example is shown in Figure 5-4, with a screenshot of only the particles being plotted shown in 8a and white dots where the centers of all particles are in 8b. As can be seen in Figure 5-4a, there appear to be gaps of air on the front bottom edge but looking to Figure 5-4b there are actually particles in those locations. The reader is asked to keep this in mind for the screen shots presented in subsequent figures.

a) Particle plot only

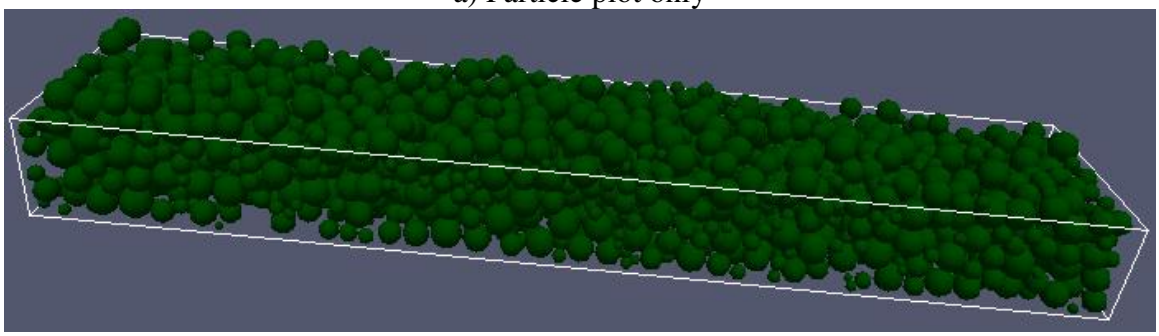

b) Particle plot with white dots at locations of all particle centroids

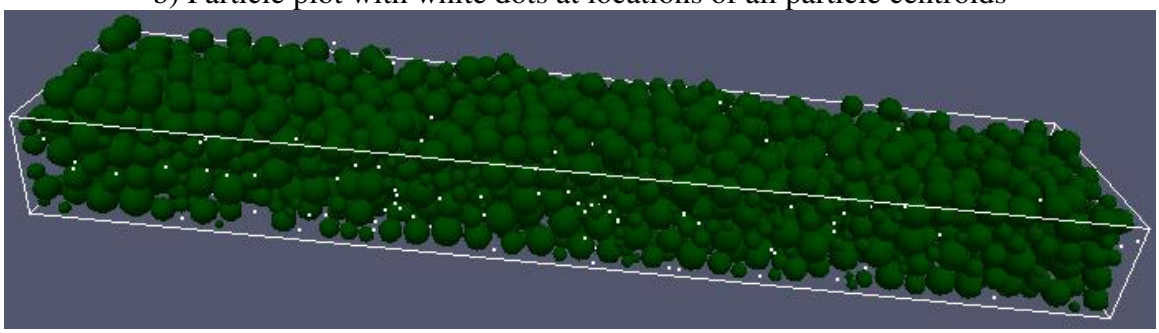

Figure 5-4: Example of plotting discrepancy in ParaView (this example is for 2400 particles).

*Particles*

As previously discussed, scaled up particle sizes were used to fill a reasonable volume of material with a reasonable number of particles. Coarse sand material properties were used for the force calculations in the model. Specifically, a density of 1850 kg/m$^3$, modulus of elasticity of 20 GPa, and a Poisson ratio of 0.15 were used (Bhavikatti, 2009). To ensure that particle size distribution does not have an effect when comparing simulation results of different slopes, the same set of 2,400 spherical particles with a uniform distribution of diameters between 1.8 and 8.0 millimeters were used in each slope generation. Here, a uniform distribution simply means that there are equal amounts of each size of particle.

*Domain and Boundary Conditions*

A figure of the domain and boundary conditions is shown in Figure 5-5 with a transparent box and the coordinate system orientation is shown in the bottom left corner. The size of the domain for the three slopes was 25 centimeters in the *x* direction and 5 centimeters in the *y* direction. The domains from the highest resting particle to the bottom rigid wall boundary were all about 3 centimeters deep in the *z* direction depending on where each slope equilibrated. The top of the box is a free surface. The boundary conditions (BCs) consisted of five rigid walls (BC1 – BC5 on Figure 5-5) and one other BC (BC6 on Figure 5-5). The second type of BC used for the simulations was one created for this DEM model, named a "save-mass" BC, and is defined by a boundary where once a particle passes the boundary, the mass of the particle is saved, no further force calculations are performed for the particle, and the particle is essentially absent from the rest of the analysis. This BC type was created because tracking sediment yield as a function of time during the simulations was an important output parameter. During the hydraulic flow event, the

particles began to roll down the slope and as more particles exited the save-mass boundary, the masses were summed to yield total eroded masses at the ends of the simulations.

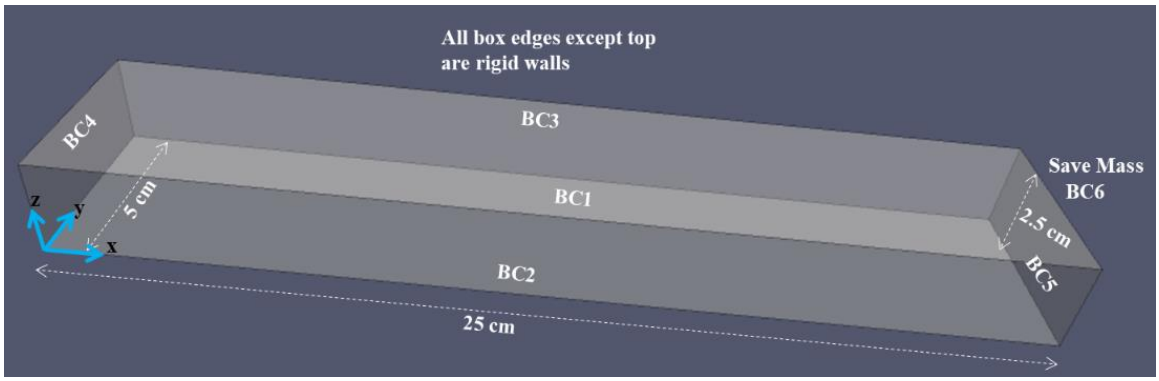

Figure 5-5: Boundary Conditions.

*Slope Generation*

Originally, a Matlab program was used to generate the 2,400 particles with random locations and diameter values (with the uniform distribution between 1.8 and 8.0 millimeters). The *x*, *y*, and *z* locations were bounded by the above described boundary conditions, with an upper bound on the *z* dimension equal to five times the height of BC5. Any initially overlapping particles were relocated until none of the particles were initially touching. Then, using the DEM model, the particles free fell under gravity in the negative *z* direction until they were settled in equilibrium. Next, simulations were performed slowly rotating and then holding gravity at specific slopes to reach equilibrium states for the particle packings. This process created the three slopes shown below in Figure 5-6, for 6°, 9°, and 12°. Although at different slopes (defined by α in Figure 5-6), the particle locations are very similar from one slope to the next.

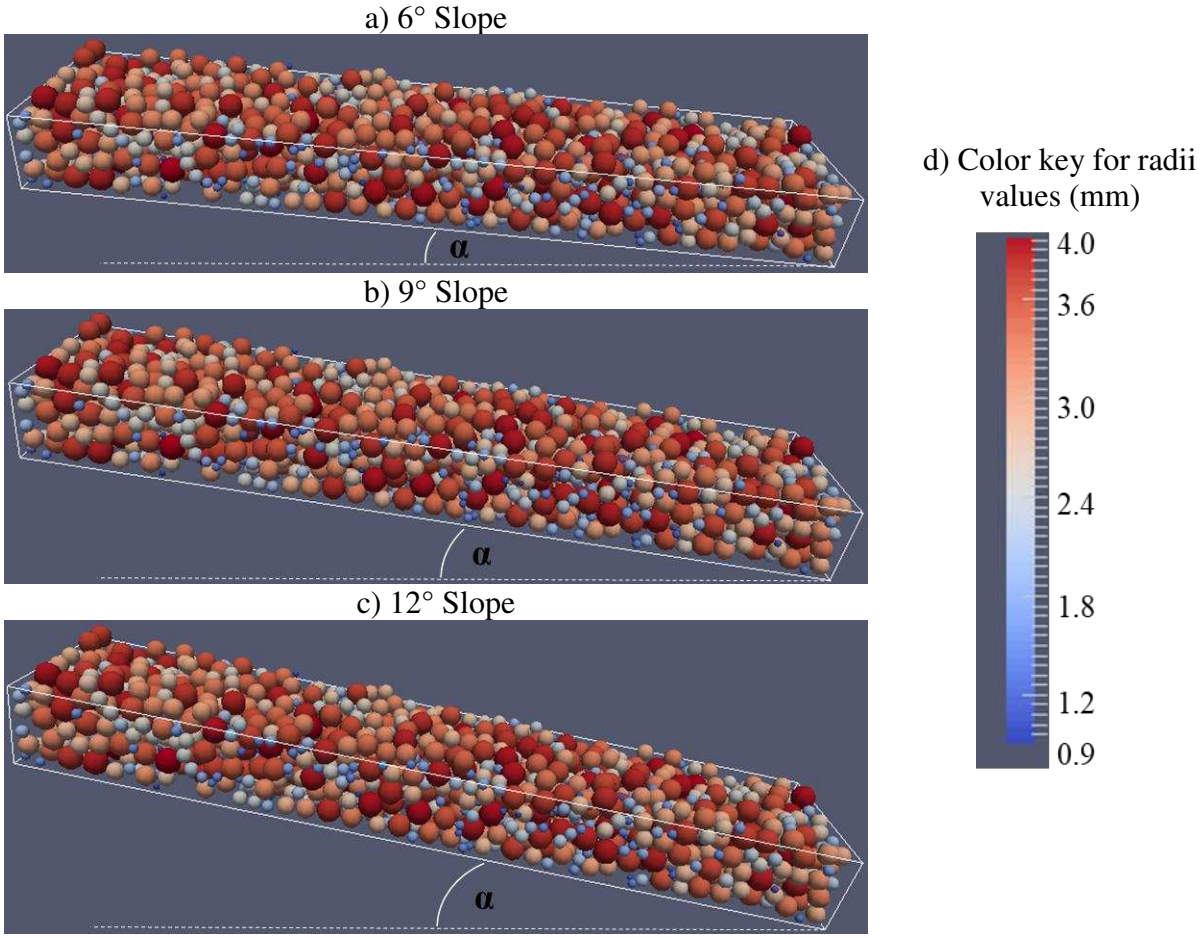

Figure 5-6: Initial Configurations of the Particle Packings at 3 Slopes.

*Identifying Surface Particles*

Particles were assigned as surface particles if their centroidal $z$ location was above $z_{surf}$, a measure developed to provide consistent surface location that was calculated by

$$z_{surf} = 1.5(z_{ave} - 1) + 1 \quad \text{[Equation 5-3]}$$

where $z_{ave}$ is the average $z$ location of all particles and the plus and minus 1 is because the bottom left corner of the particle boundary is not located at the origin of the coordinate system, but rather at (1m, 1m, 1m). Equation 5-3 lends to approximately the top third particles of the packings identified as surface particles. Once a particle is assigned as a surface particle, the

magnitude of the drag force applied to the particle is $z_{mult}F_D$ (from Equation 5-1), where $z_{mult}$ is a unitless multiplier varying linearly as a function of depth as shown in Figure 5-7.

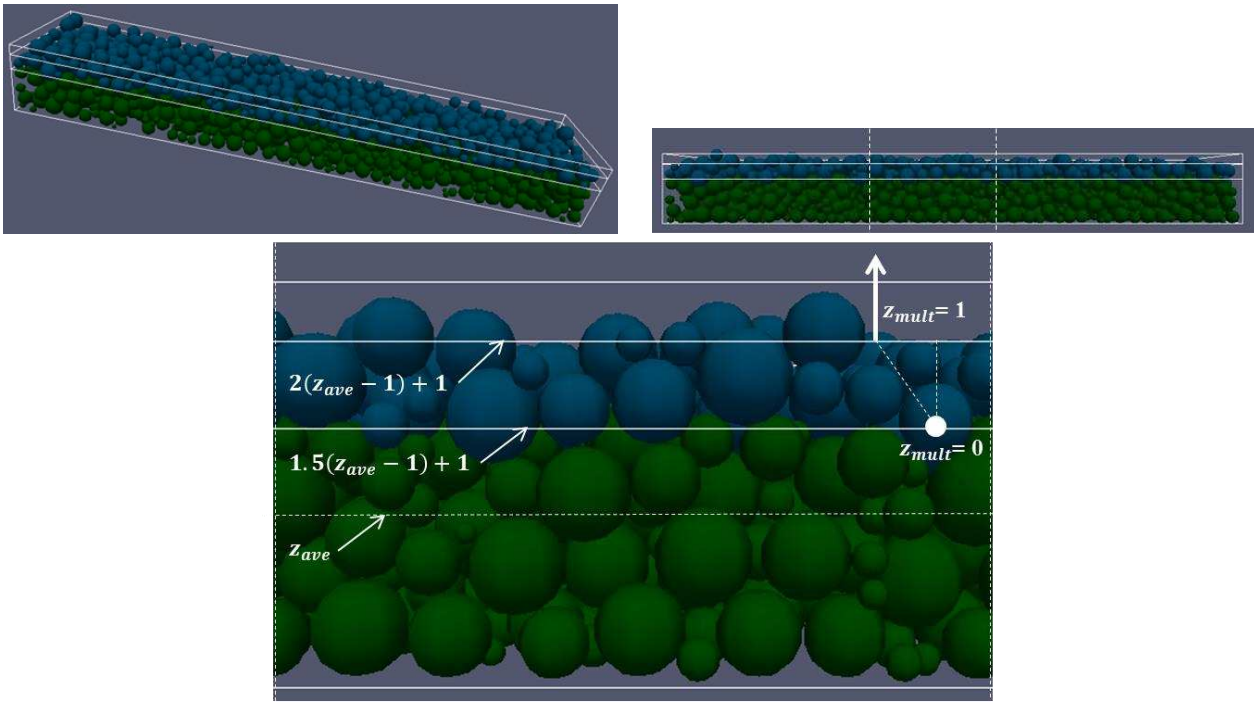


Figure 5-7: Schematic of which particles are assigned as surface particles and what magnitude multiplier is assigned for the drag force calculations.

Several iterations of this algorithm were tested to find the ideal distance parameters and ensure the majority of surface particles are identified while not including particles too deep in the packing. One case of the unreinforced 12º slope with a fluid velocity of 0.5 m/s is shown in Figure 5-8 at 0, 1.5, 3, and 4.5 seconds to show an example of how particles are being assigned as surface particles, shown as blue particles in the screen shots.

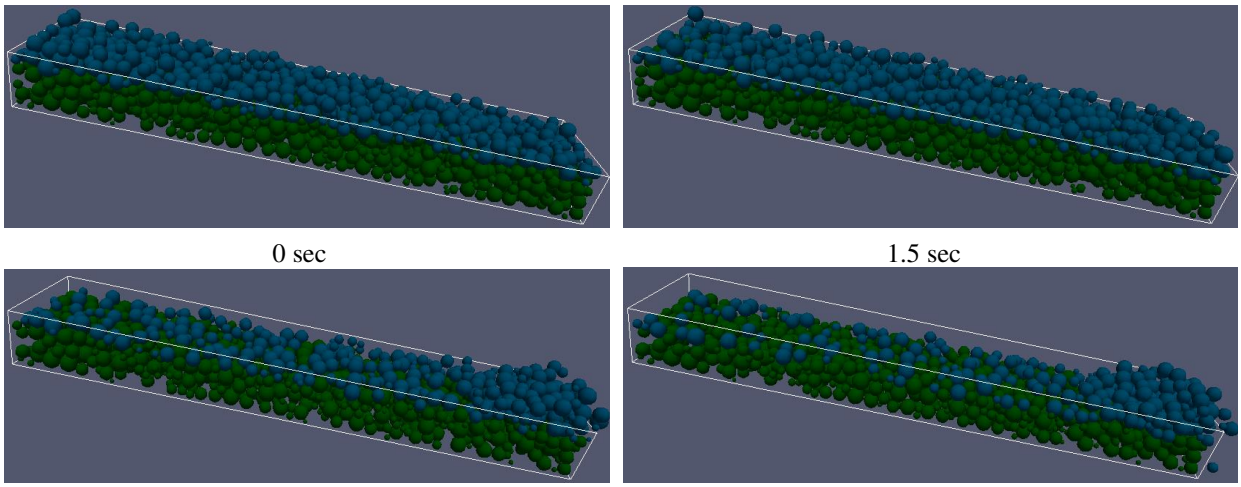

Figure 5-8: Unreinforced 12º Slope with 0.5 m/s fluid velocity. Blue particles are surface particles.

*Reinforcement Configurations*

The following four levels of reinforcement were simulated on the particle packings: 1) Unreinforced, 2) 10% Reinforcement, 3) 25% Reinforcement, and 4) 50% Reinforcement. The progression of increased percent reinforcements was meant to represent root development in a soil over time. A dataset these reinforcement percentages could be compared to was previously discussed (Schmeer et al., 2018) and the proposed reinforcement levels could represent the percent ground cover of live vegetation roughly 6 months (10%), 1 year (25%), and 3 years (50%) after a fire.

From the equilibrated particle locations, there were initially 596 surface particles. Among these particles, 50% (298) were randomly chosen to be reinforced and connected by roots to randomly selected deeper particles in contact with BC1 (the bottom of the control volume). Although the bottom particles were randomly chosen, the limitation was imposed that the deep particle must have a smaller $x$ coordinate than the connected surface particle (the deep particle is

positioned to the left of the surface particle). From the 298 reinforced particles (50% of 596), 149 (25% of 596) and 60 (10% of 596) were randomly chosen for the two other reinforcement configurations. The unreinforced and reinforced initial configurations for the 6° slope are shown in Figure 5-9. The 9° and 12° slopes had very similar initial configurations and are not shown here for sake of brevity.

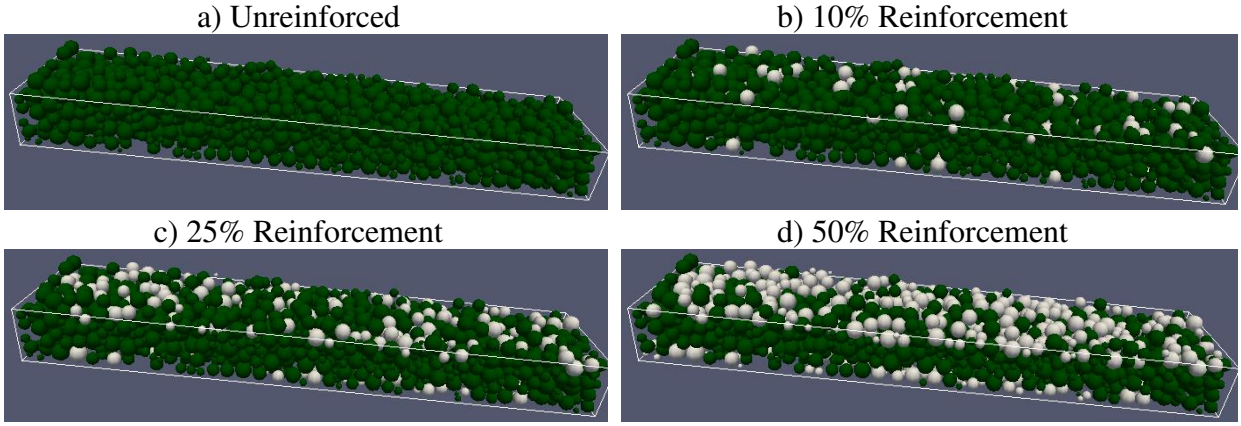


Figure 5-9: 6º Slope unreinforced and reinforced initial configurations. White particles signify reinforcement locations.

*Input Parameters*

All input parameters are summarized in Table 5-1. The limiting time increment for DEM simulations with spheres and a Hertzian contact model is a function of the minimum radius of all particles in the simulation and the material properties of that particle (Sheng et al., 2004). A time step increment of $1.0 \times 10^{-6}$ second, one-millionth of a second, was assigned and was below the critical time increment required. The simulations were run for 4.5 seconds of simulation time, resulting in a total of 4.5 million time steps per simulation.

Table 5-1: Input Parameters for Simulations

| Parameter (units) | Value | Source |
|---|---|---|
| Acceleration due to gravity ($m/s^2$) | 9.81 | - |
| Number of Particles | 2400 | - |
| Density ($kg/m^3$) | 1850 | (Bhavikatti, 2009) |
| Poisson's Ratio | 0.15 | (Bhavikatti, 2009) |
| Modulus of Elasticity (GPa) | 20 | (Bhavikatti, 2009) |
| Time step increment (sec) | $10^{-6}$ | Above critical |
| Elastic spring reinforcement stiffness (N/m) | 20,000 | Estimated |
| Particle-particle friction coefficient | 0.6 | Estimated |
| Mass damping coefficient | 25 | Calibrated value |
| Particle-particle contact damping coefficient | 0.15 | Calibrated value |

*Output Parameters*

The parameters tracked during the simulations included the average accumulated displacement of the particles and the eroded masses (tracked with the save mass BC6). The total displacement for each particle was calculated by summing the displacement magnitudes cumulatively for each particle, each time step (as opposed to simply subtracting the initial locations from the final locations). Then each time step the cumulative displacements were summed for all particles and divided by the total number of particles to calculate the average accumulated displacement. If a particle exited BC6 no further calculations were performed for the particle and the total number of particles was decreased by 1. Percent sediment yield was calculated as the sum of the eroded masses of particles that exited BC6 divided by the total mass of the 2400 particles. These measures provided a way of evaluating differences between the unreinforced and reinforced cases.

**Results and Discussion**

An example side by side comparison of particle positions at multiple times throughout the simulations (1.5, 3.0, and 4.5 seconds) is shown in Figure 5-10 for the 12° slope, 0.50 m/s fluid velocity unreinforced case (left) and 50% reinforcement case (right). Because videos cannot be included here, Figure 5-10 is essentially composed of screen shots throughout the result videos so that the reader can visualize the movements of the particles throughout the simulations. The particle flow shown in Figure 5-10 was typical for the other simulations. However, for sake of brevity, other particle position plots are not included but rather more detailed quantitative data is discussed in the remainder of this section.

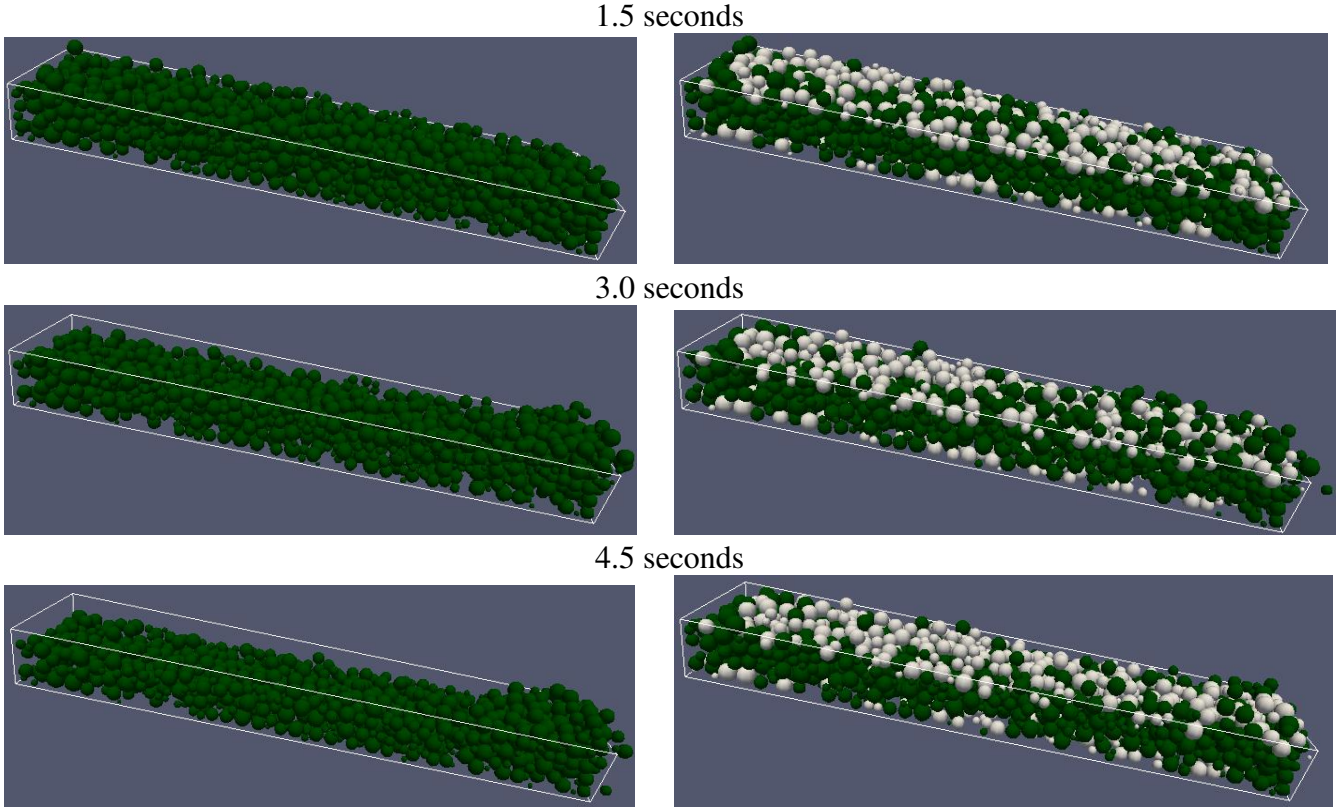


Figure 5-10: 12º Slope with 0.50 m/s Fluid Velocity Particle Position Plots
Unreinforced (left) vs. 50% Reinforcement (right)

Figures 5-11, 5-12, and 5-13 show the average accumulated displacements of particles

versus simulation time for all three slopes with both 0.25 m/s and 0.5 m/s fluid velocities. When the slope of an accumulated displacement line approaches zero, there is almost no particle movement occurring, although the drag force is still being applied (i.e. the slope has essentially re-equilibrated). The dashed lines in Figure 5-11 all appear horizontal, because the 6° slope simulations with a fluid velocity of 0.25 m/s (smallest slope and smallest hydraulic forces) had very little particle movement. The total average accumulated displacement for the unreinforced 6° slope with a fluid velocity of 0.25 m/s was less than 0.12 cm and therefore, the results for this slope and fluid velocity are not included in the other result comparisons presented.

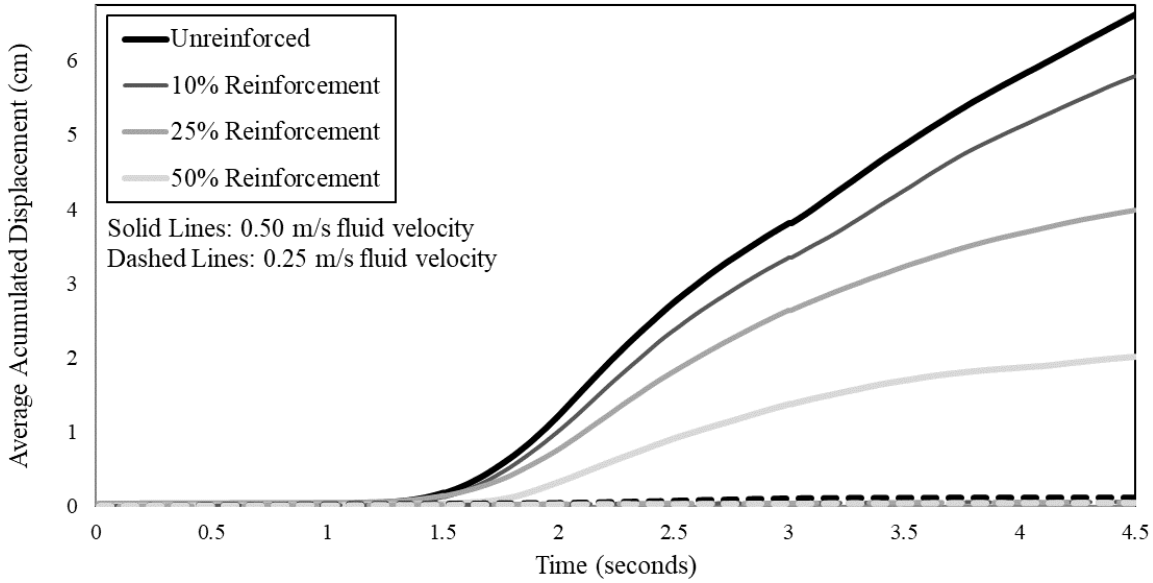


Figure 5-11: 6° Slope Spring Reinforcement Simulations
Average Accumulated Displacement vs. Time

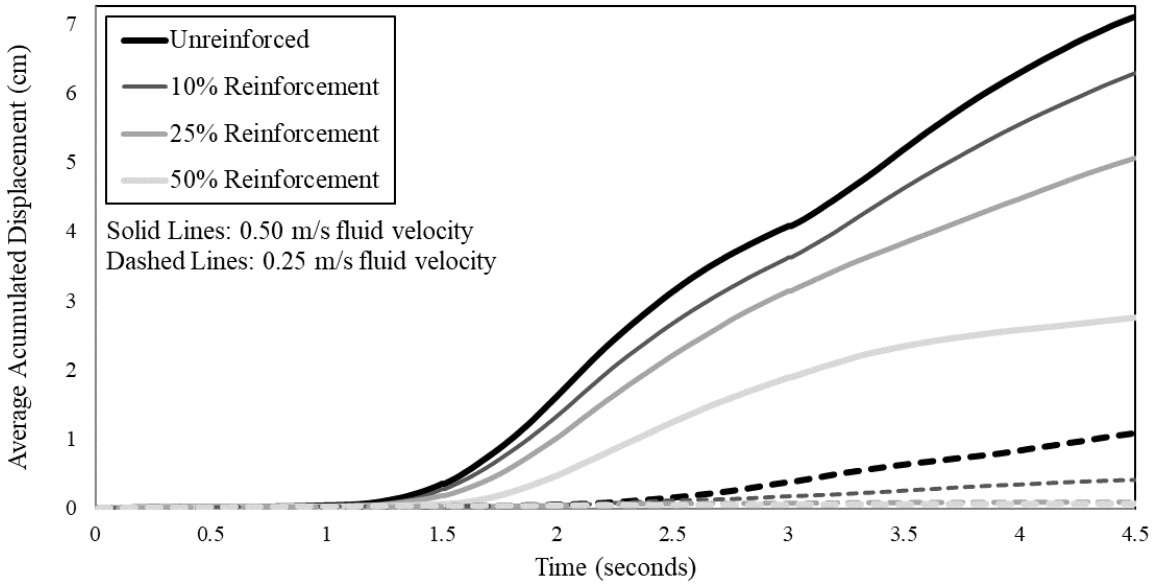


Figure 5-12: 9° Slope Spring Reinforcement Simulations
Average Accumulated Displacement vs. Time

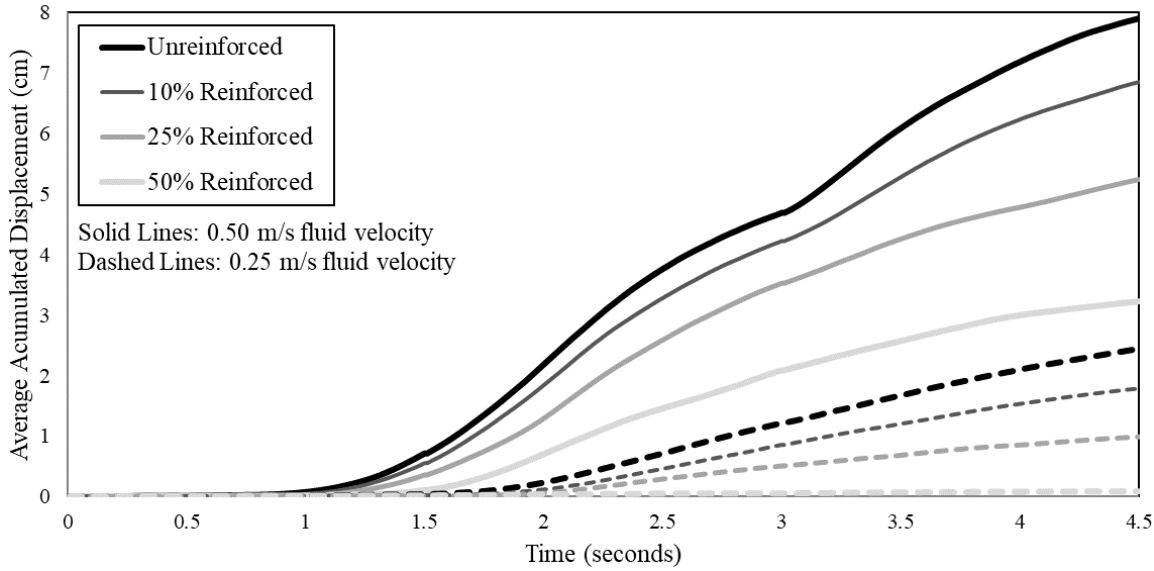


Figure 5-13: 12° Slope Spring Reinforcement Simulations
Average Accumulated Displacement vs. Time

One basic, expected result confirmed by Figures 5-11 through 5-13 is that for all slopes, an increase in percent root reinforcement resulted in a decrease in particle movement. In other words, the lines always fall in order (top to bottom of plot) as Unreinforced, 10% Reinforcement, 25% Reinforcement, and 50% Reinforcement from greatest average accumulated displacement to

lowest. Another basic expected result confirmed by the figures is that the higher fluid velocity (0.5 m/s) simulations (solid lines) have larger displacements over time than the lower fluid velocity (0.25 m/s) counter parts (dashed lines). In other words, the solid lines always fall above the dashed lines.

The final average accumulated displacements (Final AAD) for all simulations (except 6° slope, 0.25 m/s fluid velocity) are plotted in Figure 5-14 as a function of percent reinforcement. The data shows linear behavior between increased percent reinforcement and decreased particle movement.

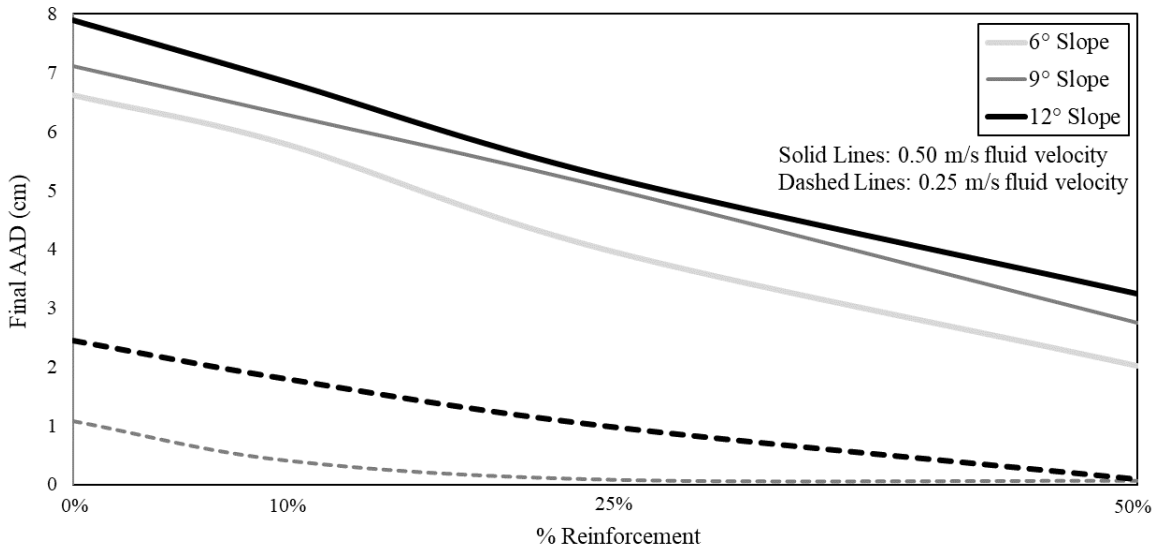


Figure 5-14: Final Average Accumulated Displacement (AAD) vs. Percent Reinforcement

The percent decreases in total displacement for the reinforced cases compared to the unreinforced (values plotted in Figure 5-14) are listed in Table 5-2. For the lower fluid velocity, the 50% reinforcement case almost completely stopped particle movement, with an average of 95.5% displacement decrease as compared to the unreinforced cases. For the larger fluid velocity, there was a 63.3% average decrease in particle displacements for the 50% reinforcement cases compared to the unreinforced cases.

Table 5-2: Percent Decreases in Total AAD for Reinforced Simulations Compared to Unreinforced

| | **0.25 m/s Fluid Velocity** | | |
|---|---|---|---|
| **Slope** | *10% Reinforcement* | *25% Reinforcement* | *50% Reinforcement* |
| 9° | 62% | 92% | 94% |
| 12° | 27% | 60% | 97% |
| | **0.50 m/s Fluid Velocity** | | |
| **Slope** | *10% Reinforcement* | *25% Reinforcement* | *50% Reinforcement* |
| 6° | 13% | 40% | 70% |
| 9° | 12% | 29% | 61% |
| 12° | 13% | 34% | 59% |

The final AADs are plotted in Figure 5-15 as a function of slope. The data shows linear behavior between increased slope and increased particle movement. However, confirming the linear trend is difficult with only 3 points for the datasets.

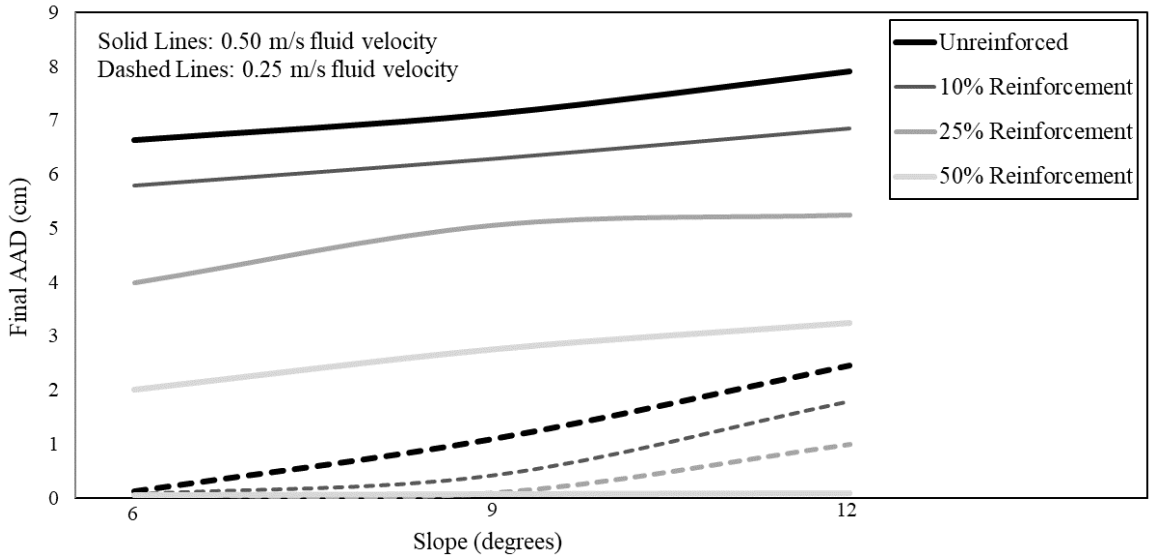


Figure 5-15: Final Average Accumulated Displacement (AAD) vs. Slope

A comparison of average accumulated displacements versus simulation time between the three slopes for only the unreinforced cases can be seen in Figure 5-16. The one expected result confirmed by Figure 5-16 is that the larger the slope, the higher the average accumulated displacements. When the overland fluid velocity was 0.25 m/s, there was an average decrease of

24% AAD for every 1° decrease in slope. For the 0.50 m/s fluid velocity simulations, there was an average decrease of 3% AAD for every 1° decrease in slope. These results suggest that for lower fluid velocities, particle displacements are much more dependent on incremental changes in slope; whereas at higher fluid velocities, particle displacements are not dependent on changes of slope less than 6°.

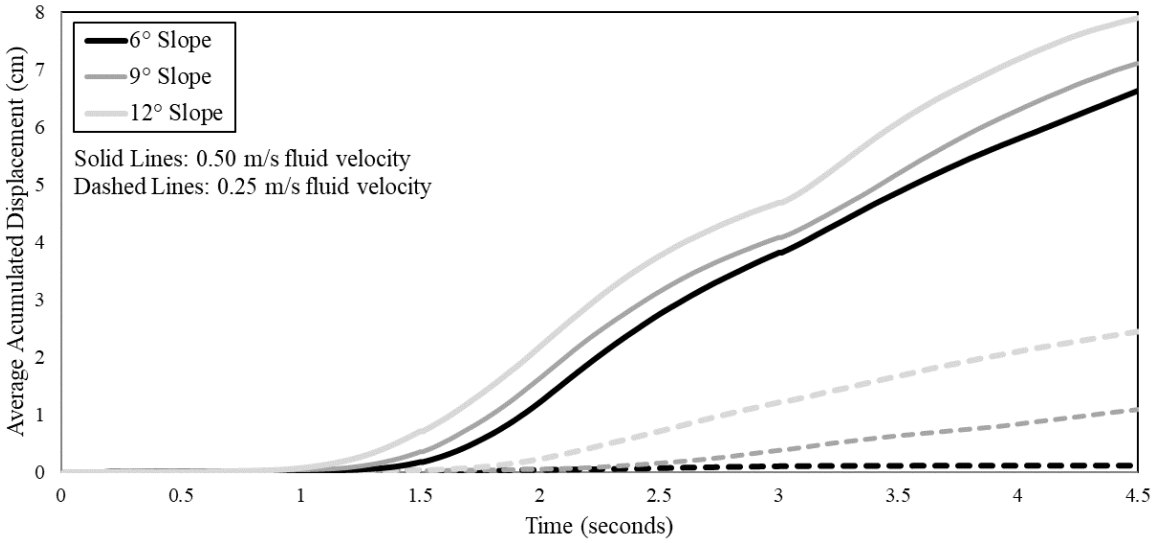


Figure 5-16: Unreinforced Simulations for All Slopes
Average Accumulated Displacement vs. Time

To compare the percent sediment yield from slope to slope, the percent sediment yields at 4.5 seconds of simulation time were calculated for all simulations. Results are shown in Table 5-3 for the 0.5 m/s fluid velocity results. Results for the 0.25 m/s fluid velocity are not included in the table, because the highest percent sediment yield was 1.0% for the 12° Slope unreinforced case and the rest were either zero or very close to zero.

Table 5-3: Final Percent Sediment Yields for 0.50 m/s Fluid Velocity Simulations

| Slope | Reinforcement | | | |
|---|---|---|---|---|
| | *Unreinforced* | *10% Reinforcement* | *25% Reinforcement* | *50% Reinforcement* |
| 6° | 25.5% | 18.8% | 10.1% | 2.1% |
| 9° | 27.0% | 20.6% | 13.6% | 4.8% |
| 12° | 32.2% | 24.1% | 16.4% | 5.7% |

As expected, the total percent sediment yield is largest for the steepest slope in each reinforcement case. An overall trend is that percent sediment yield increases (on average) 0.93% with an increase of 1° in slope for all simulations (unreinforced and all reinforcements).

The data from Table 5-3 is plotted in Figure 5-17 as a function of percent sediment yield versus percent reinforcement. As with the final average accumulated displacements, the percent sediment yields also have a linear relationship with percent reinforcement. Overall, the unreinforced simulations have the largest percent sediment yields and sediment yield decreases linearly with the smallest values occurring for the 50% reinforcement simulations.

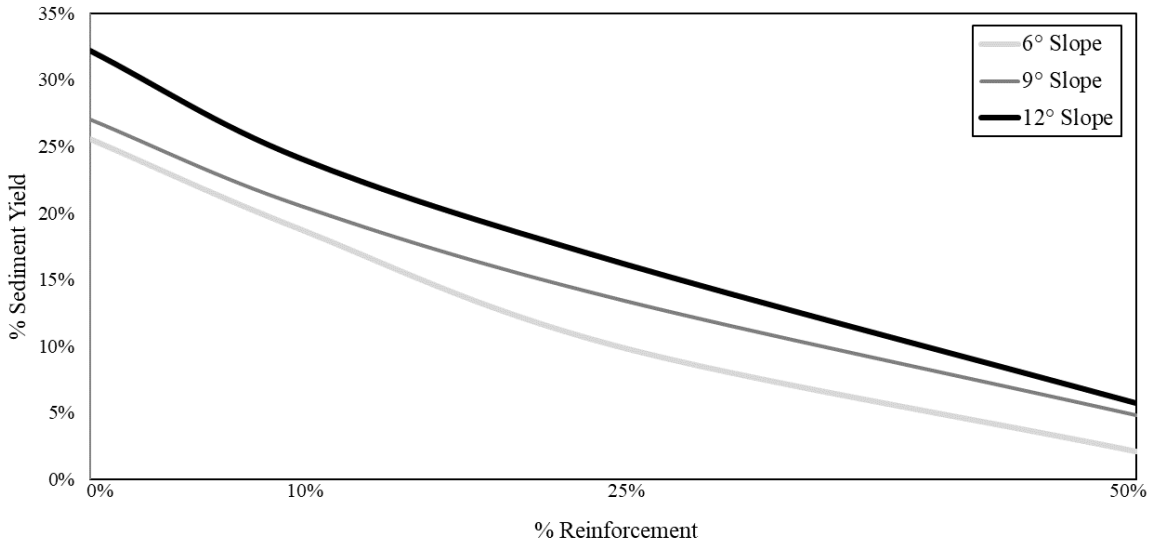


Figure 5-17: Percent Sediment Yield vs. Percent Reinforcement
0.50 m/s Fluid Velocity Simulations

## Conclusions

The research presented here tests the hypothesis that the DEM can be used to quantify the decrease in particle movement that occurs as a function of root reinforcement represented with elastic springs. A DEM model was developed and simulations were performed on three-dimensional coarse sand particle packings at varying slopes, subjected to two different overland flow fluid velocities, and reinforced with varying amounts of elastic springs, representative of roots. Particle displacements were tracked as functions of time, slope, fluid velocity, and reinforcement level for each simulation. The reinforcement levels were 10%, 25%, and 50% surface particles.

Results support the hypothesis and specific conclusions from the work are bulleted here:

- Particle movement decreases linearly with increased percent reinforced surface particles under overland flow conditions.
- Particle movement increases linearly with increased slope under overland flow conditions.
- At lower fluid velocities, particle displacements are more dependent on incremental changes in slope; whereas at higher fluid velocities, particle displacements are not dependent on changes of slope less than 6°.
- Total percent sediment yields increase an average of 0.93% with an increase of 1° in slope.
- Percent sediment yields decrease linearly as a function of percent reinforced surface particles under overland flow conditions.

The overarching goals of this research were not only to assess numerically how decreased erosion occurs as a function of increased root development, but more importantly introduce a first

effort to a new modeling technique for root reinforcements using the DEM. Future work building on the research presented here could lead to a better understanding of the physical process of particle erosion with root reinforcements in place, investigate other modelling techniques for the reinforcements, including scaling effects, and make connections between the numerical simulations and large-scale field studies already being performed.

# Chapter 6 : CONCLUSIONS AND RECOMMENDATIONS FOR FUTURE RESEARCH

This dissertation investigated the use of the discrete element method specifically for research concerning the erosion processes that occur in particle packings either with surface treatments present or reinforced with elastic springs. Both an in-house DEM model and an experiment apparatus were developed and tested, and simulations and experiments were performed to track particle erosion and sediment yields as functions of slope, hydraulic force, and level of reinforcement/surface treatment. Conclusions and recommendations are presented here for this research.

## Conclusions

Conclusions from the work include:

- As the added mass on the surface of a particle packing increases, erosion rates under surficial flow conditions decrease.
- As the slope of the particle packing increases, erosion rates increase.
- At lower masses of surface treatment, the particle erosion rates as a function of fluid velocity are dominated by piecewise linear behavior, indicating an initial resistance to flow followed by widespread failure or erosion at a much higher rate.
- There are linear relationships between decreased particle movement with increased percent reinforced surface particles, increased particle movement with increased slope, and decreased sediment yields with increased percent reinforced surface particles under overland flow conditions.
- At lower fluid velocities, particle displacements are more dependent on incremental changes in slope; whereas at higher fluid velocities, particle displacements are not

dependent on small changes in slope.

More importantly, the results from the work presented herein support the following hypotheses:

1. Compressive stress from added mass on the surface is a major contributor to the effectiveness of surface treatments in decreasing erosion (Chapter 4).
2. Decreased erosion that occurs as a function of increased root development can also be shown using the DEM to model root reinforcements numerically with elastic springs (Chapter 5).

Case studies from physical field observations have already shown correlations between both the application of ground treatments and increased vegetative ground cover with the decrease in erosion and annual sediment yields. However, the research in this dissertation provides insight to a tool, a DEM model, that has the potential to assess surface treatment effectiveness and other slope reinforcements numerically, before conducting large scale field studies. Although the effectiveness of ground treatments is already being tested at the field scale, being able to accurately model with the DEM is an improvement and addition to current practice.

**Recommendations for Future Research**

The work completed here was limited by computational resources and of course overall scope and the need to have a stopping point. If more time permitted, there are two main areas outside the scope of this dissertation believed to be the most important to explore as possibilities for future research and those are briefly described here.

Future research towards modeling non-spherical geometries with the DEM would allow for other surface treatments to be evaluated numerically. Structures with non-spherical geometries can be modeled with overlapping or contacting spheres (called agglomerates) that are fixed in position relative to each other (Bossy & Safuryn, 2016). Preliminary simulations have been performed using an agglomerate method to simulate agricultural straw surface treatment material on the same spherical particle packing explored in Chapter 4. Initial results follow the trends of the data presented here; however, further research needs to be performed. For modeling straw, tests should be performed to investigate other properties of the straw material and interaction properties between the straw and the material being protected. Then the DEM model could be properly calibrated with respect to the mulch material. Also, the behavior of the interaction between the fluid and the surface treatment was different between the layer of steel particles and the straw surface treatment experiments. Future research could also allow for a more thorough investigation on the differences in these forces so that the appropriate forces can be applied for modeling other surface treatment materials in the DEM simulations.

The exact forces between soil particles and connected roots were not experimentally investigated or quantified here and were therefore simply estimated from root tensile strengths. However, pull-out strength between soil aggregates and roots could be a different phenomenon to investigate experimentally and is potentially (and probably) not a function simply of root tensile strength, although that is what was assumed here. Testing the physical relevance of the elastic spring reinforcements used here by experimentally investigating a soil sample with and without roots would be an interesting potential for future research. One idea would be to possibly create a DEM simulation that represents a direct shear test and make comparisons to physical experiments

with and without roots to assess how to better model the physical forces from root reinforcements in soil.

## REFERENCES


Ahrens, J., Geveci, B., & Law, C. (2005). ParaView: An End-User Tool for Large Data Visualization, Visualization Handbook. Elsevier.

Bautista, S., Bellot, J., & Vallejo, V. R. (1996). Mulching treatment for postfire soil conservation in a semiarid ecosystem. *Arid Soil Research and Rehabilitation*, **10**, 235-242.

Bautista, S., Robichaud, P. R., & Blade, C. (2009). Post-fire mulching. *Fire effects on soils and restoration strategies*, 353-372.

BC Precision. (2018). Precision Ball Bearings. https://www.bcprecision.com/collections/chrome-steel-ball-bearings/products/1-2-inch-chrome-steel-ball-bearings-g25.

Bhavikatti, S. S. (2009). Properties of Soils. In S. S. Bhavikatti, *Design of Steel Structures* (p. Appendix C). I. K. International Pvt Ltd.

Bossy, C., & Safuryn, P. (2016, June 22). What is DEM: Theoretical background behind the Discrete Element Method (DEM). Edinburgh, United Kingdom.

Butlanska, J., Arroyo Alvarez de Toledo, M., & Gens Sole, A. (2009). Homogeneity and symmetry in DEM models of cone penetration. *Proceedings of the 6th International Conference on Micromechanics of Granular Media*, 425-428.

Chandramohan, R., & Powell, M. S. (2005). Measurement of particle interaction properties for incorporation in the discrete element method simulation. *Minerals Engineering*, **18**, 1142-1151.

Chung, Y. C. (2006). Discrete element modelling and experimental validation of granular solid subject to different loading conditions. University of Edinburgh, UK PhD Dissertation.

Chung, Y. C., & Ooi, J. Y. (2011). Benchmark tests for verifying discrete element modelling codes at particle impact level. *Granular Matter*, **13**, 643-656.

Coetzee, C. (2014). Discrete and continuum modelling of soil cutting. *Computational Particle Mechanics*, **1**, 409-423.

Cofie, P., Koolen, A. J., & Perdok, U. D. (2000). Measurement of stress-strain relationship of beech roots and calculation of the reinforcement effect of tree roots in soil-wheel systems. *Soil & Tillage Research*, **57**, 1-12.

Commandeur, P. R., & Pyles, M. R. (1991). Modulus of elasticity and tensile strength of Douglas-fir roots. *Canadian Journal of Forest Research*, **21**, 48-52.

Cui, L., & O'Sullivan, C. (2006). Exploring the macro- and micro-scale response characteristics of an idealized granular material in the direct shear apparatus. *Geotechnique*, **56**, 455-468.

Cui, L., O'Sullivan, C., & O'Neill, S. (2007). An analysis of the triaxial apparatus using a mixed boundary three-dimensional discrete element model. *Geotechnique*, **57**, 831-844.

Cundall, P. (1987). Distinct element models of rock and soil structure. In E. Brown, Analytical and Computational Methods in Engineering Rock Mechanics. Allen and Unwin.

Cundall, P. (2001). A discontinuous future for numerical modelling in geomechanics? *Proceedings of the institution of civil engineers geotechnical engineering*, **149**, pp. 41-47.

Cundall, P. A., & Strack, O. D. (1979). A discrete numerical model for granular assemblies. *Geotechnique*, **29**(1), 47-65.

Dean, A. E. (2001). Evaluating effectiveness of watershed conservation treatments applied after the Cerro Grande Fire, Los Alamos, New Mexico. Tucson, AZ: University of Arizona Master's Thesis.

Demars, K. R., Long, R. P., and Ives, J. R. (2004). Erosion Control Using Wood Waste Materials. *Compost Science and Utilization,* **12***,* 35-47.

deWolfe, V. G., Santi, P. M., Ey, J., and Gartner, J. E. (2008). Effective mitigation of debris flows at Lemon Dam, La Plata County, Colorado. *Geomorphology,* **96***,* 366-377.

Dong, K. J., Yang, R. Y., Zou, R. P., & Yu, A. B. (2006). Role of Interparticle Forces in the Formation of Random Loose Packing. *Physical Review Letters*, **96**(145505), 1-4.

Emmett, W. W. (1970). The Hydraulics of Overland Flow on Hillslopes: Dynamic and Descriptive Studies of Hillslopes. *Geological Survey Professional Paper*, 662-A

Foerster, S. F., Louge, M. Y., Chang, H., & Allia, K. (1994). Measurements of the collision properties of small spheres. *Physics of Fluids*, **6**, 1108-1115.

Geertsema, M., Schwab, J. W., Jordan, P., & Rollerson, T. (2010). Hillslope processes. In Compendium of forest hydrology and geomorphology in British Columbia (p. Chapter 8). BC Ministry of Forests and Range.

Gladkyy, A., & Schwarze, R. (2014). Comparison of different capillary bridge models for application in the discrete element method. *Granular Matter*, **16**, 911-920.

Gomez, J. A. & Nearing, M. A. (2005) Runoff and sediment losses from rough and smooth soil surfaces in a laboratory experiment, *Catena*, **59**, 253-266.

Greenberg, A. R., Mehling, A., Lee, M., and Bock, J. H. (1989). Tensile behaviour of grass. *Journal of Materials Science,* **24**, 2549-2554.

Halff Associates, Inc. (1998) Stream Bank Stabilization Manual. Prepared for the cities of Plano, Garland, McKinney, and Allen by Halff Associates, Inc. in conjunction with West Consultants, Inc.

Hamaker, H. C. (1937). The London-van der Waals attraction between spherical particles. *Physica (Amsterdam)*, **4**, 1058-1072.

Huang, A. B., & Ma, M. Y. (1994). An analytical study of cone penetration tests in granular material. *Canadian Geotechnical Journal*, **31**, 91-103.

Israelachvili, J. N. (1991). Intermolecular and Surface Forces. London: Academic Press.

Itasca. (2004). PFC2D 3.10 Particle Flow Code in Two Dimensions, Theory and Background volume. Minneapolis, MN.

Iwashita, K., & Oda, M. (1998). Rolling Resistance at Contacts in Simulation of Shear Band Development by DEM. *Journal of Engineering Mechanics*, **124**, 285-292.

Jennings, G. D., & Jarrett, A. R. (1985). Laboratory Evaluation of Mulches in Reducing Erosion. *American Society of Agricultural Engineers*, 1466-1470.

Julien, P. Y. (2010). Erosion and Sedimentation 2nd Edition. New York: Cambridge University Press.

Kharaz, A. H., Gorham, D. A., & Salman, A. D. (2001). An experimental study of the elastic rebound of spheres. *Powder Technology*, **120**, 281-291.

Kilinc, M., & Richardson, E. V. (1973). Mechanics of Soil Erosion from Overland Flow Generated by Simulated Rainfall. 63.

Krupp, H. (1967). Particle adhesion theory and experiment. *Advances in Colloid and Interface Science*, **1**, 111-239.

Lian, G., Thornton, C., & Adams, M. J. (1993). A Theoretical Study of the Liquid Bridge Forces between Two Rigid Spherical Bodies. *Journal of Colloid and Interface Science*, **161**, 138-147.

Lu, C.-Y., Tang, C.-L., Chan, Y.-C., Hu, J.-C., & Chi, C.-C. (2014). Forecasting landslide hazard by the 3D discrete element method: A case study of the unstable slope in the Lushan hot spring district, central Taiwan. *Engineering Geology*, **183**, 14-30.

MagLite. (2018). MAG 500 Qty 1/2" Inch Glass Marble Slingshot Ammo Solid Shot. www.amazon.com.

Masson, S., & Martinez, J. (2001). Micromechanical analysis of the shear behavior of a granular material. *Journal of Engineering Mechanics*, **127**, 1007-1016.

Matsushima, T., Saomoto, H., Tsubokawa, Y., & Yamada, Y. (2003). Grain rotation versus continuum rotation during shear deformation of granular assembly. *Soils and Foundations Japanese Geotechnical Society*, **43**, 95-106.

Maw, N., Barber, J. R., & Fawcett, J. N. (1976). The oblique impact of elastic spheres. *Wear*, **38**, 101-114.

Mindlin, R. D., & Deresiewicz, H. (1953). Elastic Spheres in Contact Under Varying Oblique Forces. *Journal of Applied Mechanics*, **20**, 327-344.

Moden, K. N. (2018). Laboratory Evaluation of a Post-Fire Ground Treatment to Mitigate Soil Erosion and Runoff. Fort Collins, CO: Colorado State University Thesis.

Montenegro, A. A. A., Abrantes, J. R. C. B., de Lima, J. L. M. P., Singh, V. P., and Santos, T. E. M., (2013). Impact of mulching on soil and water dynamics under intermittent simulated rainfall. *Catena*, **109**, 139-149.

Munjiza, A. (2004). The combined finite-element methods. John Wiley.

Napper, C. (2006). Burned Area Emergency Response Treatments Catalog. San Dimas, CA: USDA Forest Service, San Dimas Technology and Development Center.

Ng, T. T. (2004). Shear strength of assemblies of ellipsoidal particles. *Geotechnique*, **54**, 659-670.

Ning, Z., & Ghadiri, M. (1996). Incorporation of Rayleigh damping into TRUBAL and determination of the critical time step.

O'Sullivan, C. (2011). Particle-Based Discrete Element Modeling: A Geomechanics Perspective. London and New York: Spon Press.

Padros, C. B., & Kokocinska, J. (2016). DEM Software for Simulating Granular Material Flow Behaviors. Edinburgh, United Kingdom.

Potyondy, D. O., & Cundall, P. A. (2004). A bonded-particle model for rock. *International Journal of Rock Mechanics and Mining Sciences*, **41**, 1329-1354.

Powrie, W., Ni, Q., Harkness, R. M., & Zhang, X. (2005). Numerical modelling of plane strain tests on sands using a particulate approach. *Geotechnique*, **55**, 297-306.

Ravi, S., D'Odorico, P., Zobeck, T. M., & Over, T. M. (2009). The effect of fire-induced soil hydrophobicity on wind erosion in a semiarid grassland: experimental observations and theoretical framework. *Geomorphology*, **105**, 80-86.

Renzo, A. D., & Maio, F. (2004). Comparison of contact-force models for the simulation of collisions in DEM-based granular flow codes. *Chemical Engineering Science*, **59**, 525-541.

Reike-Zapp, D. H. & Nearing, M. A. (2005). Slope Shape Effects on Erosion: A Laboratory Study. *Soil Science Society of America*, **69**, 1463-1471.

Robichaud, P. R., Ashmun, L. E., & Sims, B. D. (2010). Post-fire treatment effectiveness for hill-slope stabilization. Fort Collins: U.S. Department of Agriculture, Forest Service, Rocky Mountain Research Station.

Rocky Mountain Research Station Collaborators. (2017). Learn from the Burn: The High Park Fire 5 Years Later. Science You Can Use Bulletin. United States Department of Agriculture.

Rumpf, H. (1962). The strength of granules and agglomerates. In W. A. Knepper, Agglomeration (p. 379). New York: Wiley Interscience.

Sadeghi, S. H. R., Gholami, L., Sharifi, E., Khaledi Darvishan, A., and Homaee, M. (2015). Scale effect on runoff and soil loss control using rice straw mulch under laboratory conditions. *Solid Earth*, **6**, 1-8.

Saint-Gobain. (2018). Physical Properties of Glass. https://uk.saint-gobain-building-glass.com/en-gb/architects/physical-properties.

Schmeer, S. R., Kampf, S. K., MacDonald, L. H., Hewitt, J., & Wilson, C. (2018). Empirical models of annual post-fire erosion on mulched and unmulched hillslopes. *Catena*, **163**, 276-287.

Shahverdian, S. (2015). Controls on Post-High Park Fire Channel Response, South Fork Cache La Poudre Basin, Colorado. Fort Collins, CO: Colorado State University Master's Thesis Submission.

Sheng, Y., Lawrence, C., Briscoe, B., & Thornton, C. (2004). Numerical studies of uniaxial powder compaction process by 3D DEM. *Engineering Computations*, **21**(2/3/4), 304-317.

Smolen, M. D., Miller, D. W., Lichthardt, J., and Blalock, L. L. (2001). Erosion and Sediment Control Field Manual. A cooperative effort between the North Carolina Department of Environment and Natural Resources, and the North Carolina Agricultural Extension Service, supported by the North Carolina Sedimentation Control Commission.

Stead, D., Eberhardt, E., & Coggan, J. S. (2006). Developments in the characterization of complex rock slope deformation and failure using numerical modelling techniques. *Engineering Geology*, **83**, 217-235.

Stewart, S. I., Radeloff, V. C., & Hammer, R. B. (2003). Characteristics and location of the wildland-urban interface int he United States. Proceedings of the second international wildland fire ecology and fire management workshop. Orlando, FL: American Meteorological Society.

Swift Jr., L. W. (1984). Gravel and Grass Surfacing Reduces Soil Loss From Mountain Roads. *Journal of Forest Science,* **30***,* 657-670.

Taboada, A., & Estrada, N. (2009). Rock-and-soil avalanches: Theory and simulation. *Journal of Geophysical Research*, **114**, FO3004.

The Engineering Toolbox. (2004). Drag Coefficient. Retrieved from The Engineering Toolbox: https://www.engineeringtoolbox.com/drag-coefficient-d_627.html

Thornton, C. (2000). Numerical simulations of deviatoric shear deformation of granular media. *Geotechnique*, **50**, 43-53.

Thornton, C., & Antony, S. J. (2000). Quasi-static shear deformation of a soft particle system. *Powder Technology*, **109**, 179-191.

Timoshenko, S. P., & Goodier, J. N. (1970). Theory of Elasticity 3rd Edition. New York: McGraw-Hill.

University Corporation for Atmospheric Research. (2010). Odtokovy proces. Retrieved from http://portal.chmi.cz/files/portal/docs/poboc/CB/runoff_cz/print.htm

Vu-Quoc, L., & Zhang, X. (1999). An accurate and efficient tangential force-displacement model for elastic frictional contact in particle-flow simulations. *Mechanics of Materials*, **31**, 235-269.

Vu-Quoc, L., Zhang, X., & Walton, O. R. (2000). A 3-D discrete-element method for dry granular flows of ellipsoidal particles. *Computer methods in applied mechanics and engineering*, **187**, 483-528.

Wang, J., Gutierrez, M. S., & Dove, J. E. (2007). Numerical studies of shear banding in interface shear tests using a new strain calculation method. *International Journal for Numerical and Analytical Methods in Geomechanics*, **31**, 1349-1366.

Weigert, T., & Ripperger, S. (1999). Calculation of the Liquid Bridge Volume and Bulk Saturation from the Half-filling Angle. *Particle and Particle Systems Characterization*, **16**, 238-242.

Wu, C. Y., Thornton, C., & Li, L. Y. (2003). Coefficients of restitution for elastoplastic oblique impacts. *Advanced Powder Technology*, **14**, 435-448.

Yang, R. Y., Zou, R. P., & Yu, A. B. (2000). Computer simulation of the packing of fine particles. *Physical Review E*, **62**, 3900-3908.

Yen, K., & Chaki, T. K. (1992). A dynamic simulation of particle rearrangement in powder packings with realistic interactions. *Journal of Applied Physics*, **71**, 3164-3173.

Zhang, L., Wei, Z., Liu, X., & Li, S. (2005). Application of three-dimensional discrete element face-to-face contact model with fissure water pressure to stability analysis of landslide in Panluo iron mine. *Science in China Ser. E Engineering and Materials Science*, **48**, 146-156.

Zhang, X., & Vu-Quoc, L. (2002). Modeling the dependence of the coefficient of restitution on the impact velocity in elasto-plastic collisions. *International Journal of Impact Engineering*, **27**, 317-341.

Zhu, H., Zhou, Z., Yang, R., & Yu, A. (2007). Discrete particle simulation of particulate systems: Theoretical developments. *Chemical Engineering Science*, **62**(13), 3378-3396.